R-07-38

DarcyTools version 3.4
– Concepts, Methods and Equations

Urban Svensson and Hans-Olof Kuylenstierna
Computer-aided Fluid Engineering AB

Michel Ferry
MFRDC, Orvault, France

December 2010

Svensk Kärnbränslehantering AB
Swedish Nuclear Fuel
and Waste Management Co

Box 250, SE-101 24 Stockholm
Phone +46 8 459 84 00

ISSN 1402-3091
SKB R-07-38

DarcyTools version 3.4

– Concepts, Methods and Equations

Urban Svensson and Hans-Olof Kuylenstierna
Computer-aided Fluid Engineering AB

Michel Ferry
MFRDC, Orvault, France

December 2010

This report concerns a study which was conducted for SKB. The conclusions and viewpoints presented in the report are those of the authors. SKB may draw modified conclusions, based on additional literature sources and/or expert opinions.

Preface

As the first author of this report, I take the liberty to write a preface and explain a few things about the work leading to Version 3.4 of DarcyTools. This is necessary as Michel and Hans-Olof have not been involved in the writing of the main part of the report, and they may not even share all the views expressed.

The contributions from Michel and Hans-Olof can be specified as follows:

Michel:	Development and writing of most of the software that constitutes DarcyTools V3.4. Author and owner of the solver MIGAL. Author of Appendices A and H.
Hans-Olof:	Development of methods and writing of software for generation of fracture networks and their representation (in terms of properties) in the continuum model. Development of methods and writing of software for the particle tracking routine PARTRACK. Author of Appendices B, C and D.

My contribution has been in the development of concepts and methods, real world applications and tests. I have also coordinated the efforts and done my best to ensure that we deliver the product our client, SKB, expects.

Urban Svensson

Abstract

DarcyTools is a computer code for simulation of flow and transport in porous and/or fractured media. The fractured media in mind is a fractured rock and the porous media the soil cover on the top of the rock; it is hence groundwater flows, which is the class of flows in mind.

DarcyTools is a general code for this class of problems, but the analysis of a repository for nuclear waste is the main intended application.

A number of novel features are introduced in DarcyTools. The most fundamental is perhaps the method to generate grid properties (DarcyTools is a continuum porous-media code); a fracture network, with properties given to each fracture, is represented in the computational grid by a method that is based on intersecting volumes (fracture volumes and grid cell volumes). This method is believed to result in very accurate anisotropy and connectivity properties.

The report focuses on the concepts, assumptions, equations and key features of DarcyTools. The main part of the report is fairly short; a number of appendices give more detailed accounts of various aspects of the code.

Sammanfattning

DarcyTools är ett datorprogram för simulering av flöde och transport i ett poröst och/eller sprickigt medium. Det sprickiga mediet är ett sprickigt berg och det porösa mediet jordlagret som täcker berget; det är således grundvattenströmning som är applikationsområdet.

DarcyTools är ett generellt program för grundvattenströmning, men tillämpningar som rör analyser av förvar för uttjänt kärnbränsle står i fokus.

Ett antal nya koncept och metoder utgör hörnpelare i DarcyTools. Den kanske mest fundamentala av dessa rör metoden för att representera hydrauliska egenskaper i beräkningsnätet (DarcyTools är en så kallad ”porös kontinuum kod”). Metoden bygger på en direkt representation av ett spricknätverk, som kan innefatta flera miljoner sprickor. Tanken är att denna metod skall ge en god beskrivning av bergets anisotropi och sprickors konnektivitet.

Rapporten beskriver koncept, antaganden, ekvationer och illustrerar nyckelegenskaper. Huvuddelen av rapporten är tämligen kort; ett antal appendix beskriver olika aspekter av programmet mer i detalj.

Contents

1 Introduction

1.1 Background

DarcyTools is a computer code for simulation of flow and transport in porous and/or fractured media. The fractured media in mind is a fractured rock and the porous media the soil cover on the top of the rock; it is hence groundwater flows, which is the class of flows in mind. The code is intended to be applicable to a wide range of groundwater flows, but the analysis of a repository for nuclear waste is the main intended application.

DarcyTools is developed by a collaborative effort by SKB (The Swedish Nuclear Fuel and Waste Management Company), MFRDC (Michel Ferry, R&D Consulting) and CFE AB (Computer-aided Fluid Engineering AB). It builds upon earlier development of groundwater models, carried out by CFE during the period 1990–2002. The following reports, give a general account of this work and hence give a background to the work to be described in this report:

- Groundwater flow at Äspö and changes due to the excavation of the laboratory (Svensson 1991). This report gives predictions of the influence of the laboratory *prior* to its construction.
- A regional analysis of groundwater flow and salinity distribution in the Äspö area (Svensson 1997a). Results from this study have been useful for generating boundary conditions for smaller scale models.
- A site scale analysis of groundwater flow and salinity distribution in the Äspö area (Svensson 1997b). This model may be considered as representing a synthesis of the detailed information provided in Rhén et al. (1997).
- Representation of fracture networks as grid cell conductivities (Svensson 1999a). This report describes, for the first time, the principles used for generating property fields in DarcyTools.
- A laboratory scale analysis of groundwater flow and salinity distribution in the Äspö area (Svensson 1999b). In this study the new methods were applied and evaluated.
- PARTRACK – A particle tracking algorithm for transport and dispersion of solutes in a sparsely fractured rock (Svensson 2001a). This report describes the particle tracking techniques used in DarcyTools.
- Impact of the tunnel construction on the groundwater system at Äspö. Task 5. Äspö Task Force on groundwater flow and transport of solutes (Svensson et al. 2002).

These reports give a general overview of the early developments that have lead to the present version of DarcyTools. It should also be pointed out that in the listed reports the CFD code PHOENICS (Spalding 1981) was used as an equation solver. DarcyTools is based on a solver called MIGAL (Ferry 2002). It has however been carefully evaluated that the two solvers produce very similar solutions and the reports listed are thus still valid as background reports for DarcyTools.

The present report will focus on the theoretical basis of DarcyTools. Two accompanying reports cover other aspects:

- Verification, validation and demonstration (Svensson 2010a) (Hereafter denoted Report 2).
- User's guide (Svensson and Ferry 2010) (Hereafter denoted Report 3).

Early "real world applications" of DarcyTools can be found in Svensson (2001c) and Follin et al. (2005, 2006).

Two basic approaches in groundwater modelling can be identified; in one we define grid cell conductivities (sometimes called the continuum porous-medium (CPM) approach, e.g. Jackson et al. (2000), in the other we calculate the flow through the fracture network (DFN approach). Both approaches have their merits and drawbacks, which however will not be discussed here (for a discussion, see Sahimi 1995). Instead we will try to combine the benefits of both approaches. This is done by transferring the hydraulic and geometric properties of a DFN to a CPM grid.

The traditional way to calculate grid cell conductivities in continuum models is through an upscaling procedure (for reviews see: Wen and Gómez-Hernández (1996), Renard and de Marsily (1997) and Pozdniakov and Tsang (1999)). These methods are however of no direct use in the present work. Attempts have been made, see La Pointe et al. (1995), Niemi et al. (1999) and Jackson et al. (2000), to use a DFN-model to calculate grid cell conductivities. These methods have similarities with the present approach as the cell conductivity will be based on the properties of a fracture network. We will however not use a flow simulation to estimate the grid cell conductivities; instead the fracture network is represented in the continuum model by a method based on the intersecting volumes between the fractures and the grid cells. Methods to include a limited number (say 10–20) of major deformation zones in a CPM-model have been presented, see for example Svensson (1991) and Gómez-Hernandez et al. (1999). The method in DarcyTools is different from these methods in that all fractures and deformation zones are considered, when the conductivity field is generated. This means that we may need to represent 10^6 to 10^8 fractures as grid cell conductivities. Further, if the properties (geometry, transmissivity, etc) of the major deformation zones are known, these zones are treated deterministically, while unknown, or background, fractures are generated from statistical distributions.

1.2 Objectives and scope

The objectives of this report can be summarised as:

- Provide the theoretical basis of DarcyTools.
- Illustrate how DarcyTools works.
- Discuss and evaluate the present status of DarcyTools.

A review of applications of DarcyTools is not made in the present report.

1.3 The Äspö HRL

The present report will not describe real world applications. Several references to model studies and field data related to Äspö Hard Rock Laboratory (HRL) will however be made and a brief introduction to Äspö HRL will therefore be given.

The Äspö Hard Rock Laboratory is located near the Oskarshamn nuclear power plant on the East Cost of Sweden, see Figure 1-1. The access tunnel starts on the mainland, continues under the Baltic and reaches the spiral part of the tunnel beneath the island of Äspö. The total length of the tunnel is 3,600 m and it reaches a depth of 460 m. A vertical elevator shaft connects the laboratory to the Äspö Research Village.

Mean precipitation minus evapotranspiration, P-E, has been estimated to be about 200 mm/year for the region. For the island of Äspö one can expect that the groundwater recharge (i.e. P-E) is smaller as the distance to the sea is shorter (no storage of water in lakes and ponds during periods of heavy precipitation). A value of 100 mm/year was used in the site scale model (Svensson 1997b).

Around the island of Äspö the Baltic Sea has a salinity of about 0.6%. It is known from boreholes on Äspö that the fresh water lens below Äspö has a thickness of 100 to 200 m under natural conditions; below this level the salinity increases to reach a value of about 2% at a depth of 800 m below ground. As the water density increases with salinity we have a density stratified water below the island of Äspö. This is an important feature of the groundwater flow system.

Three model domains are outlined in Figure 1-1; these will be referred to throughout the report.

The major fracture zones at Äspö are shown in Figure 1-2 and boreholes in Figure 1-3. These figures will be referenced to when field measurements are discussed.

1.4 Outline

The main part of the report is fairly short; this with the intention that the reader should be able to get a good overview of DarcyTools from a few hours of reading. The appendices will provide more detailed descriptions of various central topics.

1.5 Limitations

DarcyTools is developed continuously, both with respect to hardware developments (like multi-core platforms) and with respect to new features. Two new features which are not covered in the present version of the documentation are.

- Resaturation of the tunnel backfill. This feature is however well described in two separate reports (Svensson 2010c, Enssle and Poppei 2010).
- The ice, or permafrost, module. This feature is to be further developed and is for this reason not yet finally documented.

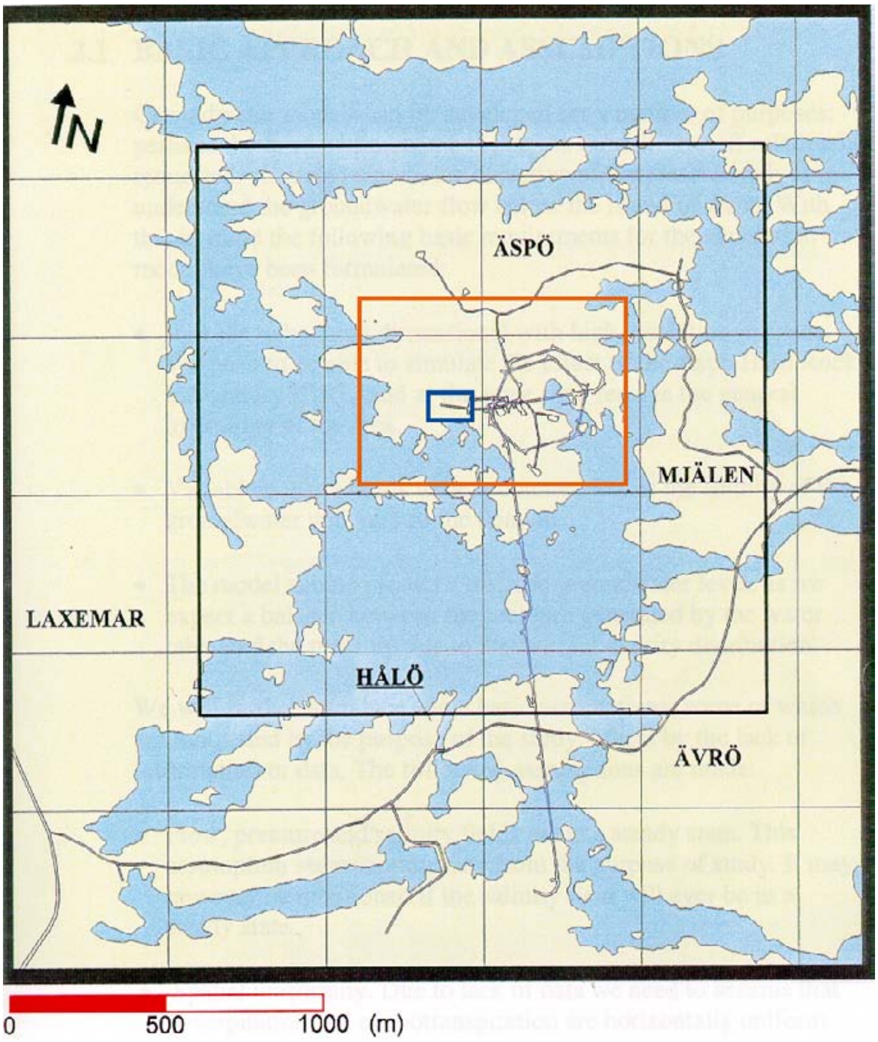

Figure 1-1. *The island of Äspö and the Äspö Hard Rock Laboratory. The black rectangle shows the area of the Site scale model (Svensson 1997b). The red rectangle shows the Laboratory model (Svensson 1999b) and the blue rectangle indicates the domain for the Repository model (Svensson 2001d).*

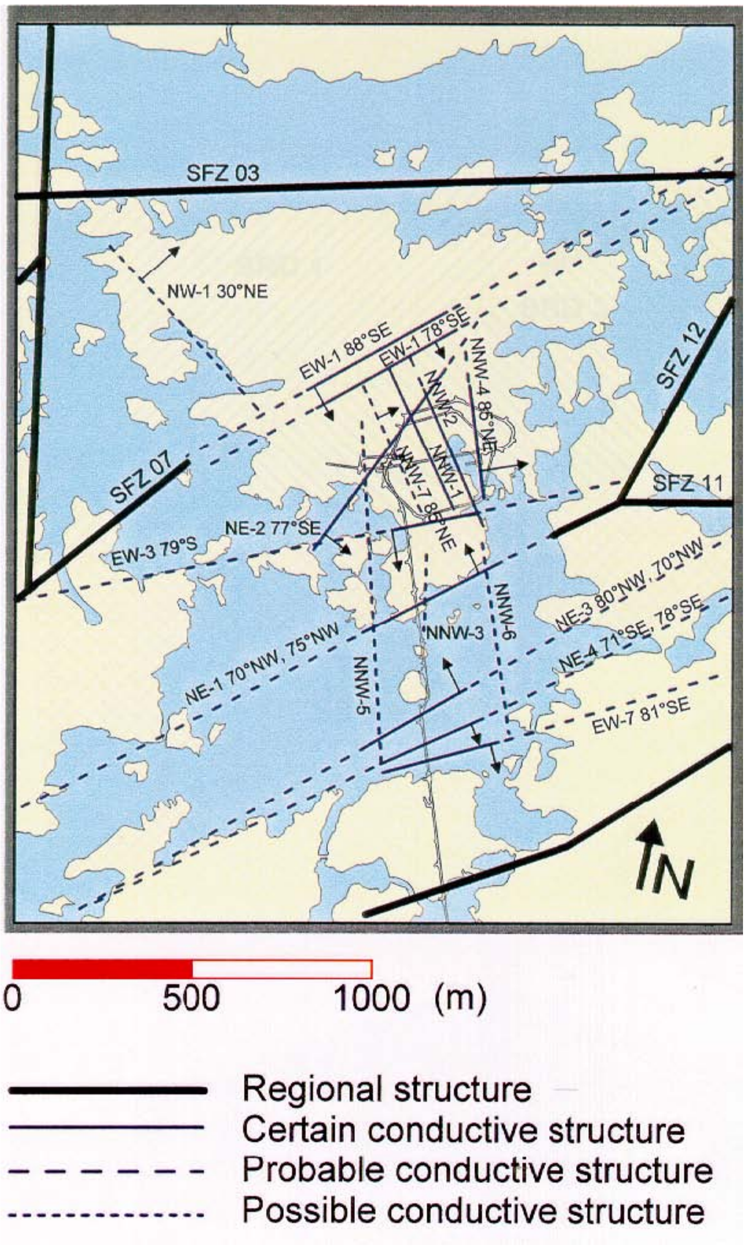

Figure 1-2. *Major fracture zones in the area, after Rhén et al. (1997).*

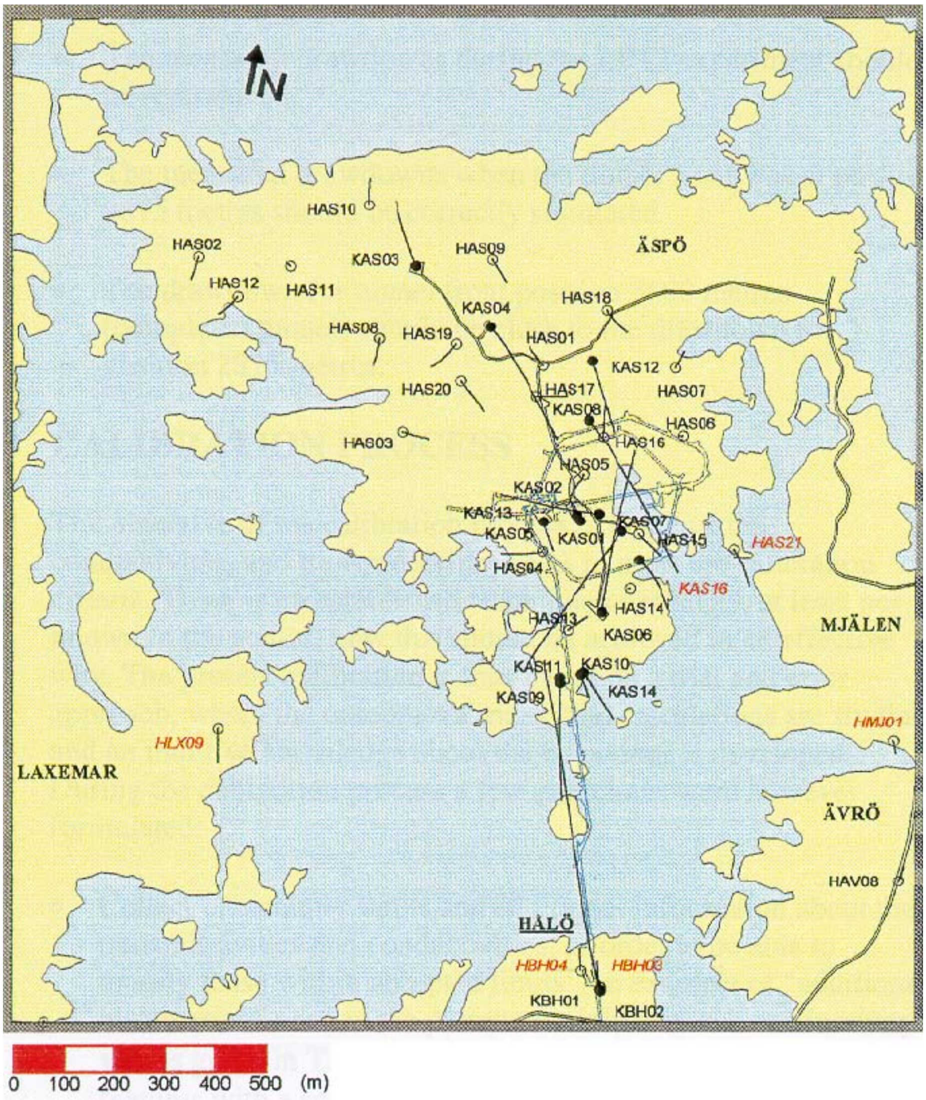

Figure 1-3. *Boreholes in the Äspö area, after Rhén et al. (1997).*

2 Situation considered

2.1 Introduction

As mentioned, the application area for DarcyTools is flow and transport in fractured and/or porous media. This section provides a general description of physical processes, scales, etc that need to be considered. The description is generic, but inspired by the conditions at and experiences from the Äspö Hard Rock Laboratory (HRL). Hence (sparsely) fractured rock is the hydrogeological medium in mind.

2.2 The 10 km scale view

The regional groundwater flow in unconfined aquifers introduces the concepts of recharge and discharge areas, see Figure 2-1. Recharge areas, i.e. where a net inflow is found, are usually found in topographically high places while the discharge areas are located in topographic lows. The discharge areas may take the form of a stream, river or a lake.

The general flow pattern is hence from high to low areas; a system of local flow cells is formed and the groundwater table follows the surface topography. However, this is an idealized picture which is based on the assumptions of a steady, constant density flow in a homogeneous aquifer. These assumptions are seldom fulfilled and care should hence be taken when interpreting field data, based on this view. In particular, most natural aquifers are anisotropic and heterogeneous.

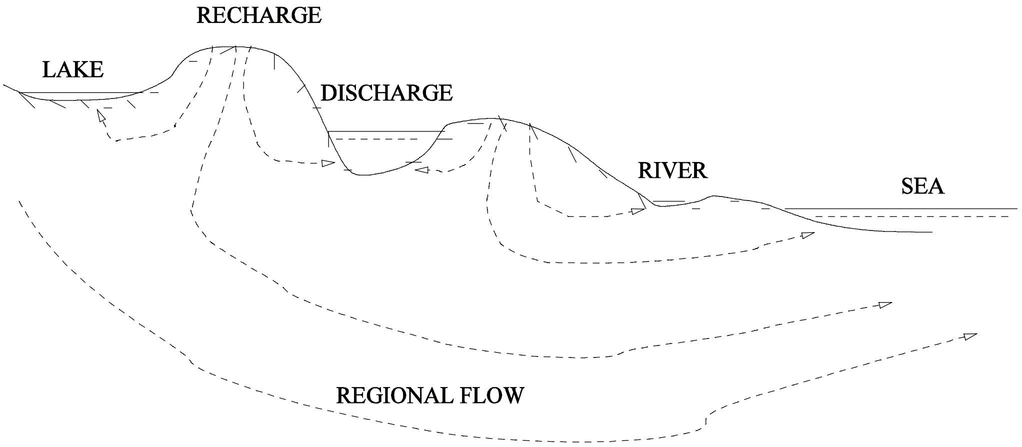

Figure 2-1. Situation considered – the 10 km scale view.

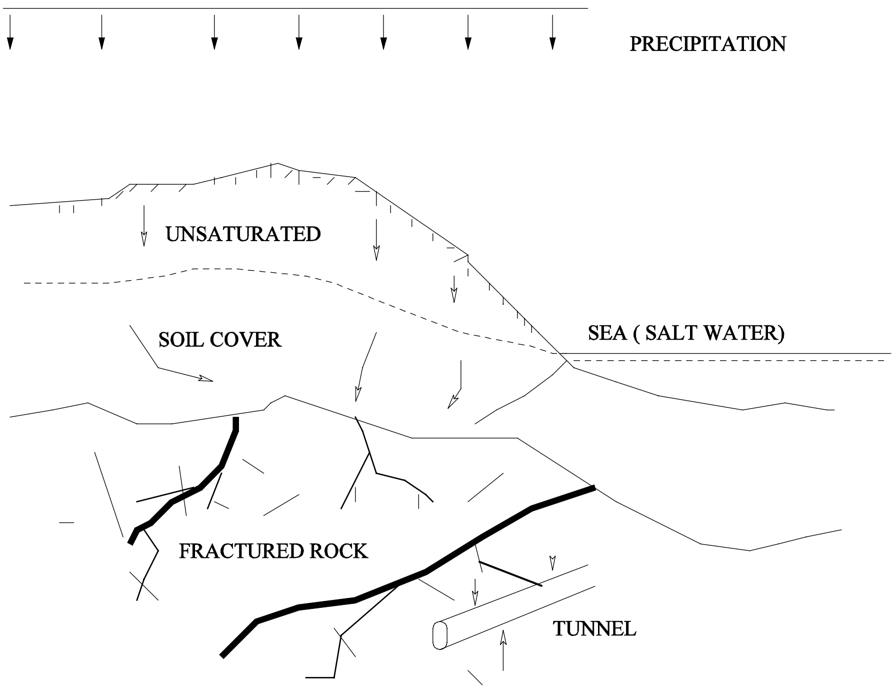

Figure 2-2. Situation considered – the km scale view.

2.3 The km scale view

A km scale view is given in Figure 2-2. Let us assume that it is of interest to determine the origin of water leaking into the tunnel. Two main sources are precipitation and sea water (excluding brine water from below). To track the precipitation water one has to follow a water parcel through the unsaturated zone, through the saturated soil cover and finally its way through the fracture network. It is essential to determine the position of the groundwater table, as it determines the pressure gradients in the porous media and may influence the conditions deep into the rock. The other source, the sea water, introduces density effects, as the seawater is heavier than fresh water. The heavier saltwater penetrates the coastal zone and modifies the pressure distribution (the Ghübern Herzberg relation). Due to this effect the inflow to the tunnel may be dominated by sea water *or* the precipitation water, all depending on the actual conditions (density difference, tunnel position, etc).

2.4 The m scale view

The main novel features of DarcyTools are concerned with the fracture network and we will therefore focus on the description of fractures (giving the porous media less attention). In Figure 2-3 part of a fracture network is shown. Different parts of the network have been marked with letters; these parts will now be described:

A: Represents a deformation zone. The deformation zone is assumed to be composed of a number of smaller fractures through which the flow takes place. Most of the small fractures do however not contribute to the flow but are still important for transport and

dispersion of a tracer. Deformation zones are often the main flow conductors due to their high transmissivity and size (length scale > 100 m). The thickness is typically > 1 m.

B: Some fractures are best characterised as “a single opening”.

Typically the thickness, or the aperture, is on the order of 10^{-3} m. The fractures marked with **B** in Figure 2-3 have a through-flow and may hence contribute to the total flow rate. If the transport time through the **B** fractures is different from the transport time in the fracture zone a dispersion effect will also result from the parallel flow path.

C: Isolated fractures of groups of fractures can not contribute to the flow, transport or dispersion, as flow in the matrix is neglected. In the numerical model these are removed before the generation of grid data is performed.

D: Some fractures, or deformation zones, may form "dead end systems". The exchange with fractures with a significant flow is then by molecular diffusion. When storage of water over long time periods, say longer than 100 years, is studied it is essential to represent the dead-end systems correctly.

E, F: There is always a lower limit on the fracture size that can be represented correctly in a numerical simulation. In the present study it will be assumed that fractures below a certain size, to be discussed, do not contribute significantly to the total flow. However, for transport and dispersion it is probably necessary to consider all scales, as a large fraction of the pore volume is expected to be due to the small scale features of the porosity field.

2.5 The mm scale view

It was mentioned above that the opening, or aperture, of a fracture is typically of the order of 1 mm or smaller. The aperture has however not a constant value, as is illustrated in Figure 2-4. On this scale it is useful to introduce the notion of the mobile zone, for the volume that has flowing water, and the immobile zone which represents all volumes with stagnant water. In Figure 2-4, the stagnant pools, the crossing fractures and the matrix may all contain stagnant water. The fracture may also contain material of various kinds, so called gouge material.

The geometrical complexity of a fracture opening is essential to consider when small scale dispersion processes are to be described. The exchange between the mobile and immobile zones is often assumed to be due to molecular diffusion only.

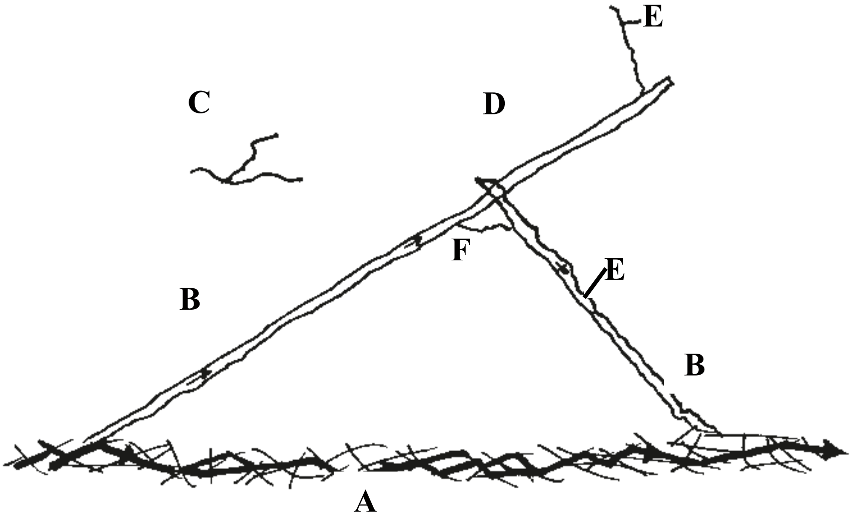

__Figure 2-3.__ Situation considered – the m scale view.

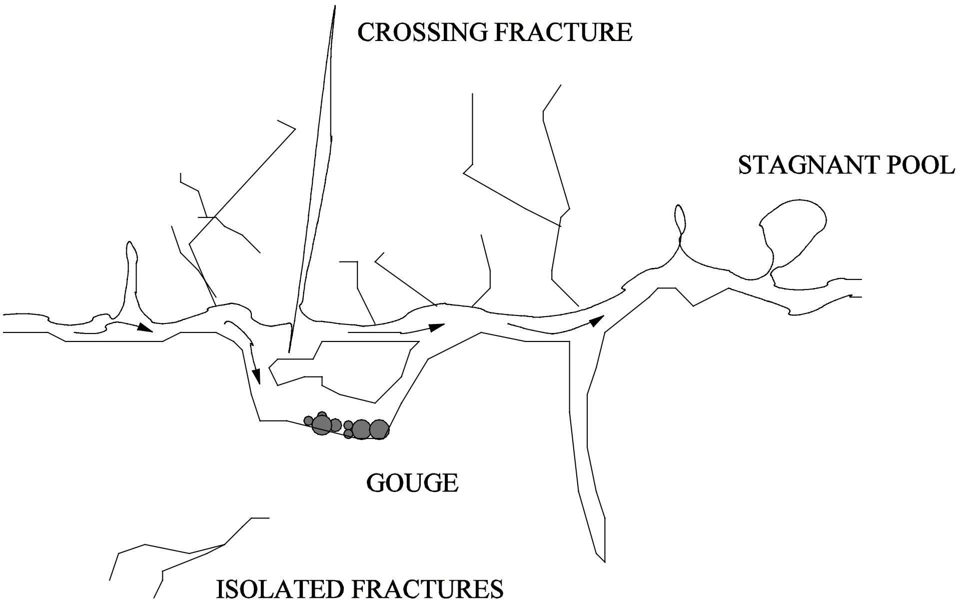

Figure 2-4. Situation considered – the mm scale view.

2.6 The flow system

If only the flow field is of interest, we do not need to consider the detailed properties of a fracture (as outlined in Figure 2-4). The fracture transmissivity is normally what is needed. In addition the following topics may be of importance.

- A method to handle the unsaturated zone is required. Depending on the situation at hand the method may range from quite simple (only position of the groundwater table) to complex two-phase algorithms.
- Density stratification. If waters of different densities meet, it is essential to account for the effects.
- In addition to the fracture transmissivities one needs information about the conductivity of the soil cover, if present.

These are some of the key elements that govern the flow system. Note that we at this stage are not discussing the required input to a numerical model, which of course is more extensive (boundary conditions, properties, etc).

2.7 Transport and dispersion

When discussing transport and dispersion of solutes it is useful to distinguish between two different problems with respect to the time scale. The first kind of problem is the field experiment with a time scale from weeks to perhaps a year. A longer time scale, which may be thousands of years, needs to be considered when the water types present in the fracture network is to be analyzed. At Äspö HRL, water from the last glaciation (about 11,000 years ago) has been found already at a depth of a few hundred metres. The relevant processes for the two problems will now be described, in turn.

Let us think of a typical cross-borehole tracer experiment where a tracer is injected in one borehole and the arrival in another, pumped, borehole is studied. The curve describing the time distribution of the concentration in the pumped borehole is called the breakthrough curve (BTC). Obviously the tracer is transported by advection between the two boreholes, and the flow field is hence an important element in the analysis. A number of dispersion processes will however affect the tracer as it travels through the fracture network. The most important of these are.

- **Intersections.** At a fracture intersection a tracer cloud may split up and enter pathways with different lengths and fluid velocities. This type of dispersion is often called macro-dispersion.
- **Channelling.** Spreading occurs within each fracture plane as the different streamlines have different path lengths and velocities. The flow channels may also merge or split up.
- **Taylor dispersion.** A velocity profile exists between the two bounding walls of the fracture. The resulting dispersion effect is called shear- or Taylor dispersion.
- **Matrix diffusion and sorption.** Interaction with the rock, stagnant pools and microfissures causes a number of processes that in effect lead to a delay and dispersion of a tracer pulse. These include: sorption on the fracture walls, diffusion into the rock matrix with sorption on inner surfaces and interaction with gouge.

As mentioned earlier, the diffusion into dead-end fractures of various sizes (see Figure 2-3 and 2-4) is by molecular diffusion. In order to illustrate the typical penetration depth for this process one may think of a substance with a certain molecular diffusion coefficiant ($D_{mol} = 10^{-10}$ m^2/s) and an experimental time scale of, say, one month ($t \approx 2.6\times10^6$ s). The penetration length can then be estimated as $\sqrt{D_{mol} \times t} = 0.016$ m. As the immobile zone is mainly made up of small fractures one can conclude that small scale dispersion is mainly governed by processes on the mm to cm scale.

For the transport problem on long time scales we may use the salinity field to illustrate some key features. First we can note the time scale for exchange in larger (> metres) dead-end fracture systems. If we put $D_{mol} = 10^{-10}$ m^2/s and $L = 10$ m, we find that the time scale is 10^{12} seconds, or 30,000 years ($t = L^2/D_{mol}$). It is thus not surprising to find water from the last glaciation, or the Litorina Sea (≈ 7,000 years BP), in the fracture system at Äspö HRL. Gravitational forces may further enhance the entrapment of water in dead-end zones. If, for example, Litorina water (which has higher salinity than the present Baltic water) is located in a dead-end fracture extending downwards from the mobile zone gravitational forces will enhance the entrapment. The same principle applies to glaciation water (which has a lower density than present Baltic water) in a dead-end fracture extending upwards from the mobile zone. If we further note that the volume of all immobile zones is larger than the volume of the mobile zone, one can draw the conclusion that the salinity field is "stiff" and requires very long time scales to reach a steady state. On a shorter time scale all processes listed above are of course also active for the dispersion of salt.

2.8 The transient nature of the problem

From the discussion of the salinity field one can conclude that the groundwater system is never in a steady state. Note that any change in the salinity field will modify the flow field as these are linked through the gravitational force.

In order to emphasize the transient nature of the problem the following list of processes have been compiled:

- **Glaciations.** Time scale of 10,000 to 100,000 years.
- **Diffusion into dead-end fractures.** Time scale from minutes to 100,000 years.
- **Sea level variations.** From daily variations to long time effects due to the land uplift.
- **Precipitation.** From daily, seasonal to yearly variations.
- **Tidal effects.** Time scale of one day.

The list can be made longer, but the message is probably clear: "transient effects on a variety of scales need to be considered".

2.9 Summing up

The intention of this chapter was to describe the problem considered in a general way. One may however put emphasis on different aspects of the problem (the important area of two-phase flows has for example not been mentioned, nor have the storativity and specific yield effects been described). It should also be noted that the description given has some bias towards issues of interest to nuclear waste repositories, although the ambition was to give a general account of the problem.

Based on the qualitative descriptions given the following consensus statement is formulated:

- Flow, transport and dispersion in a sparsely fractured rock are governed by processes that have time scales ranging from minutes to thousands of years and space scales ranging from millimetres to several kilometres. The coupling between scales, in space and time, is strong and it is generally not possible to neglect these interactions.

3 Concepts, Assumptions and Methods

3.1 Introduction

The qualitative description of the previous chapter sets the scene for the concepts, assumptions and methods to be introduced in this section. If the previous section was general, the present chapter is very specific for DarcyTools. The descriptive presentation method will however be continued, leaving the mathematics to Chapter 4. We will hence not try to "prove" the correctness of the concepts, assumptions and methods, as this will be the objective of a separate report (Report 2).

First a key assumption in DarcyTools will be presented, then the fracture network and its representation in the grid (including subgrid processes) is discussed. After this concepts related to transport are reviewed, then the groundwater table is discussed and finally some assumptions regarding properties are given.

3.2 The key assumption

The most fundamental assumption in DarcyTools is related to the structure of the fracture network, which is assumed to follow a power law distribution. More precisely it is assumed that the number of fractures per unit volume, n, in the length interval, dl, is given by:

$$n = \mathrm{I} * \left[\left(\frac{l + dl}{l_{ref}} \right)^{a} - \left(\frac{l}{l_{ref}} \right)^{a} \right] / a \qquad (3\text{-}1)$$

where I is the intensity, l_{ref} a reference length and a the power law exponent. Depending on how I and a are chosen, networks with different characteristics can be generated. In DarcyTools simulations it will often be assumed that $a = -2.6$ (following La Pointe et al. 1999) and that I is given avalue resulting in a "sparsely fractured rock" (details later). This is the situation at Äspö HRL (Rhén et al. 1997), where the major deformation zones have been thoroughly studied and it is believed that they provide the "first order" response in, for example, a pump test (Stanfors et al. 1999). The length scale of the major deformation zones is typically above, say, 300 m and the transmissivity is of the order of 10^{-5} m^2/s. Deformation zones smaller than 300 m have also been mapped at Äspö, and found to be hydraulically important, and should hence also be considered in the conductivity field. DarcyTools is developed for a fracture network of the kind found at Äspö HRL. Sometimes the intensity parameter is related to fracture surface area, P_{32}. It is possible to relate I to P_{32}, see Follin et al. (2005).

From this assumption of a sparsely fractured network, it follows that the flow is distributed on relatively few flow channels, as it is the large scale fractures and zones that provide the connectivity in the network. In DarcyTools it will be assumed that all essential flow channels can be described in the computational grid. However, as discussed above, dispersion is often dominated by processes on the mm scale, which can not be described explicitly. This Separation Of Scales (SOS-concept) is a consequence of the sparsely fractured rock and will form the basis for the subgrid model to be described.

3.3 Concepts used for fracture descriptions

The real world fracture network will be represented as a system of conductive elements and storage volumes, see Figure 3-1 (which is based on Figure 2-3). As mentioned, not all fractures can be represented in the generated fracture network. The smallest fracture size, l_{min}, is chosen to be comparable to cell size, Δ, in the computational grid. Fractures smaller than l_{min} will be represented as storage volumes, which are defined as volumes that are in contact with the flow channels and exchange matter with these by molecular diffusion. Note that fracture **F** in Figure 3-1 will not be represented as a flow channel in the generated network, as it is supposed to illustrate a fracture smaller than l_{min}.

Each of the conductive elements (A, B and D in Figure 3-1) is assumed to have a thickness, b_e, conductivity, K_e, kinematic porosity, θ_e, flow wetted surface, a_w and diffusion coefficient, D_e. The storage volumes (E and F in Figure 3-1) are described by their linear dimensions, volumes and diffusion coefficients. Below, it will be discussed how these parameters can be estimated.

If the open space in a fracture can be described as "the space between two parallel walls" it is easy to estimate the flow wetted surface (FWS); it will be 2 $m^2/(m^2$ fracture). If the fracture is very irregular or have parallel flow channels it is harder to estimate a realistic value. In DarcyTools the FWS will be given as an input parameter for each major (or deterministic) fracture zone and each group of random fractures.

All properties (conductivity, porosity, diffusivity and FWS) are assumed to be uniformly distributed over the thickness of the conductive element.

Some nomenclature for fractures needs to be introduced. A fracture that has one single opening will in the following be called a single fracture, while a deformation zone consists of several crossing fractures. For a single fracture we call the width of the opening the aperture, which is typically less than 10^{-3} metres. For a deformation zone, the thickness is on the order 10–100 m. In the present study, we will make no distinction between a single fracture and a deformation zone; both are idealized as an element with thickness and length. If the transmissivity of the single fracture, or the deformation zone, is denoted T we can define the hydraulic conductivity of the element as $K = T/b$. In the following we will call the conductive element a fracture for short.

A few more things can be noted in Figure 3-1:

- isolated fractures, **C**, are removed in the generated fracture network,
- the deformation zone, **A**, may have a varying thickness in the generated network. A method to generate conductive elements with varying thickness has been developed (described in Appendix C), but this method can presently only be used for major deterministic deformation zones (often 15–20 in number) as it is time-consuming on the computer.

3.4 Representation of properties on a grid

Most numerical models of groundwater flow subdivide the studied domain into smaller volumes. If a computational grid is defined, we call these smaller volumes grid cells, and we apply the conservation laws and other constitutive relations to these. Also material properties, like hydraulic conductivity and porosity, need to be specified for the grid cells. Often these properties are measured on a smaller scale (support scale) and a technique to express these on the scale of the grid cells is thus needed (upscaling). When material properties for all grid cells have been obtained, the flow simulation can be performed. In DarcyTools, we will however not follow this traditional route and the main argument for this can be stated as follows:

- In a sparsely fractured rock it is believed that most of the flow is due to a limited number of major fractures and deformation zones. The main task is thus to identify these and to represent them in the numerical model. If refined modelling is required, the next size class of fractures or deformation zones should be considered. From this point of view it seems more logical to first consider large fractures, and then progressively smaller ones, than to upscale properties from a small scale.

It is not possible to represent all fractures in the grid, simply because there are too many. In DarcyTools the smallest fracture considered will often be of the same size as the grid size. Smaller fractures, $l < l_{min}$, are however also of importance (for dispersion) and in DarcyTools represented as storage volumes (immobile zones), see Figure 3-2. In fact, storage volumes are defined as *all* immobile zones , with $l < l_{min}$, that exchange matter with the flowing water by molecular diffusion only.

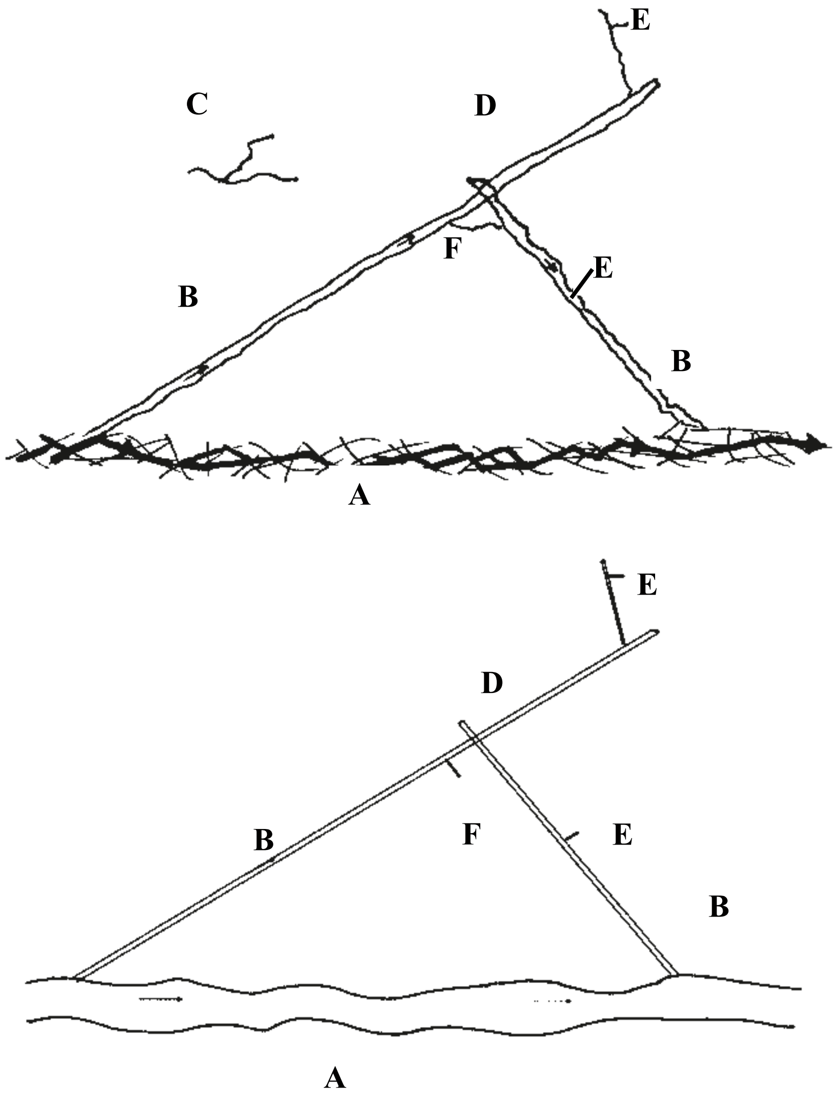

Figure 3-1. Representation of the real world fracture network (top) as conductive elements and storage volumes.

We have thus subdivided all fractures in contact (isolated fractures are not considered) into conductive elements and storage volumes. Storage volumes will be treated as subgrid effects and are represented in the subgrid model FRAME, to be described below. Conductive elements are represented as grid properties by the GEHYCO method which can now be formulated as:

- A conductive element contributes to the grid value of a variable by an amount which is equal to the intersecting volume times the value of the variable in question. Contributions from all elements that intersect the control volume are added and the sum is divided by the volume of the cell.

This basic principle will now be explained and illustrated, using Figure 3-3. A conductive element of thickness b is crossing a computational grid, which has a cell size of Δ. A staggered grid is to be used, which means that scalar quantities, like pressure and salinity, are stored at cell centres while velocity vectors are stored at cell wall centres, see Figure 3-3. This grid arrangement was first introduced by Harlow and Welch (1965) and is described in textbooks, see for example Patankar (1980). Each variable is assumed to be representative for a certain control volume, which is the volume the discretized equations are formulated for. For a velocity cell it is clear that the driving pressure force can be easily formulated. As we are going to apply the Darcy law to the velocity cell we also need a relevant cell conductivity to obtain the cell wall velocity. How to calculate this conductivity, and other properties, is the main subject of the GEHYCO method.

To obtain the porosity, as an example, of the scalar cell marked in Figure 3-3 the following steps are performed.

- Calculate the intersecting volume between the conductive element and the cell; this volume is marked in the figure.
- If the porosity of the conductive element is θ_e, the contribution to the free volume is $\theta_e V_i$, where V_i is the intersecting volume.
- Calculate the contributions from all conductive elements that cross the cell.
- Obtain the cell porosity as the sum of all contributions divided by the cell volume.

In Figure 3-3 a control volume for a velocity cell is also marked. The procedure to obtain the conductivity for this control volume is analogue to the steps above.

By this procedure the porosity, flow wetted surface and storativity are determined for all scalar cells and the conductivities and diffusivities for all cell walls.

An assumption in the statement above is that "contributions from all elements that intersect a cell are added". If two, or more, fractures intersect a velocity cell, the cell conductivity should represent a fracture intersection (neglecting the case of parallel fractures of various orientation). Neretnieks (1993) discusses various concepts about channelling at intersections, but concludes that no firm information is available. He cites however a number of observations that support the idea that "fracture intersections form easy pathways". In lack of any firm information, it will therefore be assumed that contributions can be added. Fracture intersections will hence form "easy pathways".

The basic principle of the GEHYCO method is obviously very simple but, as will be demonstrated, still general enough to handle even complex fracture networks. A few properties of the method can already at this stage be identified:

- All cell wall conductivities will be different, as we generate three conductivity values (in a 3D case) for each scalar cell (the normal terms of the tensor). In fact, all six cell wall conductivities will be different, but only three are considered to belong to each cell; the others belong to neighbouring cells. A conductivity field that is anisotropic on the cell scale is hence always generated.
- A fracture smaller than the cell size can not generally contribute to the anisotropy or correlation of the conductivity field.

Some simple calculations that illustrate the GEHYCO method, and also demonstrates the accuracy that can be expected, can be found in Appendix G.

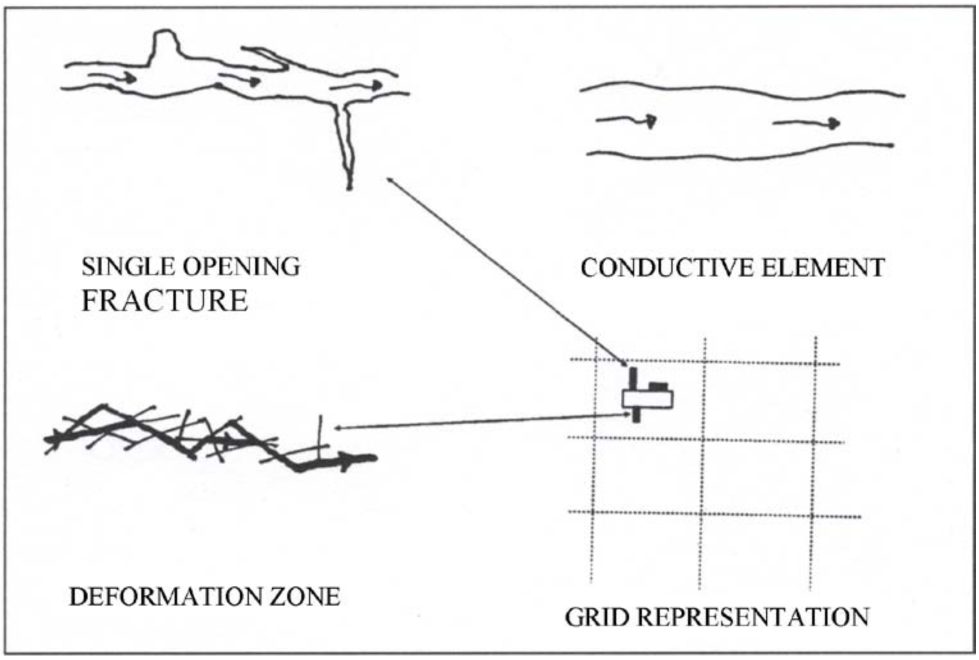

__Figure 3-2.__ Representation of kinematic (or mobile) and storage (or immobile) volumes in the grid. The open rectangle in the grid represents a kinematic volume (generated by the conductive element), while filled rectangles represent storage volumes. The single opening fracture and the deformation zone are hence both represented as a conductive element, which has no storage volumes.

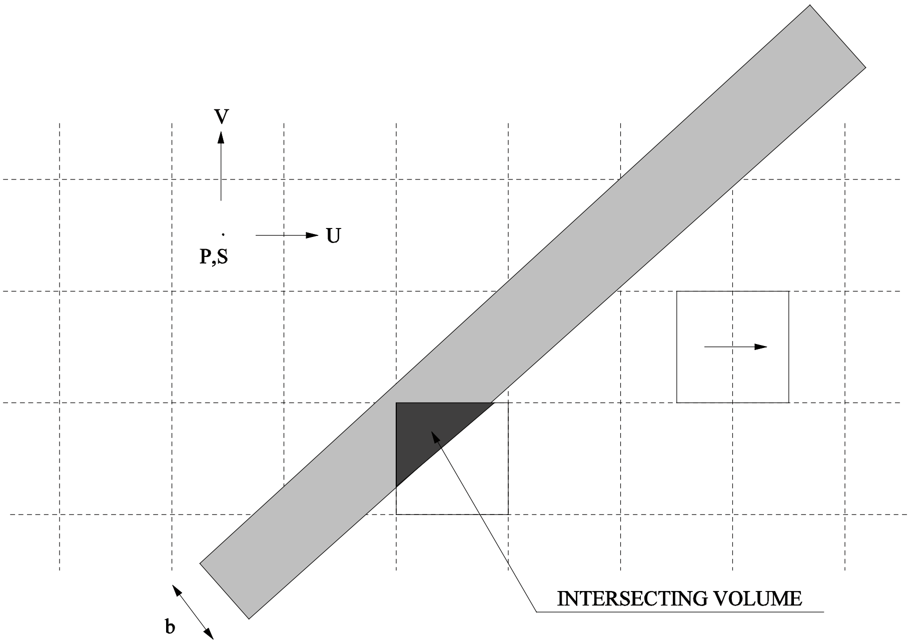

__Figure 3-3.__ Illustration of concepts and methods for calculating grid properties.

3.5 Subgrid processes, FRAME

In Figure 3-4 some subgrid processes and concepts are introduced. Let us consider a computational cell with a through flow, i.e. a cell with a flow channel. The flow "sees" a certain surface area, the flow wetted surface (FWS), as it passes the cell. The FWS may bring the flowing water in contact with other fractures, gouge material, stagnant pools, etc. Most of these volumes can be expected to have stagnant water and mass exchange is hence due to molecular diffusion. For a stagnant pool the relevant diffusion coefficient may be that for pure water, while diffusion into crossing fractures and the rock matrix may proceed with a diffusion rate that is several orders of magnitude smaller. As above, we will call the volume with flowing water the mobile zone and the volumes with no advection the immobile zone. Fractures and volumes which are not in contact with the mobile zone are of course of no relevance and can be excluded from the discussion.

The situation outlined in Figure 3-4 is quite complicated and does not lend itself to direct descriptions of individual processes. In order to derive a simple model that can be employed in large (many grid cells) 3D models, the following basic assumption will be made:

- The immobile zones can be represented by a set of boxes, each with its own length scale, volume and effective diffusion coefficient.

The idealized problem is illustrated in Figure 3-5. The box with the smallest length-scale (dimension perpendicular to the mobile zone) will have the largest diffusion coefficient and normally also the largest contact area with the mobile zone. This volume will hence have a fast response. The actual response time can be estimated from the length scale, l, and the effective diffusion coefficient, D_e, as:

$$t \approx \frac{l^2}{D_e}$$

For $l = 10^{-3}$ m and $D_e = 10^{-10}$ m^2/s the time is 10^4 s (≈ 3 hours). For l= 1 m and $D_e = 10^{-12}$ m^2/s the time will be 10^{12} s (30,000 years), which illustrates that both short and long time scales may be treated within the same concept. In the following we will call these boxes storage volumes, which thus represent an idealized view of the immobile zones.

The next step is to devise methods to calculate the FWS, storage volumes, diffusion coefficients, etc. Fractal scaling laws will be used in this context and as we have adopted a multirate diffusion approach we call the subgrid model FRAME (a subgrid model based on FRActal scaling laws and Multirate Equations). Methods to derive the FWS are described in detail in Appendix E, and here we will focus on the properties of the storage volumes. The following steps will determine these.

- Divide the immobile volumes, illustrated in Figure 3-4, into a number of size groups with respect to the length-scale.
- Generate the number of fractures in each size group from a power-law with exponent a (fractal dimension). Note that the same power-law as used for the resolved fracture network is used also for the subgrid system. This will give the number of fractures per m^3, for the size group in question.
- Only immobile zones in contact with the FWS can be in contact with the mobile zone. Modify the number of fractures in each size group with respect to this constraint.
- Assume that the aperture of a fracture is proportional to the length scale, i.e. $e_T \sim l^\gamma$. Note that for $l \approx l_{min}$, it can be expected that the immobile zones are due to fractures. For $l \approx l_{min}$ the volumes are perhaps due to stagnant pools and it may be questionable to speak about an aperture.
- The effective diffusion coefficient, D_e, is expected to be close to the molecular value for water, D_m, for the smallest volumes and then show a decreasing trend with the length scale of the immobile zone. The following relation is assumed:

$$D_e = D_m \left(\frac{l}{l_{\min}} \right)^{\Psi}$$

By these steps the volume, contact area and effective diffusion coefficient have been determined for each storage volume, as a function of a, γ and Ψ. However, these parameters will not be specified individually as they can be related to the "late time slope of the breakthrough curve"; this will be further discussed in Chapter 4 (see also Appendix B), where the details of the model implementation are described.

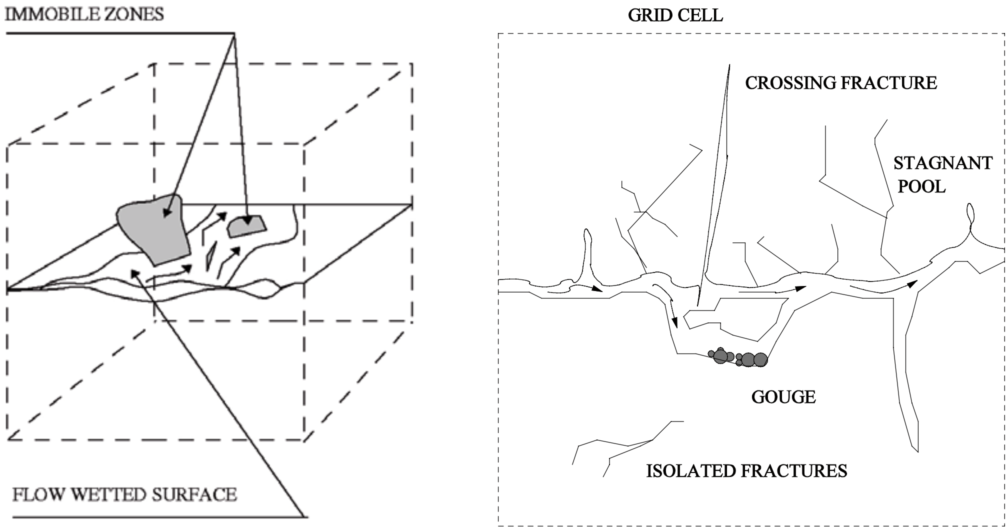

Figure 3-4. Illustration of subgrid processes and concepts.

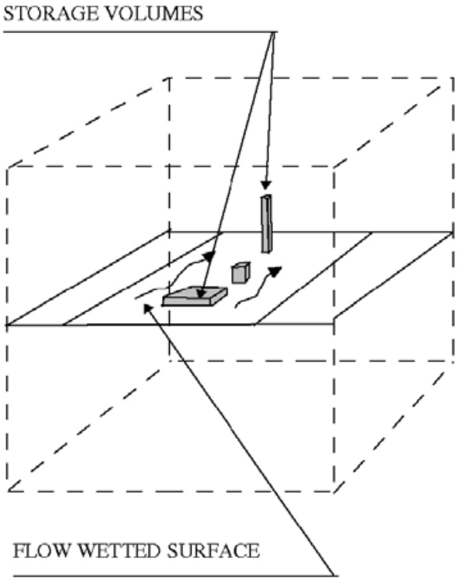

Figure 3-5. The assumed structure of subgrid volumes and areas.

Regarding the size interval to be considered, it was shown above that a length scale of 10^{-3} m results in a storage volume that has a response on the order of a few hours. Smaller, or faster, boxes are probably not required, unless a very fast experiment is to be simulated. The upper limit should be the cell size, Δ, as larger fractures are normally treated explicitly in the resolved fracture network. However, Δ is often in the range 1–10 m and the largest storage volume will hence be very slow. From a practical point of view (save computer time) the upper limit may hence be chosen with respect to the time scale of the problem considered. Note also that fractures in the resolved network may form dead-end systems that exchange matter with the flowing water by molecular diffusion only.

The concepts and assumptions introduced give a very simplified view of the expected subgrid processes. However, it should be remembered that the objective is to derive a subgrid model that can be employed in large 3D, transient models.

3.6 Transport

DarcyTools has two built-in options for transport simulation; a particle tracking algorithm, PARTRACK, and advection/dispersion equations. The reasons why two methods are needed are based on the following assumptions.

- Salinity. The salinity field strongly influences the flow field through the density field. It is difficult to describe the salinity field by a set of particles and an advection/dispersion equation is therefore the best choice.
- Temperature. The main heat flux component is conduction and an advection/dispersion equation is hence the obvious choice for this variable. It will further be assumed that the water and rock is always in thermal equilibrium and only one temperature is thus solved for.
- Tracers. Simulation of tracer transport is best performed with a particle approach as this method is free from numerical dispersion effects. It is also possible to treat sorbing tracers (like radionuclides) with this technique.

These are the main scalars that need to be considered in applications. If additional scalar simulations are requested a decision about the most appropriate method has to be taken.

Transport of salt and tracers are assumed to be restricted to the water phase. Dispersion is hence due to mixing at fracture intersections (macro dispersion) and exchange with immobile zones (micro dispersion, as embodied in FRAME). FRAME is hence developed for both the advection/dispersion equation (as used for salt) and PARTRACK (as used for tracers).

3.7 Groundwater table

As was stated in Chapter 2, the groundwater table may determine the pressure field deep down into the rock. Unfortunately it is not straight forward to calculate the position of the groundwater table. From the literature two methods are available:

- The variably saturated approach, which means that the unsaturated zone is included in the simulation and that the so called Richards equation is solved.
- Free surface approach. The main assumption of the method is that the conditions in the unsaturated zone do not significantly affect the position of the groundwater table.

A novel method to determine the groundwater table, which is in between these two, is introduced in DarcyTools. The basic idea is as follows: If a simulation like the one in Figure 3-6 is performed without taking any notion of the groundwater table a certain pressure distribution results. A surface with atmospheric pressure is calculated, but pressure gradients and hence a horizontal flow is calculated above this surface. As the hydraulic conductivity is significantly smaller for the region above the surface with the atmospheric pressure this is obviously not correct. The key feature of the method is to prevent the horizontal flow above the surface of atmospheric pressure by simply reducing the horizontal conductivity. This is done in an iterative manner, meaning that the position of the atmospheric pressure is determined and horizontal conductivities are recalculated (note that if a rising surface is calculated, the horizontal conductivities below the surface should be restored to the fully saturated values). It can be shown, see Report 2, that this method gives a steady state groundwater table that is in agreement with available analytical solutions.

The transient problem introduces a new feature; if the groundwater table is lowered a delayed drainage of the volumes above the water table will occur. A significant amount of water can be released and affect the position of the water table. In DarcyTools this *specific yield effect* is described by a source term in the mass balance equation:

$$Q_{sy} = k_{sy} V_{sy}\,(t)\ [\mathrm{m^3/s}]$$

$$\frac{dV_{sy}}{dt} = -Q_{sy}$$

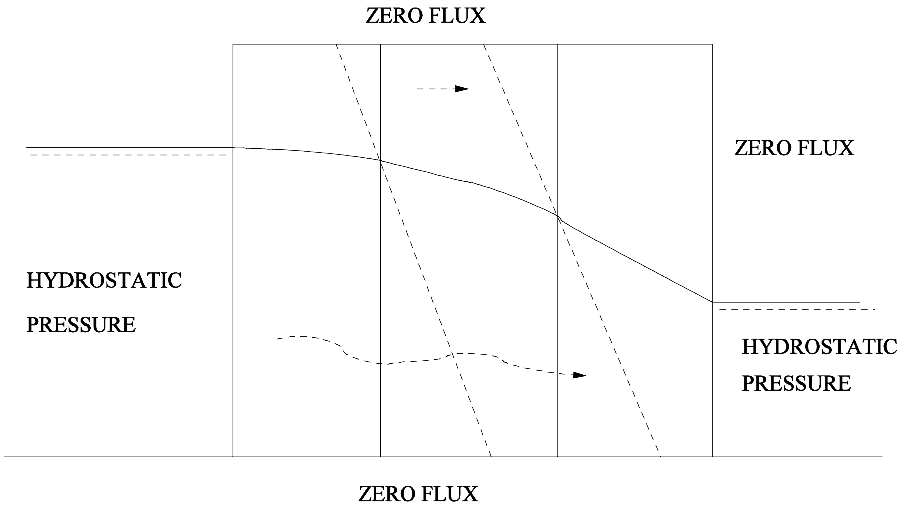

Figure 3-6. *Illustration of concepts used for determination of the groundwater table. The dotted inclined lines indicate pressure distributions, with pressure <0 above the groundwater table.*

where V_{sy} is the volume of drainable water at time t and k_{sy} a time constant for the drainage. We thus keep track of the drainable water in each cell above the water table and let this water be transported, by gravity, down to the water table. In Report 2, it is shown that this approach gives results that are in fair agreement with available analytical solutions. However, the method is not computationally effective and therefore not recommended for general use. A tentative suggestion is to instead use the storativity term to model the effect. In Report 2 (Case B6) this method is tested.

3.8 Porosity and state laws

Finally, we will briefly review some assumptions related to the properties of the media and the fluid.

The porosity field is based on the porosities ascribed to the conductive elements. In the analysis of the resulting porosity field it is however of interest to also characterize the porosity as based on the volume of the computational domain. For this reason the following definitions will be used:

- θ_a is the porosity based on all generated fractures, including isolated fractures or clusters of fractures.
- θ_c is the connected part of θ_a, i.e. isolated fractures and clusters have been removed.
- θ_f is the part of θ_c that has a significant flow, i.e. stagnant volumes have been removed.

θ_f requires a definition of what should be called "stagnant volumes". The definition to be adopted here is:

- If the stagnant parts of the kinematic porosity field are neglected, i.e. the porosity is put to zero, this should result in a reduction of the flow through the domain that is smaller than 1%. This should be fulfilled for pressure gradients in all three coordinate directions.

These porosity measures will be further analyzed in Section 7.3.

Other media properties are flow wetted surface and storativity. Also these will be calculated as grid cell data, based on the ascribed values to the conductive elements. In the fracture network the conductivity of conductive elements is specified; this because input data are often given as a transmissivity, T, and a thickness, b, and the conductivity is then T/b. In the simulation model the permeability is however used as the influence of fluid properties needs to be taken into account.

State laws for water that take into account the effects of pressure, temperature and salinity are very complex indeed. For the present range of applications, it is expected that the following assumptions are adequate:

- Density is linearly and quadraticly (i.e. two terms) related to both salinity and temperature.
- Viscosity is linearly and quadraticly (i.e. two terms) related to temperature.
- Specific heat of mass is linearly and quadraticly (i.e. two terms) related to salinity.

As the user will have access to the coefficients of these relations, details in next chapter, it is expected that it will always be possible to tune the relations to a specific application, with a high degree of accuracy.

4 Mathematical formulation

4.1 Introduction

First the conservation and state laws will be presented and then, as in the previous sections, various features will be dealt with; now with focus on the mathematical formulation.

In Section 4.2, temperature has been denoted *T*, which elsewhere is used for transmissivity.

4.2 Conservation and state laws

Conservation of mass:

$$\frac{\partial \rho\theta}{\partial t}+\frac{\partial}{\partial x}(\rho u)+\frac{\partial}{\partial y}(\rho v)+\frac{\partial}{\partial z}(\rho w)=Q \tag{4-1}$$

where ρ is fluid density, θ porosity, u, v and w Darcy velocities and Q a source/sink term. The coordinate system is denoted x, y, z (space) and t (time).

Mass fraction transport equation:

$$\begin{aligned}\frac{\partial \rho\theta C}{\partial t} &+ \frac{\partial}{\partial x}\left(\rho u C-\rho\gamma D_x\frac{\partial C}{\partial x}\right)\\ &+\frac{\partial}{\partial y}\left(\rho v C-\rho\gamma D_y\frac{\partial C}{\partial y}\right)\\ &+\frac{\partial}{\partial z}\left(\rho w C-\rho\gamma D_z\frac{\partial C}{\partial z}\right)=QC+Q_C\end{aligned} \tag{4-2}$$

where C is transported mass fraction, D_x, D_y and D_z the normal terms of the diffusion-dispersion tensor and Q_c a source/sink term, that represents the exchange with immobile zones. Q_c is determined by the subgrid model FRAME. Note that the diffusion coefficients are the effective coefficients that include the porosity, see further explanation of the diffusion term in connection with Equation 4-11 below.

Conservation of heat:

$$\begin{aligned}\rho\theta\frac{\partial c_p T}{\partial t} &+ \frac{\partial\,(1-\theta)cT}{\partial t}\\ &+\frac{\partial}{\partial x}\left(\rho u c_p T-\lambda_x\frac{\partial T}{\partial x}\right)\\ &+\frac{\partial}{\partial y}\left(\rho v c_p T-\lambda_y\frac{\partial T}{\partial y}\right)\\ &+\frac{\partial}{\partial z}\left(\rho w c_p T-\lambda_z\frac{\partial T}{\partial z}\right)=\left(\frac{\partial\rho u}{\partial x}+\frac{\partial\rho v}{\partial y}+\frac{\partial\rho w}{\partial z}\right)c_p T+Q_T\end{aligned} \tag{4-3}$$

where λ_x, λ_y and λ_z are the normal terms of the equivalent (i.e. rock with fluid) thermal conductivity tensor, c is the rock thermal capacity and c_p the specific heat of the fluid and Q_T a source/sink term. We are hence only solving for one temperature, assuming thermal equilibrium between the rock and the water. Note that we have chosen to use c (Joule/m^{3}°C) for the rock thermal capacity and c_p (Joule/kg°C) the specific heat of the fluid. The reason for this inconsistency is that this formulation does not require the rock density as an input variable.

The mass conservation equation is turned into a pressure equation under the well known Darcy's assumption:

$$\rho u = -\frac{K_x}{g}\frac{\partial P}{\partial x}$$
$$\rho v = -\frac{K_y}{g}\frac{\partial P}{\partial y} \qquad (4\text{-}4)$$
$$\rho w = -\frac{K_z}{g}\frac{\partial P}{\partial z} - K_z(\rho - \rho_0)$$

where K_x, K_y and K_z are the local hydraulic conductivities in x, y and z direction, g the gravity acceleration, ρ_0 a reference fluid density and P the dynamic fluid pressure relative to the reference hydrostatic pressure.

$$P = p + \rho_0 g\, z \qquad (4\text{-}5)$$

where p is the total pressure. The hydraulic conductivity, K, is related to the permeability, k, by the relation,

$$K = \frac{\rho g k}{\mu} \qquad (4\text{-}6)$$

where μ is the dynamic viscosity.

The fluid properties like the dynamic viscosity, μ, the density, ρ, and the specific heat, c_p, are given by state laws:

$$\mu = \mu_0\left[1 + a_1\left(T - T_\mu\right) + a_2\left(T - T_\mu\right)^2\right]^{n_\mu} \qquad (4\text{-}7)$$

$$\rho = \rho_0\left[1 + \alpha_1 S + \alpha_2 S^2 - \beta_1\left(T - T_\rho\right) - \beta_2\left(T - T_\rho\right)^2\right] \qquad (4\text{-}8)$$

$$c_P = c_{P0}\,(1 + b_1\, S + b_2 S_2 \qquad (4\text{-}9)$$

while the porosity θ and the compaction, γ, of the matrix are given the following dependencies:

$$\theta = \theta_0\,\gamma \qquad (4\text{-}10)$$

$$\gamma = 1 + (\sigma/\theta_0)\,(P - P_0)/\rho g \qquad (4\text{-}11)$$

In the above formulas S represents the salinity (salt mass fraction), θ_0 a reference porosity field given for a reference pressure field P_0 and σ the specific storativity field. n_μ, a_i, b_i, α_i, β_i, μ_0, ρ_0, c_{p0}, T_μ and T_ρ are constants.

In the advection/diffusion Equation 4-2, it is common to write the diffusion coefficient as θD_{mol}, where D_{mol} is the molecular diffusion coefficient. In DarcyTools we choose to write the term as $\theta D_{mol} = \theta_0\gamma D_{mol} = \gamma D$, where D is now the effective diffusion coefficient. The reason is that it is the effective diffusion coefficient that is specified for a conductive element and the GEHYCO-algorithm will hence deliver effective diffusion coefficients for cell walls. When a porous media case is simulated and the diffusion coefficients are specified, one thus needs to remember that it is the effective coefficients that should be given.

4.3 Fractures and fracture network

The relations to be discussed below are not an integral part of DarcyTools as they can be altered based on site specific information. It is hence more an illustration of the input data required. The relations given are largely based on data from Äspö HRL.

Fracture properties. The relations used to determine fracture properties, like transmissivity and porosity, are taken from a tentative evaluation/ compilation (Appendix F). The following summarises the main relations:

- Transmissivity-fracture size:

$$T = \begin{cases} 10^{-5}(l/100)^2 & \left[m^2/s\right] \quad \text{for } l \leq 100\text{m} \\ 10^{-5} & \left[m^2/s\right] \quad \text{for } l > 100\text{m} \end{cases} \qquad \text{(4-12)}$$

where T is transmissivity and l fracture size. The coefficients of this relation are accessible to the user and it is also possible to include a random term in the relation, see Report 3 for details.

- Transmissivity-transport aperture: Based on empirical relations and the cubic law, see Appendix F, it is suggested that the transport aperture, e_T, can be estimated as:

  $$e_T = 2.0T^{0.6} \qquad \text{(4-13)}$$

- Fracture size-thickness: Field data from Äspö HRL indicate that a fracture thickness, b, of 1% of the fracture length is a good choice. The fracture thickness is defined to include the flow channel, the gauge material, parallel flow paths, etc. It is hence often one or two orders of magnitude larger than the aperture. The kinematic porosity, θ, is calculated from e_T and b ($\theta = e_T/b$).
- Diffusion coefficients: Molecular diffusion in a conductive element should be proportional to the product of the transport porosity and the diffusivity value in the pore water (Neretnieks 1993). The proportionality constant is related to the properties of the pore space (constrictivity and tortuosity). Often we will simply assume that the diffusion coefficient for a conductive element is equal to the product of the kinematic porosity and the diffusion value in pure water.

Fracture orientation. Several projects have been carried out with the objective to characterize the fracture orientation at Äspö. In DarcyTools fracture sets of different orientations can be generated and the spread around these orientations is governed by a Fisher distribution (see Appendix D).

Fracture intensity. The fracture intensity is specified from a power law distribution. For a length interval, *dl*, we then get:

$$n = \mathrm{I} * \left[\left(\frac{l+dl}{l_{ref}} \right)^a - \left(\frac{l}{l_{ref}} \right)^a \right] / a \qquad \text{(4-14)}$$

where n is the number of fractures per unit volume, I the intensity, l_{ref} a reference length (= 500 m) and a, the power law exponent, put to –2.6 (see La Pointe et al. 1999). At Äspö the intensity was determined to 10^{-8} by generating fractures in the interval 320 to 1,000 m and compare the number with the number of deterministic deformation zones in the Laboratory domain. The intensity chosen gives 10 to 15 (different realisations) deformation zones in the length interval which can be compared to 12 deterministic deformation zones. The parameters can of course be set by the user, see Report 3.

Fracture shape: The fractures are assumed to be squares, with length, *L,* and have a thickness, *b*. DarcyTools can apply a varying thickness, and hence properties, for a limited number of major deformation zones. A correlation structure can be specified for each of these zones by a method described in Appendix C.

4.4 FRAME

We will now return to the subgrid model FRAME described in Chapter 3. The influence from the immobile zones on the mobile concentration of a tracer is given by the source/sink term Q_c in Equation 4-2. Before Q_c can be specified some further developments of the ideas introduced in Chapter 3 are needed.

The starting point is the representation of the immobile water in storage volumes, as outlined in Figure 4-1. To simulate the mass transfer within a storage volume one needs to solve a 1D diffusion equation. However, as has been shown by Haggerty and Gorelick (1995), it is possible to simulate the transport within the storage volume by a series of boxes that exchange matter with the kinematic volume; see Figure 4-1. Using this approach the term Q_c (in Equation 4-2) and the equations for the boxes will take the following form:

$$Q_c = -\sum_{j=1}^{N} \beta_j \frac{\partial (C_{im})_j}{\partial t} \tag{4-15}$$

$$\frac{\partial (C_{im})_j}{\partial t} = \alpha_j \left(C - (C_{im})_j \right) , \quad j = 1,2,..N \tag{4-16}$$

where β_j represents the capacity ratios, α_j the first order mass transfer coefficient and $(C_{im})_j$, the tracer concentration in the immobile water represented by box j. The total capacity $\beta_t \left(= \sum_{j=1}^{N} \beta_j \right)$ is equal to the volume ratio between the immobile and mobile zones (for a non sorbing tracer). For "layered diffusion", which is the situation when a storage volume is in contact with a kinematic volume, Haggerty and Gorelick (1995) give the following expressions:

$$\alpha_j = \frac{(2j-1)^2 \pi^2}{4} \frac{D_a}{a^2} \tag{4-17}$$

$$\beta_j = \frac{8}{(2j-1)^2 \pi^2} \beta_t \tag{4-18}$$

where D_a is the apparent pore diffusion coefficient and a the linear dimension of the storage volume. For further details about this "multi-rate model of diffusion", see Haggerty and Gorelick (1995).

As discussed in Chapter 3, FRAME is based on a power-law formulation. The main argument for this is that the fractal properties of the subgrid fracture network should be the same as for the resolved network. The use of a power-law formulation does however also support a further development of the model.

- As mentioned, all storage volumes are represented by a series of first order capacity boxes. When all storage volumes have been represented, the continuous distribution of capacities is also a power-law. This can be shown both numerically and analytically.
- It can further be shown that the slope of this distribution is related to the late time slope of the breakthrough curve, *k*.

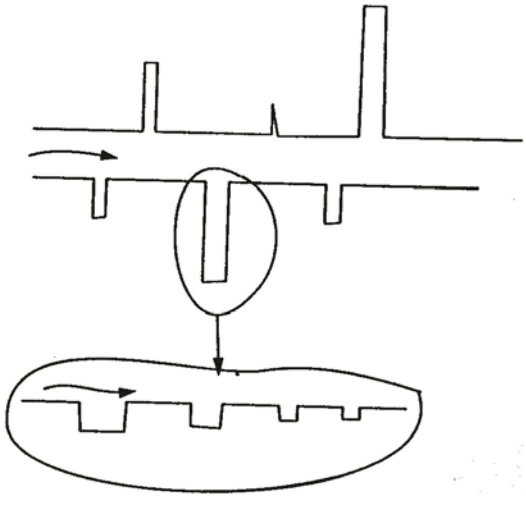

Figure 4-1. *Illustration of how a storage volume is simulated as a series of first order boxes.*

- In Chapter 3 the properties of the storage volumes were stated to be a function of three parameters: a, γ and Ψ. It can be shown, see Appendix B, that these are related to k as follows:

$$k = \frac{a - \gamma - 2\Psi + 1}{2 - \Psi} \tag{4-19}$$

These developments form the basis for the implementation of FRAME.

We will now return to the source term Q_c (Equation 4-15) and see how FRAME is specified for an advection/diffusion equation like (4-2). Let us further assume that C is salinity in this equation. The parameters that specify the model are:

- β_i, the volume ratio between the immobile and mobile zones.
- α_{min} and α_{max}, the minimum and maximum mass transfer coefficients. Note that these specify the length interval of the storage volumes considered as $\alpha_{min} = D_{mol}/l^2_{\max}$ and $\alpha_{max} = D_{mol}/l^2_{\min}$, where D_{mol} is the molecular diffusion coefficient and $l_{\max}$ and $l_{\min}$ the maximum and minimum lengths of storage volumes.
- k, the late time slope of the break-through curve. k determines how β_t is distributed over the spectrum of mass transfer coefficients.

In the numerical implementation a few more parameters need to be considered:

- n_α, the number of α-intervals that the total spectrum should be divided into.
- The FWS is also needed to consider in applications were a cell to cell variation of FWS is taken into account. The method employed is to calculate a β_t that varies from cell to cell. This is done by using FWS/vol_m (where vol_m is the volume of the mobile zone) as a weighting factor and then ensure that the global mean of β_t has the prescribed value.

Thus:

$$\beta_{t,cell} = \overline{\beta}_{t,cell} \left(\frac{FWS}{vol_m} \right)_{cell} / \overline{\left(\frac{FWS}{vol_m} \right)_{cell}} \tag{4-20}$$

where overbars indicate a global average.

4.5 PARTRACK

The particle tracking routine in DarcyTools is called PARTRACK.

PARTRACK has two basic modes of operation; the first is the traditional way of moving the particle along the local velocity vector, while the second method uses the so called "cell-jump" approach. The first method is based on an interpolation of the velocity components (defined at cell walls) to obtain the local velocity vector within the cells. The second approach is believed to be more appropriate for transport in a fractured media and is therefore described in some more detail:

- A particle entering a scalar cell will, if no dispersion effects are activated, stay in the cell for a time which is equal to the free volume of the cell divided by the flow rate through the cell (a so called plug-flow). If dispersion effects are active the travel time will however be different and will also be different for different particles.
- When the particle is ready to leave the cell, it will leave through one of the cell walls that have an outgoing flow direction. The choice between cell walls with an outgoing flow is made with a likelihood that is proportional to the outflows. If several particles are traced, the cloud will thus split up in proportion to the flow rates. Complete mixing in a cell is hence assumed.

It should be noted that no time is spent when moving from one cell to the neighbour. Next we will discuss some details about the two points above.

When the particles are travelling through the cell, the retardation due to matrix diffusion, sorption and Taylor dispersion need to be accounted for. The concept of particle states is used to simulate these processes. As an illustration let's outline how Taylor dispersion can be simulated. If the velocity profile is described as a number of layers, each with a certain velocity, we identify these layers as the different states a particle can be in. If correct frequencies can be ascribed for moving to a neighbouring layer, it is realized that particles will experience different velocities when staying in the cell and a Taylor dispersion effect will result. If we further should like to account for sorption on the fracture walls a particle state is also needed for this process. We also need to find out the frequency by which a particle will leave the velocity layer close to the wall and enter the "sorbed state" and also the frequency by which it will go back.

If Taylor dispersion is simulated by PARTRACK a "cross diffusion coefficient", *fxdift*, needs to be specified. A parabolic velocity profile is assumed and *fxdift* is then equal to the diffusion coefficient divided by the square of the aperture.

PARTRACK uses FRAME to account for matrix diffusion and sorbtion processes. The parameters introduced for FRAME applies also to PARTRACK. However, as PARTRACK can also handle sorbing tracers we need to introduce the retardation factors for the mobile, R_m, and immobile zone, R_{im}. These will affect the FRAME parameters as follows:

- $\beta_t = \beta_n \frac{R_{im}}{R_m}$, where β_n is the volume ratio for a non-sorbing tracer.
- $\alpha_{\mathrm{min}} = D_{mol}/(l^2_{\mathrm{max}} R_{im})$
- $\alpha_{\mathrm{max}} = D_{mol}/(l^2_{\mathrm{min}} R_{im})$

Presently the best source of information regarding sorbing tracers is the SKB report IPR-06-21. For a discussion of how retardation are included in the multi rate model, see Haggerty and Gorelick (1995).

4.6 Finite volume equations and solver

CFD (Computational Fluid Dynamics) methods transform the differential equations into algebraic ones, which can be solved numerically. DarcyTools uses the so-called finite volume method, which can be thought of as having three well-defined stages:

1) Discretize the computational domain into a number of cells, which fill entirely the domain.
2) Integrate each differential equation for each cell, to yield an algebraic equation.
3) Solve the resulting set of algebraic equations.

The differential equations were given in the previous sections. After the integration, step 2 above, an algebraic equation of the following type results:

$$a_P\Phi_P = a_W\Phi_W + a_E\Phi_E + a_S\Phi_S + a_\mathrm{N}\Phi_\mathrm{N} + a_\mathrm{B}\Phi_\mathrm{B} + a_\mathrm{T}\Phi_\mathrm{T} + S_\phi \tag{4-21}$$

where Φ denotes the variable in question, a coefficients and S_ϕ source terms. For further details, see Appendix A.

It is equations of type (4-21) that are solved by the solver MIGAL (see Appendix A); in fact MIGAL can solve linked systems of this kind of equations, a feature that is used for the pressure-salinity coupling in the present set of equations.

From version 3.4 DarcyTools can take full advantage of computers with multi-core processors. This parallelization option is briefly described in Appendix H.

5 Confidence building

5.1 Some definitions

During the last twenty years CFD (Computational Fluid Dynamics) has become a standard simulation tool in most engineering problems, dealing with groundwater flow and transport. This development has been driven by readily available software packages and the significant increase in affordable computer speed and memory capacity. CFD is however not a simple technique to use; generally speaking a basic understanding of several subjects like fluid mechanics, numerical analysis and computer software programming is required. For groundwater modelling an understanding of hydrogeology is of course also needed. In a recent project, ERCOFTAC (Casey and Wintergerste 2000), guidelines for CFD simulations are discussed and summarized. Partly based on this report, the following main sources of errors and uncertainties in groundwater simulations can be identified:

- **Mathematical model.** The mathematical model does not describe the real flow exactly. For example, in textbooks the approximations inherent in the Darcy equation are often analyzed and listed. Another often used approximation is that the water is incompressible.
- **Discretization.** Numerical solutions are performed on a grid in space and time. The difference between the solution on this grid and the exact solution of the modelled equations is called the discretization error.
- **Convergence and round-off errors.** Typically a CFD simulation involves iterative procedures. Convergence errors occur because these iterations are stopped by a certain criteria before they are completed. Round-off errors are due to the limited number of digits when a number is stored in the computer memory.
- **Application uncertainties.** This includes uncertainties about the geometry of the domain (for example a fracture network), boundary conditions, fluid properties, etc.
- **Code errors.** It is difficult to get software "bug-free".
- **User errors.** These are the errors that result from mistakes or carelessness by the user.

More points could have been listed (errors in postprocessing, interpretation of results, etc) but the list given probably gives the most important ones. In this context it may be of interest to refer to the following definitions (from ERCOFTAC):

Error:	A recognizable deficiency that is not due to lack of knowledge.
Uncertainty:	A potential deficiency that is due to lack of knowledge.

As the present report will deal with flow and transport in a fractured rock, one should view the points given from this perspective. The significance of the different points may still vary depending on the modelling approach chosen and the problem studied. Here we mainly concern ourselves with a fracture network, as represented in a continuum model. All of the above discussed errors and uncertainties may still be relevant to consider and it is not easy, in the author's view, to neglect (or set priority to) any of the points. For the modelling approach chosen it is however expected that the "quality" of a simulation is strongly dependent on how well the fracture network is represented in the continuum model. The fracture network is however only partly known (geometry, properties, etc) and we therefore need to consider the uncertainty introduced.

The question whether a computer code is credible or not and methods to answer this question are given in an issue of the AIAA Journal (1998). Based on the papers presented, Table 5-1 has been created. The table is an attempt to illustrate the actions involved in the confidence building process. A few comments to the table.

- The order (from top to bottom) is essential. It is not possible to achieve certification without having demonstrated verification and validation.
- There is a consensus in the literature about the definitions of verification and validation. Additional steps and actions in the confidence building are still open to discussion.
- Some authors emphasize that it is important to distinguish between confidence building in a computer code and in a specific application. Related to this issue is the concept "fitness for purpose". It is for example of little value to have a very accurate numerical solution if the algorithm is so slow that the code is impractical for its intended use.

Table 5-1. Processes and actions involved in confidence building.

	Process	Definition	Action
CONFIDENCE BUILDING ↓	Verification.	Demonstrate that the equations are solved correctly.	Comparison with analytical solutions and other models.
	Validation.	Demonstrate that the right equations are solved.	Comparison with measurements (laboratory and field data).
	Certification.	Assess whether the right things are done and whether they are done right.	Evaluate software construction and working procedures.
	More (QA-systems, wide range of applications, publications in international journals, etc).		

5.2 Verification of DarcyTools

The verification cases performed can be found in Report 2 and are summarized in Table 5-2.

All cases tested show “good result”, i.e. the comparison with the corresponding analytical solution, or another model study, is satisfactory; the reader is referred to the report to study the details.

A few words may however be needed to explain the objectives when selecting the test cases and the way the comparisons have been carried out.

- The test cases should include one, two and three dimensional, steady and transient cases.
- A wide range of relevant physical processes should be included, i.e. density stratification, unsaturated zones, storativity effects, etc.
- The representation of fractures in a continuum model is a key feature of DarcyTools and should be well covered by the test cases.

Some verification studies described in the literature are focused on grid refinement studies. Here the listed objectives have however been considered to be more important with the “fitness for purpose” argument in mind.

Table 5-2. Compilation of verification cases.

Group	Case	Comment
A. Numerical methods	A1. One dimensional transient diffusion A2. One dimensional steady advection/diffusion A3. Two-dimensional pressure problem A4. Test of grid, fractures as objects A5. Test of grid, cell removal	This group of cases intends to show that the numerical methods work as expected.
B. Porous media	B1. Regional groundwater circulation B2. Steady groundwater table B3. Theis problem B4. Water inflow to a circular tunnel B5. Specific yield B6. Transient groundwater table B7. Water inflow to a grouted tunnel.	This group considers some classical hydrogeological test cases.

Group	Case	Comment
C. Fractured media	C1. Three fractures in a two dimensional domain C2. A multi-fracture fracture zone C3. Single fracture in a box C4. Many fractures in a box C5. Percolation theory C6. Diffusion in a dead-end fracture C7. Matrix-fracture temperature problem	This group of cases deals with the representation of fractures in a continuum model.
D. Transport and dispersion	D1. Taylor dispersion D2. Breakthrough curve, PARTRACK D3. Breakthrough curve, adv/diff equation D4. Seven fractures in a 2D domain, PARTRACK D5. Three fractures in a 2D domain, PARTRACK D6. Single fracture in a box, PARTRACK	This group considers transport, retention, dispersion and particle tracking cases.
E. Buoyancy effects	E1. Henry's problem E2. Two fluid problem E3. Coupled temperature- salinity fields E4. Upconing E5. The floating island	This group considers comparisons where density stratification, due to salinity and temperature gradients, is a key factor.

5.3 Validation of DarcyTools

As validation should be concerned with comparisons to measurements and DarcyTools has not yet been widely used for real world applications, it is not surprising that rather few such comparisons can be reported at this stage. However, as discussed in Chapter 1, it is relevant to include cases that were carried out with PHOENICS as the equation solver, as it has been carefully evaluated that the two solvers give very similar solutions. Note that the descriptions of the fracture network (GEHYCO) and other descriptions of physical processes are in most respects the same in the PHOENICS cases to be discussed, as in the present version of DarcyTools.

For simulations of flow and transport in a fractured rock, it is difficult to separate the steps "validation" and "calibration". To discuss this we first need to define "calibration" (following AIAA Journal 1998):

- **Calibration** is the process of tuning a code, in order to improve its prediction of global quantities, for realistic geometries, of design interest.

If we require that validation studies should be concerned with comparisons with field measurements, we also need to accept that these measurements are obtained in conditions that are to a large extent unknown. We do not know the fracture network (its geometry, fracture properties, boundary conditions, etc). In the author's view, we therefore have to accept the following tentative definition of validation:

- For the flow and transport in a fractured rock, **validation** of a simulation can be claimed if calibration can be performed with all adjustable parameters within realistic limits.

This definition immediately raises the question "what are realistic limits?". For major fracture zones we may be able to define bounds for properties (thickness, transmissivity, porosity, etc) and these bounds then define the "realistic limits". However, for most applications properties and boundary conditions can not be given with error bounds and we have to accept the admittedly weak definition given. Flow and transport around a repository introduce a number of special considerations (for a discussion, see Cliffe et al. 1998). As one example we may mention the analysis of the impact of an inland ice on the performance of a repository. It is not possible to validate a model, by comparisons with field data, for such a case; still predictions are needed.

Validation cases are described in Report 2 and summarized in Table 5-3. As can be seen the validation cases are taken from calibration studies in various projects. We thus follow the definition of validation given above.

Table 5-3. Compilation of validation cases.

Case	Project (Reference)	Comments
A site scale validation (Case V1)	Impact of the tunnel construction on the groundwater system at Äspö. Task 5 (Svensson et al. 2002).	Calibration focuses on: – Groundwater table – Pressure in boreholes – Kinematic porosity – Water composition Code: PHOENICS
A laboratory scale validation (Case V2)	A laboratory scale analysis of groundwater flow and salinity distribution in the Äspö area (Svensson 1999b).	Calibration focuses on: – Fracture transmissivities – Pressure in boreholes – Conductivity distributions Code: PHOENICS
A repository scale validation (Case V3)	Prototype repository. Groundwater flow, pressure and salinity distributions around the Prototype repository. Continuum model No1 (Svensson 2001d).	Calibration focuses on: – Tunnel inflows (skin) – Pressure in boreholes – Conductivity distributions Code: DarcyTools
An experimental scale validation (Case V4)	Simulation of tracer transport considering both experimental and natural time scales (Svensson and Follin 2004).	Calibration focuses on – PARTRACK – Sorbing and non-sorbing tracer retention. Code: DarcyTools
A pump test (Case V5)	The Olkiluoto site, Finland. - Numerical simulations of the pump tests in boreholes KR14-KR18 Äspö Task Force; Task7B (Svensson 2010b).	Calibration focuses on • Pump tests • Representation of boreholes in a large scale model. Code: DarcyTools

5.4 Concluding remarks

It is clear from this chapter that the process of confidence building is complex and involves many aspects. The bottom line is if a particular simulation is credible or not. The computer code, and its verification and validation, is of course a key factor when credibility is judged, but the user of the code is also important. CFD simulations are still far from routine calculations and the modeller normally makes a number of decisions when formulating the problem conceptually and mathematically. The "credibility of the modeller" is hence also a factor to consider.

6 A generic Äspö model

6.1 Introduction

In the chapter on Confidence Building it was noted that DarcyTools has not been extensively used in real world applications. The application to be discussed in this section has similarities with the conditions at Äspö HRL, but is generic in nature; it will hence not add to the validation studies reported. Instead the objective is to show some of the features and capabilities of DarcyTools in a realistic, but generic, application. The reason for keeping the case generic is that the description of input data and results can be brief, as we can not discuss these in relation to field data.

The situation studied is outlined in Figure 6-1. It is a coastal site, with sea water of a brackish nature (salinity of 1%). We assume a certain precipitation on land and we hence have a density stratification to take into account. Two hills give a certain topography on land. A tunnel, with a certain inflow, will be placed below the small island in the experimental volume shown in the figure. The focus of the analysis will be on the effects of the tunnel. The situation has a clear resemblance with the Äspö region. The fracture system will however be much simpler in this demo, as compared to the detailed information available for Äspö HRL. Four major fracture zones, shown in Figure 6-1, are assumed to represent the deterministic system. Random fractures will be generated to build a working fracture network.

It should be mentioned that the set-up in DarcyTools will be used as a work example in the User's Guide (Report 3).

6.2 Problem specification

A summary of the problem specification is given in Table 6-1. It is not the intention to give a complete account of the input data; this is considered to be outside the scope (the specification of the fracture network would be lengthy, for example). A few comments may be needed as a complement to the key features in the table (see also Figure 6-1):

- Domains. The site model covers the whole domain, while the laboratory model is located below the island. The first of these two grids follows the topography, while the second grid is a cartesian box. The experimental model is placed in the laboratory model, enclosing the tunnel area.
- Properties. Porosity is specified for each fracture and fracture zone. The diffusion coefficient is given a value of ten times the value for molecular diffusion for salt; diffusion is hence insignificant. Transmissivities, orientations, etc for the random fractures are set according to the values found appropriate for Äspö HRL.
- Random fractures. When the fracture network for the site domain is generated, random fracture in the interval 40 → 1,000 m are generated. Random fractures in the interval 10–40 m are then added for the laboratory volume. For the experimental volume random fractures in the interval 2–10 m are added.

6.3 Results

Some sample results will be presented for the situation with the tunnel present.

In Figure 6-2 a vertical section showing the salinity field can be found. The salinity fields show the typical fresh water lenses below land and the island. The upconing of salt water below the tunnel is also worth noting.

Next we study the conditions around the tunnel, see Figures 6-3 and 6-4. The salinity and pressure fields on the surface of the enclosing experimental volume are shown.

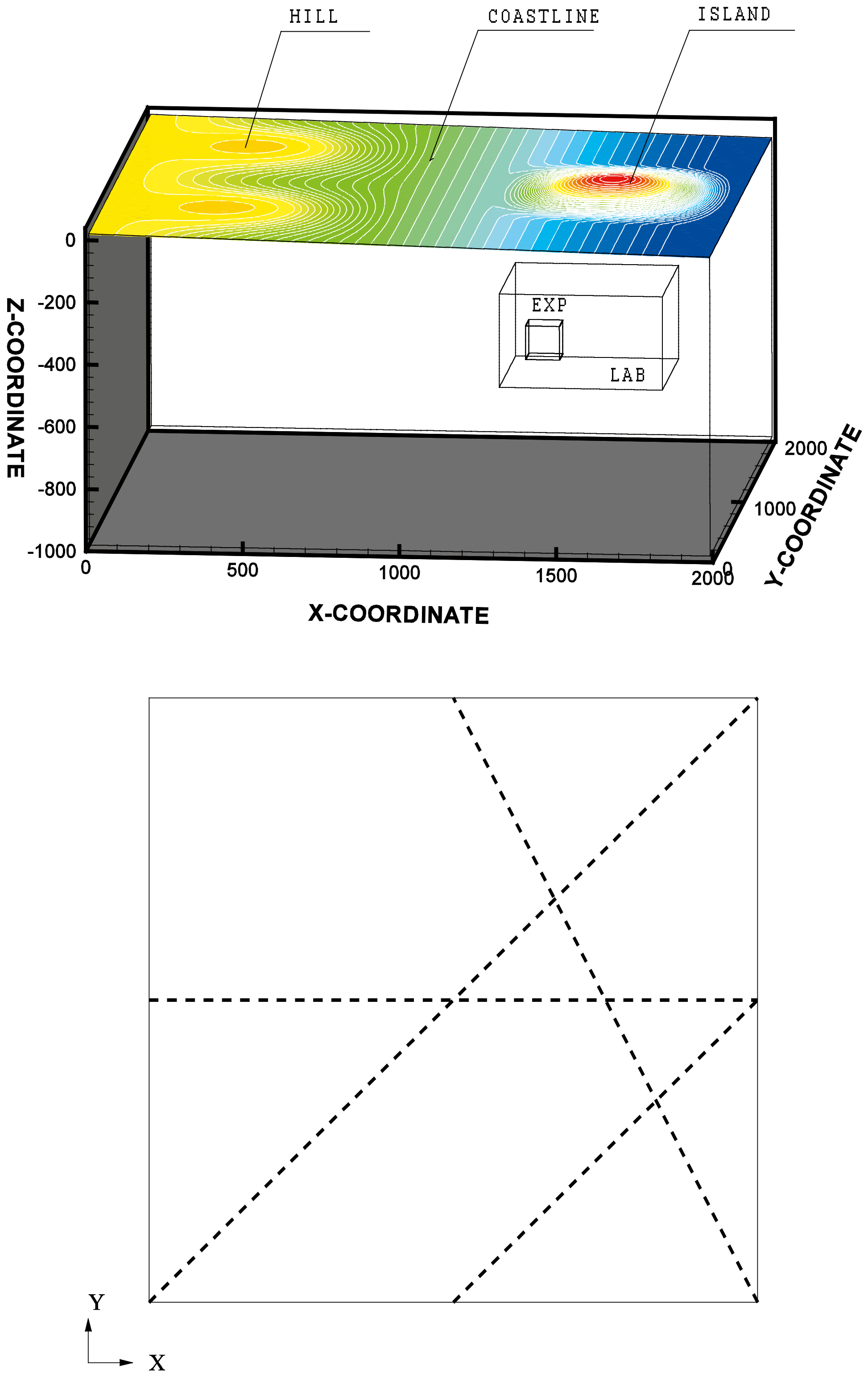

Figure 6-1. *Situation considered (top) and deterministic fracture zones*

Table 6-1. Summary of problem specification.

Domains and grids	Site: 2 × 2 × 1 km^3 Δ =32 m Laboratory: 500 × 500 × 400 m^3 Δ = 16 m Experimental: 200 × 100 × 100 m^3 Δ = 8 m Tunnel: Δ = 2 m
Properties	– Deterministic zones according to Figure 6-1, Transmissivity = 10^{-5} m^2/s – Random fractures Site: *l* = 40 → 1,000 m Laboratory: *l* = 00 → 40 m Experimental: *l* = 2 → 10 m – Diffusion coefficients: 10^{-8} m^2/s, constant
Boundary conditions	Top: Precipitation on land , 50 mm/year Pressure and salinity fixed below sea Vertical boundaries: Zero flux at x = 0 boundary. Prescribed pressure and salinity on other vertical boundaries. Fixed salinity at bottom boundary. Tunnel : Grouting with a maximum conductivity of 10^{-8} m/s. Groundwater table: As part of the simulation the groundwater table is calculated.

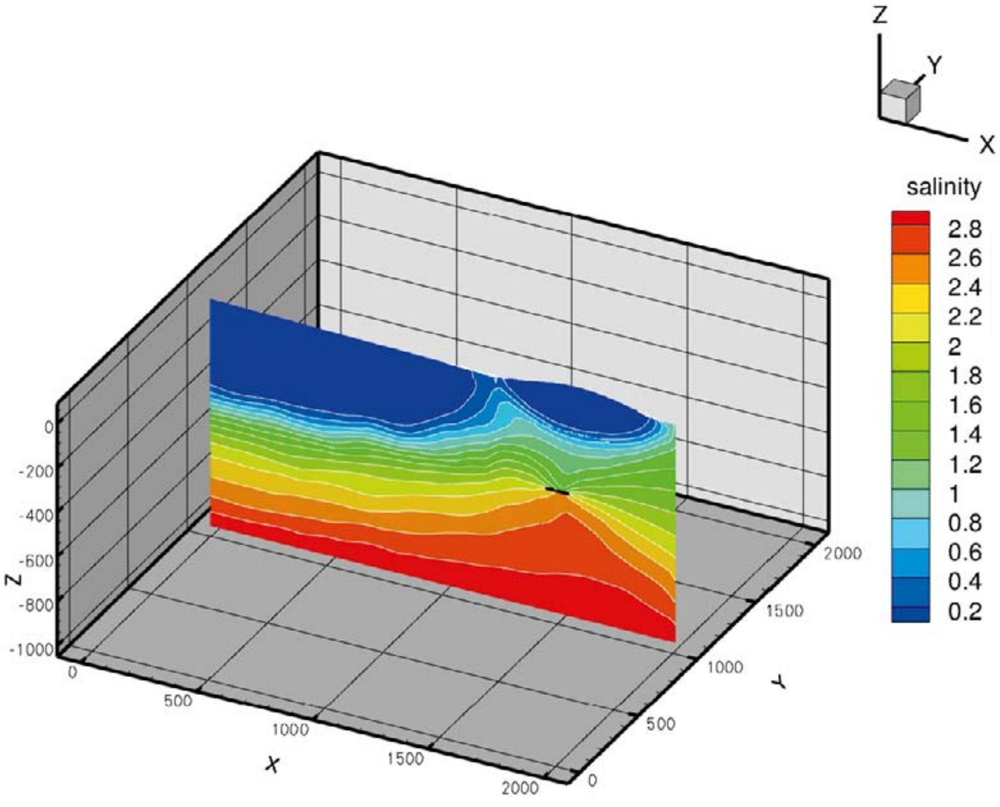

Figure 6-2. Vertical section through the island. Salinity field (in %) with upconing due to the tunnel. Blue colour indicates fresh water.

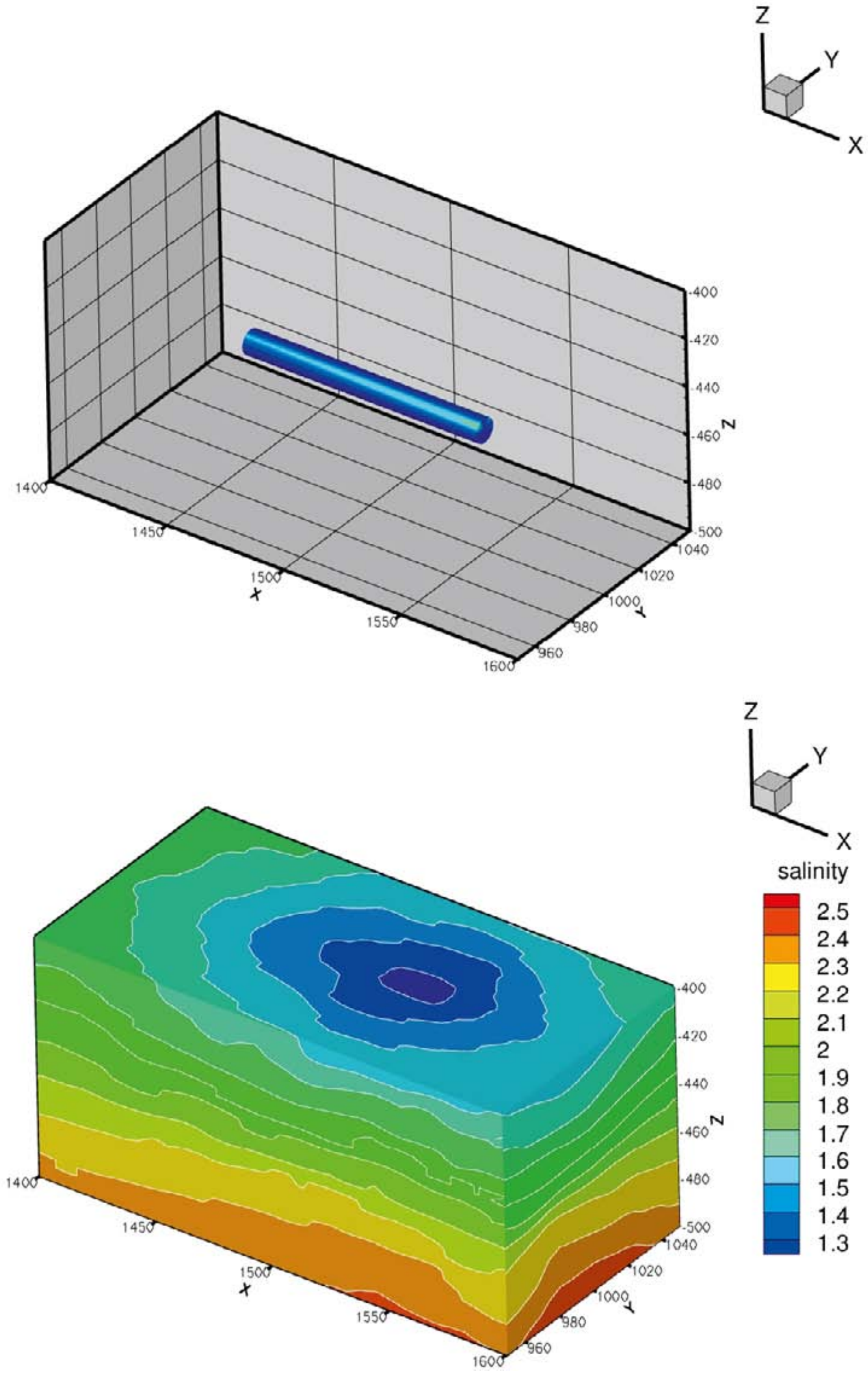

Figure 6-3. *Salinity field (in %) around the tunnel.*

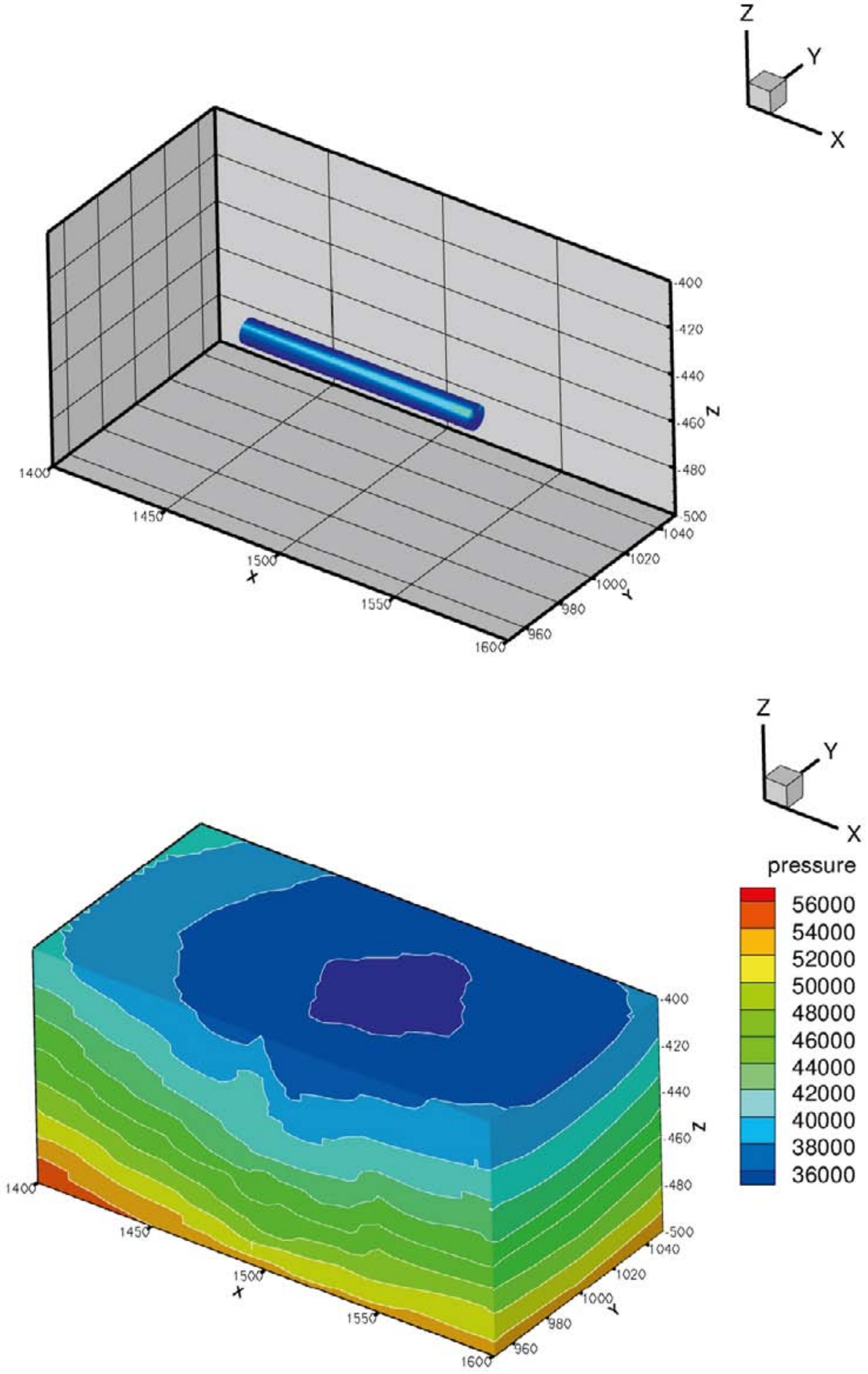

Figure 6-4. *Pressure field (Pa) around the tunnel.*

6.4 Concluding remarks

It has been shown that some features of the Äspö site, like fresh water lenses and upconing, can be simulated in a simple generic set-up.

7 Illustration of some key concepts

7.1 Introduction

Several development projects preceded the present report on DarcyTools. A number of fundamental issues dealing both with flow and transport in fractured rocks and numerical modelling techniques were addressed. It is not possible to include these studies in the present report, but a brief review of some key results is within scope. The reason for reviewing these related studies is that they illustrate the concepts used and highlight some aspects of DarcyTools that are believed to be essential for a groundwater code.

The laboratory model of Äspö HRL, see Chapter 1, will be used for the simulations as we are going to illustrate features that are believed to be important in real world applications.

7.2 Spatial and temporal discretization errors

In this section results that show the magnitude of the discretization errors, that can be expected in a real world application, will be presented. As we are interested in general trends and results, the estimated magnitudes will be based on the average of ten realizations of the background fracture network. This will also give a perspective on the discretization error, as it can be compared to the variations due to different realizations.

It was stated in Chapter 3, that the smallest generated fracture size should be of the same size as the grid cells, i.e. $l_{min} \approx \Delta$. In a grid independence study, it is however preferable to keep all parameters the same, except for the studied parameter Δ. For this reason l_{min} is equal to 3 m when flow rates are studied and 10 m in the transport simulations, motives for these values are given below.

Flow and Pressure

As a background to the grid independence study some general characteristics of the fracture network will be discussed. It was stated in Chapter 3, that an underlying assumption of the present method to represent a fracture network is that "large fractures are more important for the flow rate than small ones". In Table 7-1 some calculations of the mean block, or domain, conductivity in the West to East direction are shown. As can be seen the block conductivity does not change a lot if l_{min} is 5, 10 or 15 m. In the following l_{min} will be put to 3 m, which ought to ensure that all fractures important for the flow simulation are included. Table 7-1 also shows that the block conductivity changes more when Δ is changed; this aspect will be analyzed in detail below. Table 7-2 shows the block conductivity in different realizations for three of the values shown in Table 7-1. Different realizations can clearly result in rather different block conductivities. Block conductivities with only the major deterministic deformation zones present are shown in Table 7-3. There is no stochastic element in these simulations and there is hence no need for several realisations. Some grid dependence is found for the South to North direction, while the two other directions show very little sensitivity to variations in Δ. We may also note that, for the West to East direction, the block conductivity is 30–50% of the block conductivity shown in Table 7-1. The major deformation zones and the background fracture network thus have about the same significance for the flow rate.

The block conductivities in the West to East direction, as a function of Δ, are shown in Figure 7-1. Ten realizations of the background fracture network were generated to get the average values shown in the figures; l_{min} was equal to 3 m in all calculations. In the figure two graphs are shown. In the top one block conductivity is shown as a function of N_i, the number of cells in the coordinate direction studied. This curve shows that the block conductivity approaches a certain value in an asymptotic manner; this is the normal behaviour in grid refinement studies. The lower figure shows the same data, but expressed as a function of Δ. The advantage of this representation is that it is possible to extrapolate the curve to $\Delta = 0.0$, and hence get an estimate of the discretization error. At this stage we will only note that the error is around 10% (from extrapolation) for the solutions with $\Delta = 3$ m.

Table 7-1. Block conductivity for a pressure gradient in the West to East direction, for various $l_{\min}$ and Δ.

l_{min}	Conductivity x 10^{-7} (m/s) for various Δ (m).			
	5	10	15	20
5	0.66	0.84	1.00	1.17
10	0.66	0.81	0.97	1.14
15	0.66	0.81	0.97	1.13
20	0.61	0.76	0.93	1.07

Table 7-2. Block conductivity for a pressure gradient in the West to East direction. Ten realizations based on $l_{\min}$ = 5 metres and various Δ.

Realization	Conductivity x 10^{-7} (m/s) for various Δ (m).		
	5	10	20
1	0.76	0.94	1.20
2	0.66	0.83	1.06
3	0.63	0.79	1.04
4	0.57	0.74	1.01
5	0.65	0.78	1.03
6	0.59	0.83	1.18
7	0.56	0.75	1.02
8	0.59	1.06	1.08
9	0.87	0.92	1.36
10	0.71	0.77	1.21

Table 7-3. Block conductivity in the three coordinate directions with only major deterministic deformation zones present, for various Δ.

Direction	Conductivity x 10^{-7} (m/s) for various Δ (m).				
	3	5	10	15	20
West-East	0.30	0.31	0.31	0.32	0.33
South-North	0.80	0.85	0.98	1.10	1.22
Low-High	4.26	4.22	4.23	4.22	4.26

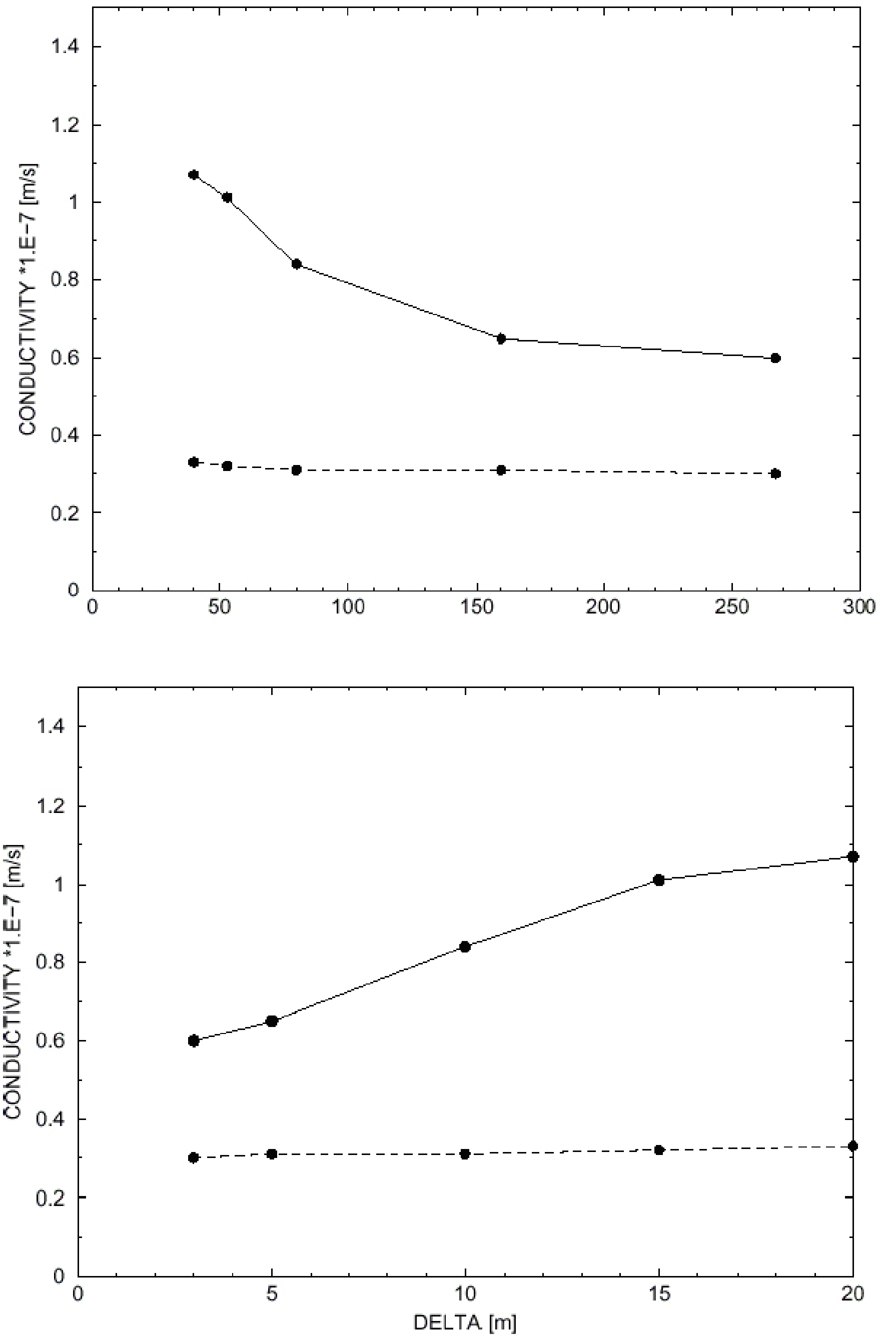

Figure 7-1. *Block conductivity in the West to East direction as a function of the number of cells in the coordinate direction (top) and as a function of Δ.*
(———) All fractures included.
(------) Only major fracture zones.

Some illustrations of what happens when Δ is varied are given in Figures 7-2, and 7-3. In the first figure, the flow and pressure distributions for a mean pressure gradient from West to East are shown. The general impression from these figures is that a Δ equal to 3 m resolves the major fracture zones (deterministic and stochastic) with high accuracy. For Δ = 10 m some of the details in the flow distribution are lost. One may also note that the pressure distributions are rather similar for Δ = 3 and 10 m. Figure 7-3 shows the conductivity fields for Δ = 3 and 10 m. The smaller Δ gives a fairly detailed picture of the fracture network.

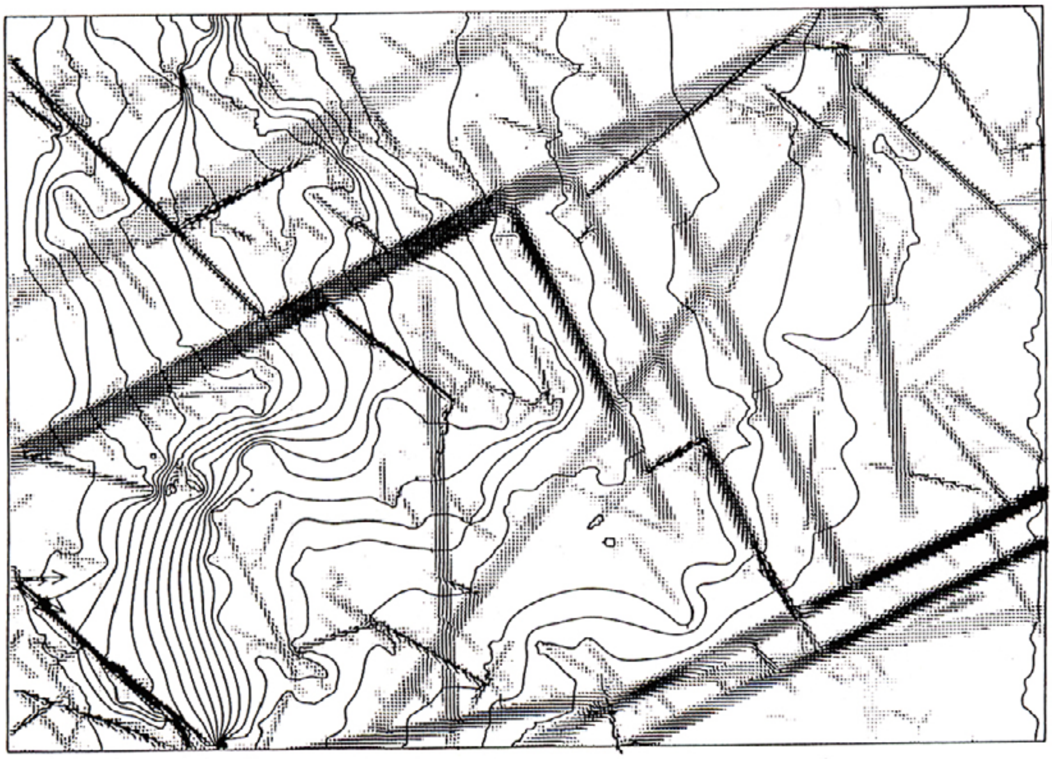

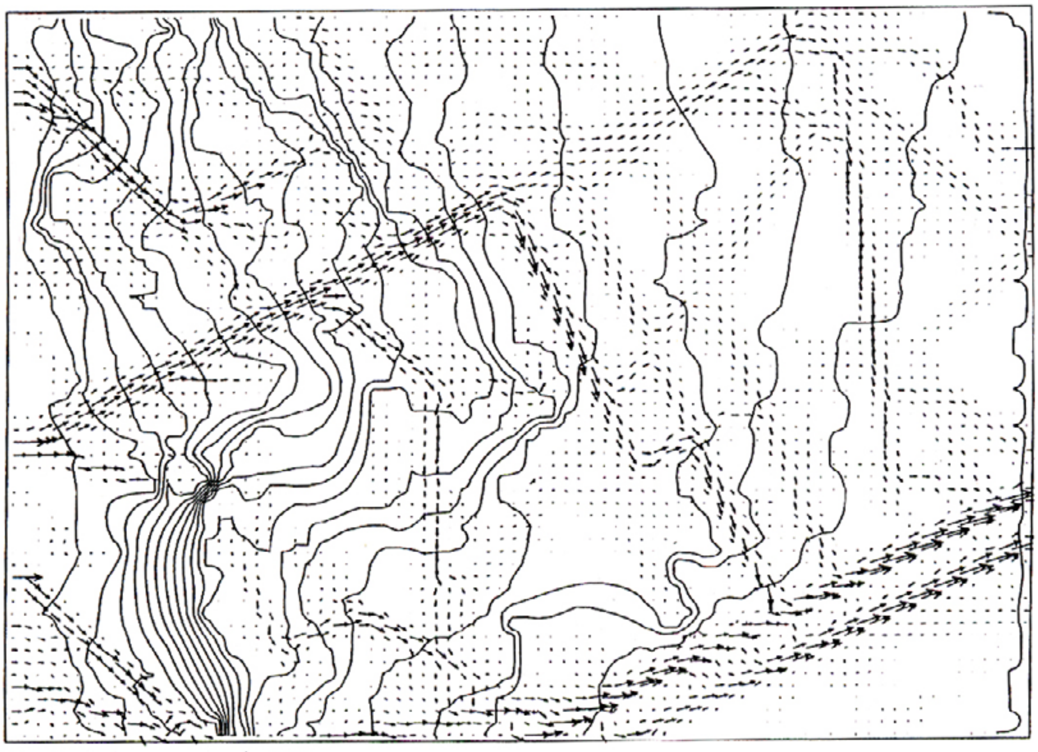

Figure 7-2. *Flow and pressure distribution for a mean pressure gradient from West to East. Pressure distribution shown with 20 isolines.* Δ = 3 *m (top) and 10 m.*

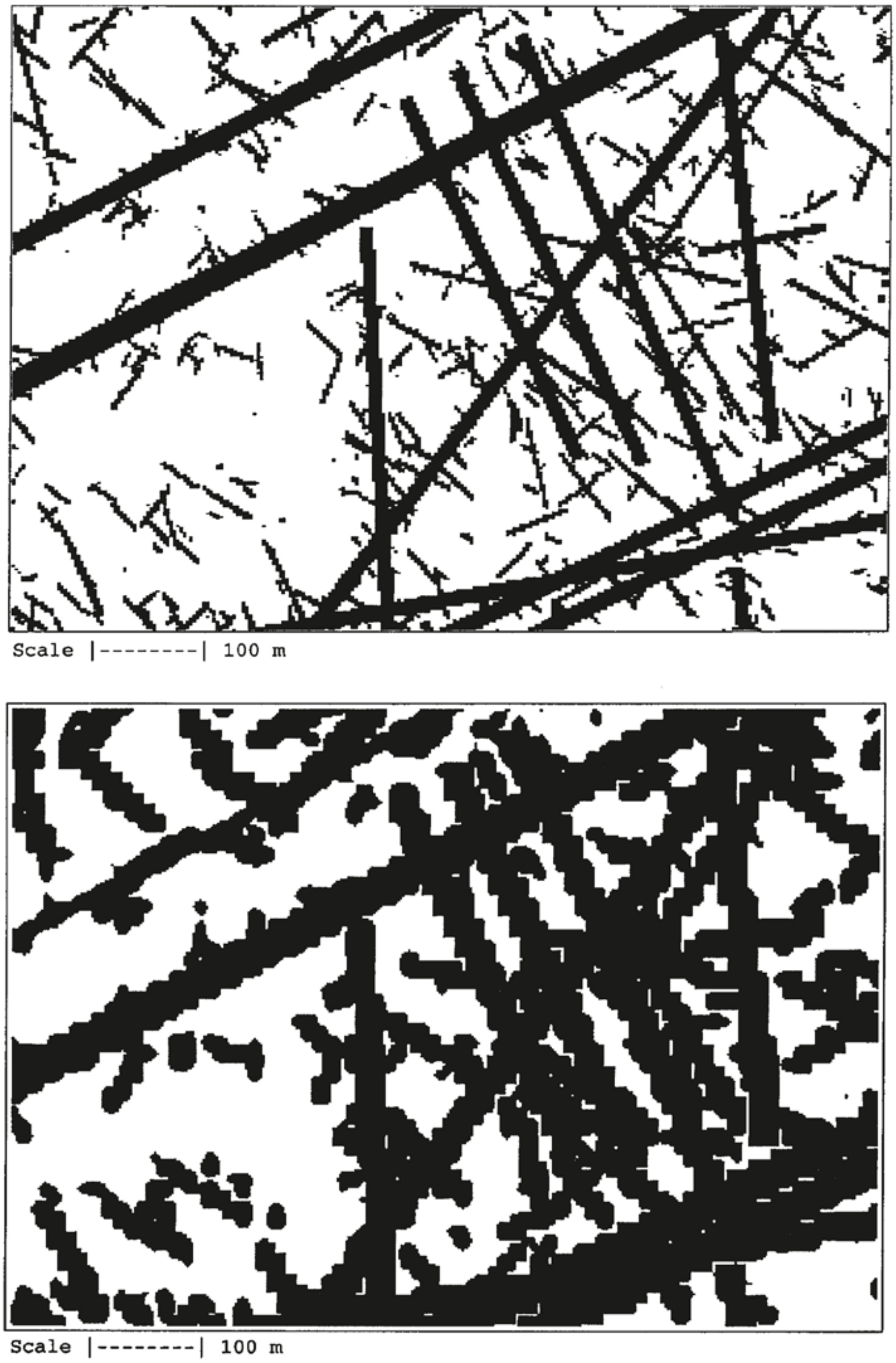

Figure 7-3. *Conductivity fields for* $\Delta = 3$ *m (top) and 10 m. All conductivities larger than* 10^{-8} *m/s shown.*

Transport and Dispersion

Estimating the discretization errors when simulating a tracer pulse that moves through the domain is more difficult than the steady state flow rate, as we then have to consider the errors both in space and time. In order to simplify the analysis only flow in the West to East direction will be considered. As the flow simulations further indicate that $\Delta > 10$ m produces quite "smeared" solutions, only $\Delta = 3{,}5$ and 10 m will be discussed.

The following situation is studied. In a steady flow field a tracer marks the water at the inlet (Western) boundary during a period of one year. After about fifteen years the pulse leaves through the Eastern boundary.

A typical breakthrough curve is shown in Figure 7-4. It is the concentration at the outlet, in fracture zone NE1, that is shown in the figure. The tracer will leave the domain through several fractures but the maximum flux is expected through NE1. Regarding l_{min} it was argued in Chapter 3 that a good choice is to put it equal to Δ. However in a grid refinement study it is preferable to keep the geometry fixed and only vary Δ. For this reason l_{min} will be put to the largest Δ, i.e. 10 m, in the following calculations.

In the grid refinement study, we will use the maximum concentration at the outlet as a simple description of the breakthrough curve. The main result of the exercise is given in Figure 7-5. The smallest time step used, 0.25 months, is seen to be close to the time step independent solution (from an extrapolation). It is also interesting to note that $\Delta = 3$ and 5 m give very similar results. Hence, with $\Delta = 3$ m and $\Delta t = 0.25$ months, we are probably close to a grid independent (in space and time) solution. The time step discussed are of course related to the mean transport time, and hence to the prescribed mean head gradient.

In Figure 7-6 the tracer distribution after ten years is shown for two Δ. As can be seen, the main characteristics of the plume are quite well described in both grids. The breakthrough curves for the smallest time steps used are given in Figure 7-7. Also this figure indicates that $\Delta = 3$ m resolves the transport problem with acceptable accuracy. The main difference between the three curves is the arrival time for the peak concentration. This difference is due to the increase in flow rate with Δ, as discussed above.

A concluding comment on the discretization errors in the transport simulations shown may be in place. The breakthrough curves in Figure 7-7 mainly differs in the arrival times, which can be explained by the increase in flow rate with Δ (as discussed above). The peak value and the shape of the breakthrough curves are however very similar. This is a strong indication that the grid representation of the flow and porosity fields is based on sound principles. The flow field looks quite different for $\Delta = 3$ and 10 m (see Figure 7-2) and the grid representation of the porosity fields is smeared in a similar way as the conductivity field (see Figure 7-3). Still the transport problem is solved in a similar way in both grids.

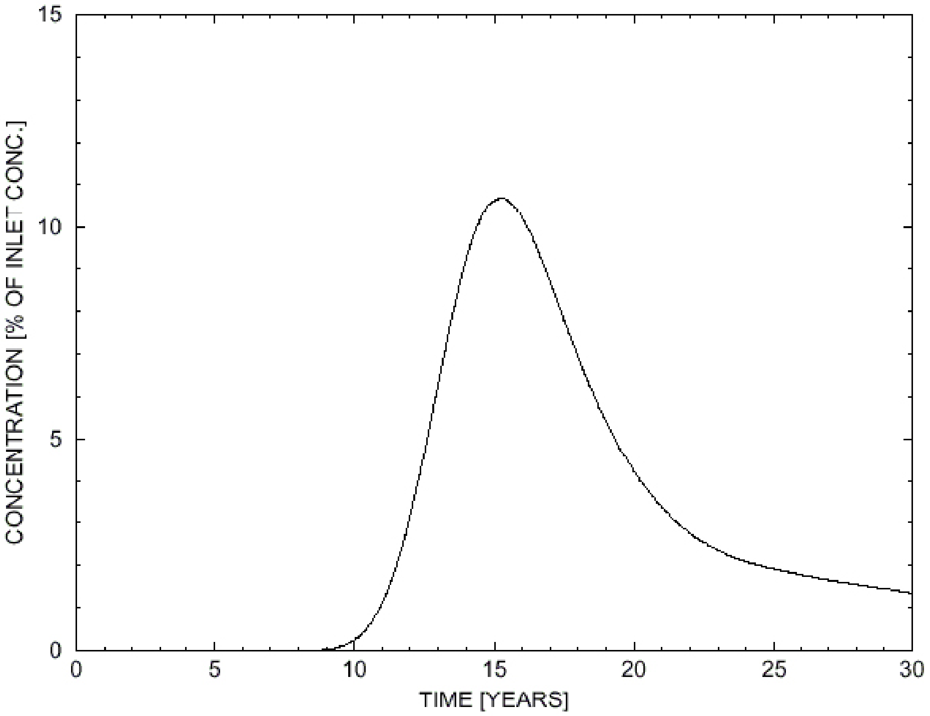

Figure 7-4. *Breakthrough pulse through NE1 at the outlet boundary.*
$\Delta = 5$ m, $\Delta t = 1$ month.

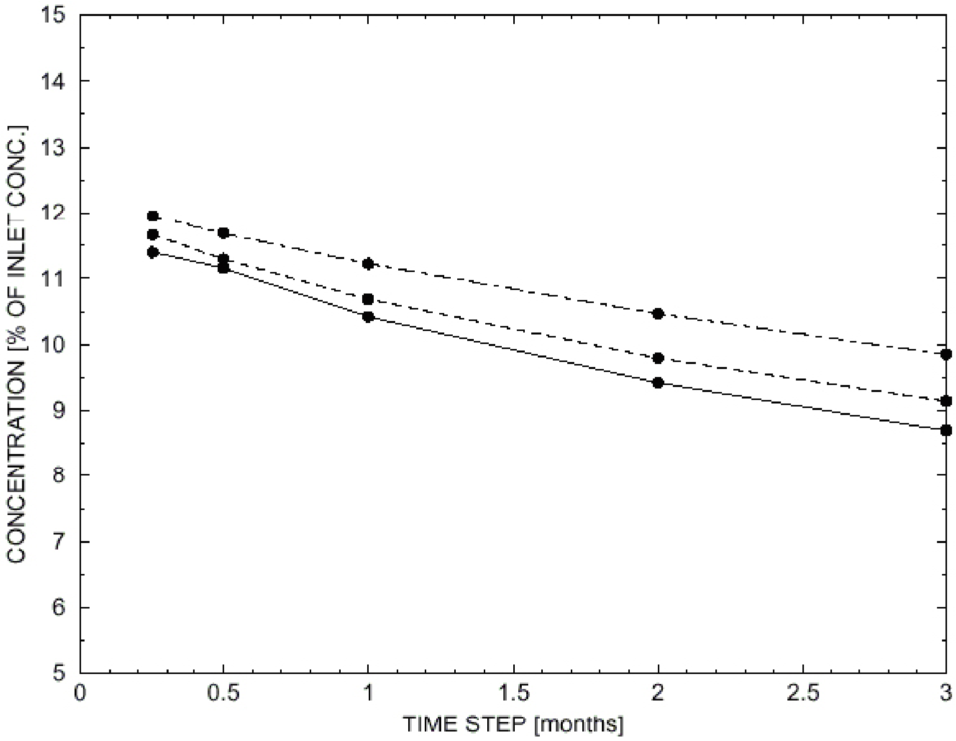

Figure 7-5. *Maximum concentration in fracture zone NE1 at the outlet plane, as resolved by different Δ and Δt.*
(——) Δ = 3 m.
(------) Δ = 5 m.
(-·-·-·-·) Δ = 10 m.

Conclusions

The objective of the work presented has been to estimate the discretization error, in space and time, in simulations of flow and transport in a realistic fracture network. This has been done for a test case with a prescribed mean pressure gradient in a coordinate direction. The block conductivity and transport characteristics for such situations have been studied for a range of grid cell sizes, Δ, and time steps, Δ*t*.

From the study the following main conclusions can be formulated:

- The space resolution, Δ, should be of the order of 1%, or smaller, of the domain size. For the test case studied the error, i.e. the difference between the actual and the estimated grid independent solution, in the block conductivity may then be around 10%.
- The estimated magnitude of the discretization errors is regarded to be small in comparison to the uncertainty in input data (for example transmissivities and porosities).
- The minimum fracture size in the background fracture network should be comparable to the grid size. This ensures that all important flow channels are resolved and provides a natural link to a subgrid model (the subgrid model considers the dispersion effect due to all fractures smaller than the grid size).

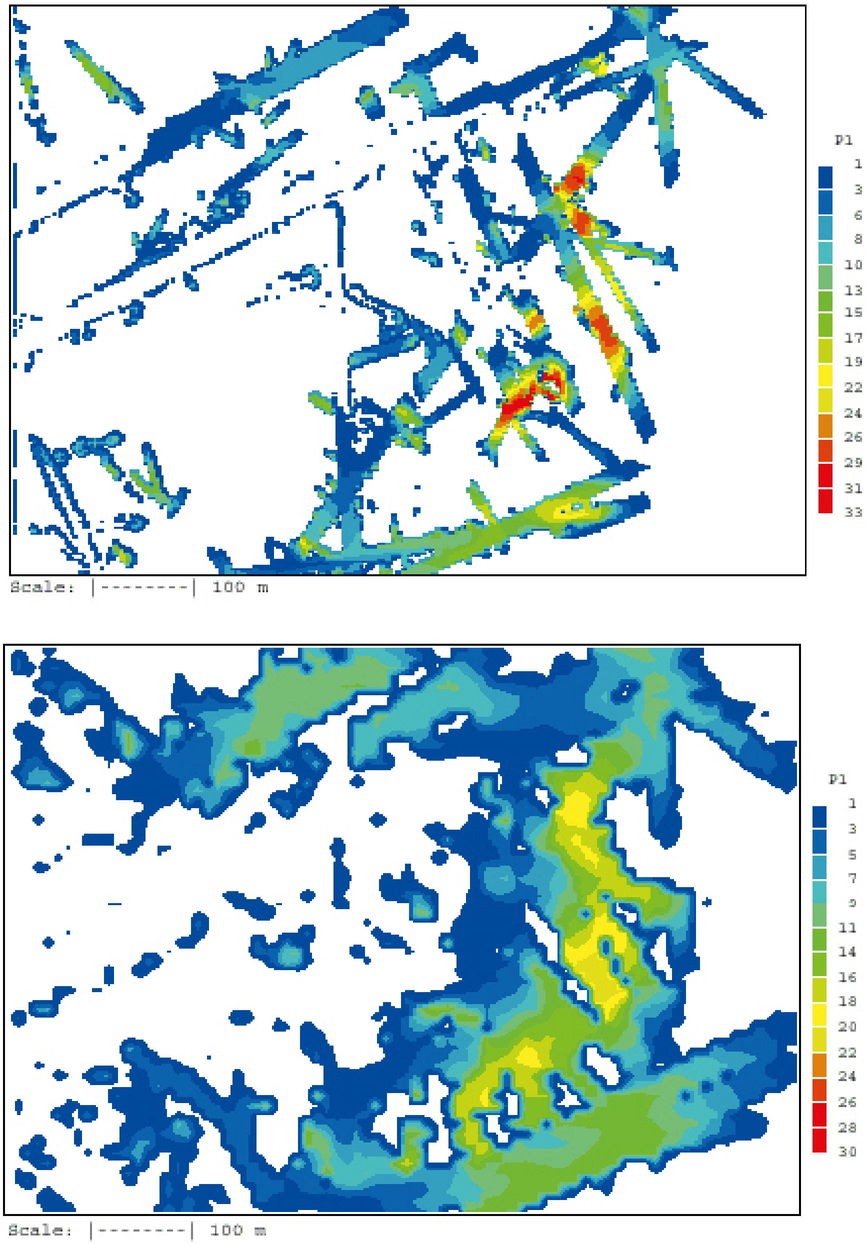

Figure 7-6. *Tracer distribution (in % of inlet concentration) after ten years. Δ = 3 m (top) and Δ = 10 m.*

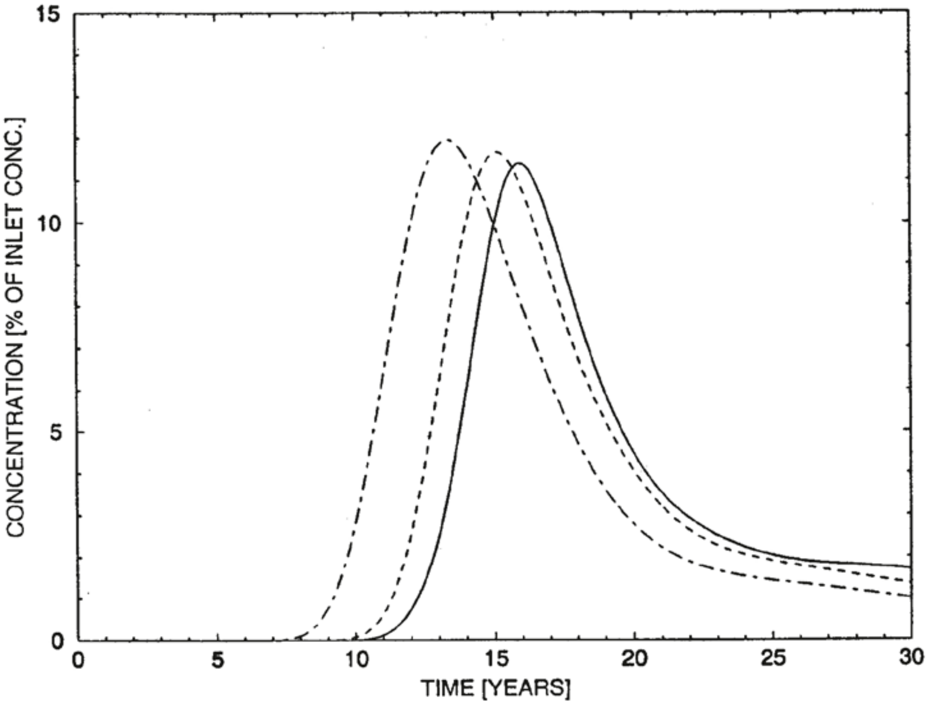

Figure 7-7. Breakthrough curves for $\Delta = 3$ *m (———), 5 m (------) and 10 m (-·-·-·-·). Δt = 0.25 months.*

7.3 Porosity and connectivity

In this section we will apply the porosity concepts to the laboratory model of the Äspö HRL.

In Section 3.6, some domain related porosity concepts were defined (θ_a, θ_c and θ_f). θ_f is the porosity based on "all volumes with a significant flow", i.e. stagnant parts have been removed from θ_c. As outlined in Section 3.8, some calculations are required to identify the stagnant volumes.

A typical sequence of calculations is shown in Table 7-4. For a head gradient of 10^{-3}, it is found that disregarding all cells with a maximum absolute cell wall flux of 3×10^{-11} m/s will result in a decrease of the average flux through the domain that is smaller than 1%. Note that the number of stagnant cells is not related to the flux value 3×10^{-11} m/s, as a different head gradient would result in another flux value; the 1% reduction limit will however still be valid.

Table 7-4. Determination of stagnant parts of the kinematic porosity field. The ratio Q/Q_m, where Q is the actual flow rate and Q_m the flow rate for θ_c, is determined for various limits on the absolute maximum flow rate through a cell wall, $|V_{limit}|$.

$\lvert V_{limit}\rvert$ [m/s]	Q/Qm [%]		
	East-West	**North-South**	**High-Low**
10^{-10}	93.7	96.9	99.0
5×10^{-11}	97.3	98.8	99.5
3×10^{-11}	99.0	99.5	99.7

Table 7-5. Kinematic porosity values based on total volume of domain and on volume of active cells.

Case	Porosity based on total volume	Number of active cells (%)	Porosity based on volume of active cells
All fractures included	1.19×10^{-4}	70	1.7×10^{-4}
Isolated fractures or clusters removed	1.13×10^{-4}	45	2.5×10^{-4}
Stagnant volumes and isolated fractures removed	1.09×10^{-4}	35	3.1×10^{-4}

In Figure 7-8 three porosity fields are shown; in the top one all generated fractures contribute to the porosity field, in the middle one all isolated volumes are disregarded and in the lower one also the stagnant volumes have been removed. It is clear that most of the flow is due to a limited number of fractures. Table 7-5 gives some further details. It is interesting to note that the porosity based on the total volume varies little between the cases listed. The explanation is that the isolated and stagnant parts of the porosity field are due to small fractures with low transmissivity and hence also low porosity. Figure 7-9 provides support for this explanation. When isolated and stagnant parts are removed 66% of all cells have a porosity $\leq 10^{-7}$.

A visualization of the kinematic porosity (θ_c) and flow field is shown in Figure 7-10. The porosity is illustrated with an isosurface for a value of 3×10^{-5}, while the isosurface for the magnitude of the Darcy flux has a value of 3×10^{-11} m/s (this was the value that identified stagnant volumes). The flow direction is from west to east.

7.4 Gravitational effects

At the Äspö HRL old water types (like Glacial water) have been found already at a depth of a few hundred metres. As discussed earlier, it is possible to explain the storage of water by a slow exchange with the storage volumes. Gravitational effects may however also contribute to the isolation of a water volume; salt water in the bottom of a fracture is not easily replaced by fresh water. In this test it will be demonstrated that water can be stored for long periods even without storage volumes.

A qualitative study of the gravitational effects will be carried out. As in the previous case we specify a pressure gradient in the west to east direction. The inflow and outflow sections are however now limited to a 10 m high horizontal band at a depth of 380 m. The initial salinity in the domain is zero, while the inflowing water has a salinity that varies in time, according to Figure 7-11. The total simulation time is 10,000 years. What one can expect is that the salt water will replace the water in the lower half of the domain, while some water with zero salinity may remain (note that the inflowing water always has a salinity > 0%) in the upper half of the domain.

The result after 10,000 years of simulation can be studied in Figure 7-11. The two vertical sections show the result with (top) and without gravity activated. Obviously gravity is a very important factor when storage of old water types is to be analyzed.

A comment may be needed on the "horizontal band of 10 m" giving the inflow and outflow boundaries. The salinity of the inflowing water is intended to illustrate different stages, with different salinities, of the Baltic Sea. In the present model set-up we do not simulate the contact with the Baltic Sea, as the top of the model domain is at a depth of 200 m, and we are thus forced to specify "unrealistic" boundary conditions. It should however be noted that the purpose of the simulation is to illustrate the effect of density variations, in a qualitative way.

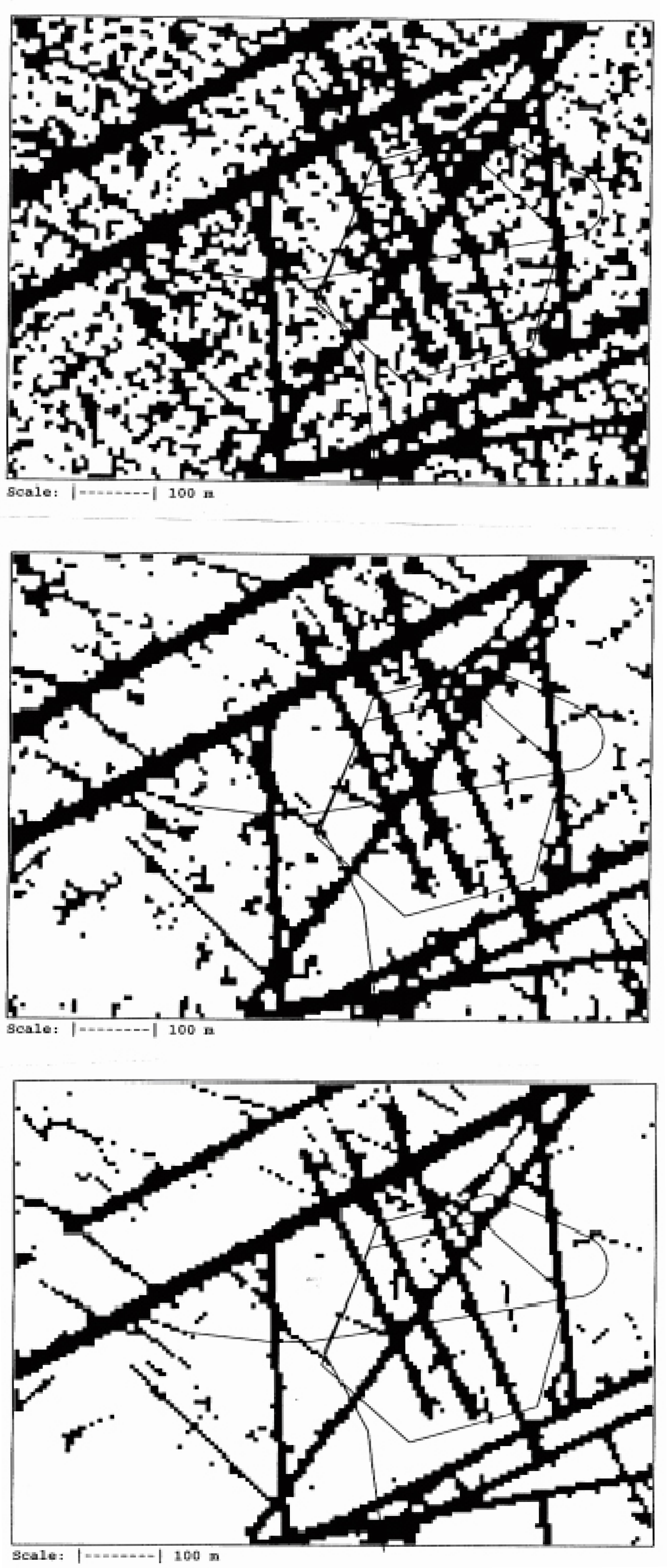

Figure 7-8. *Kinematic porosity fields at a depth of 450 m, based on all generated fractures (top), all connected fractures (middle) and all connected fractures disregarding stagnant volumes. All cells with a porosity >0 are marked black.*

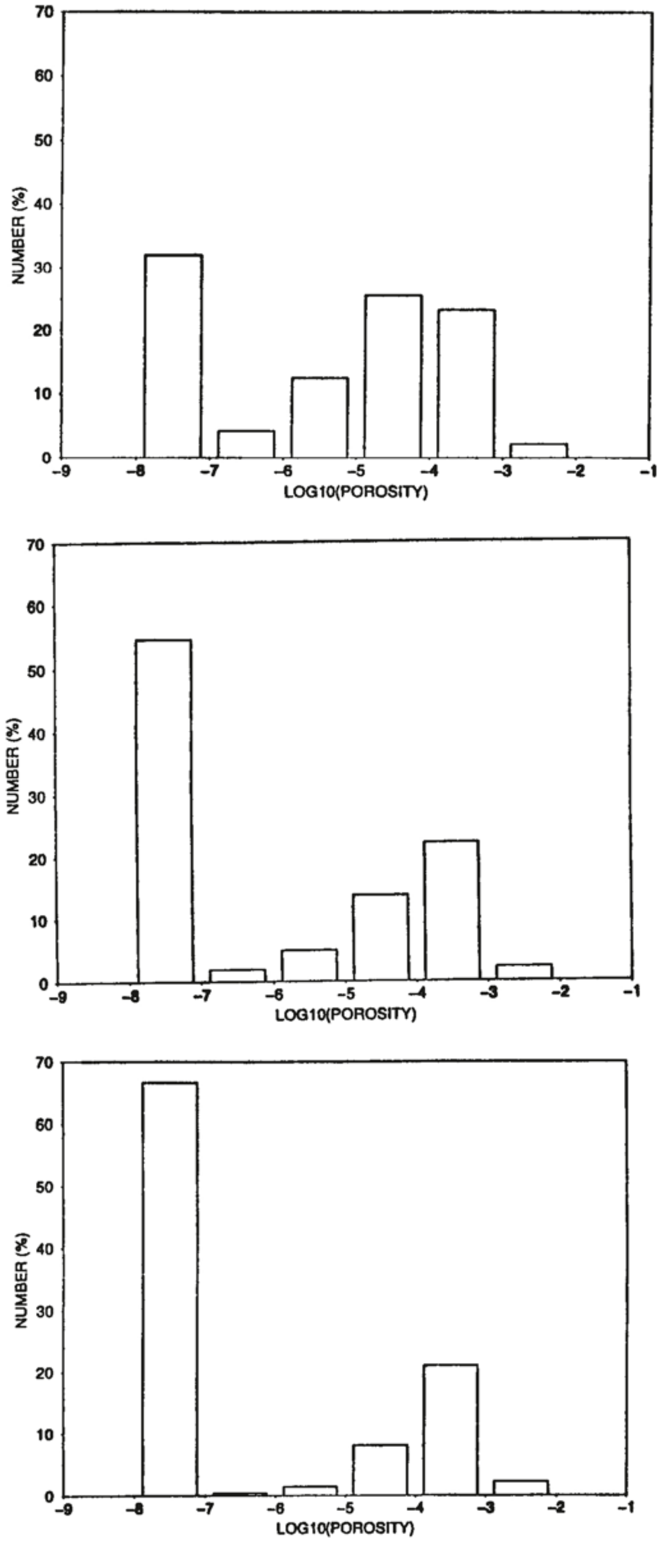

Figure 7-9. *Porosity distribution in the computational grid. Number of cells with different kinematic porosity shown for the case where all generated fractures are kept (top), isolated fractures removed (middle) and isolated fractures and stagnant volumes removed.*

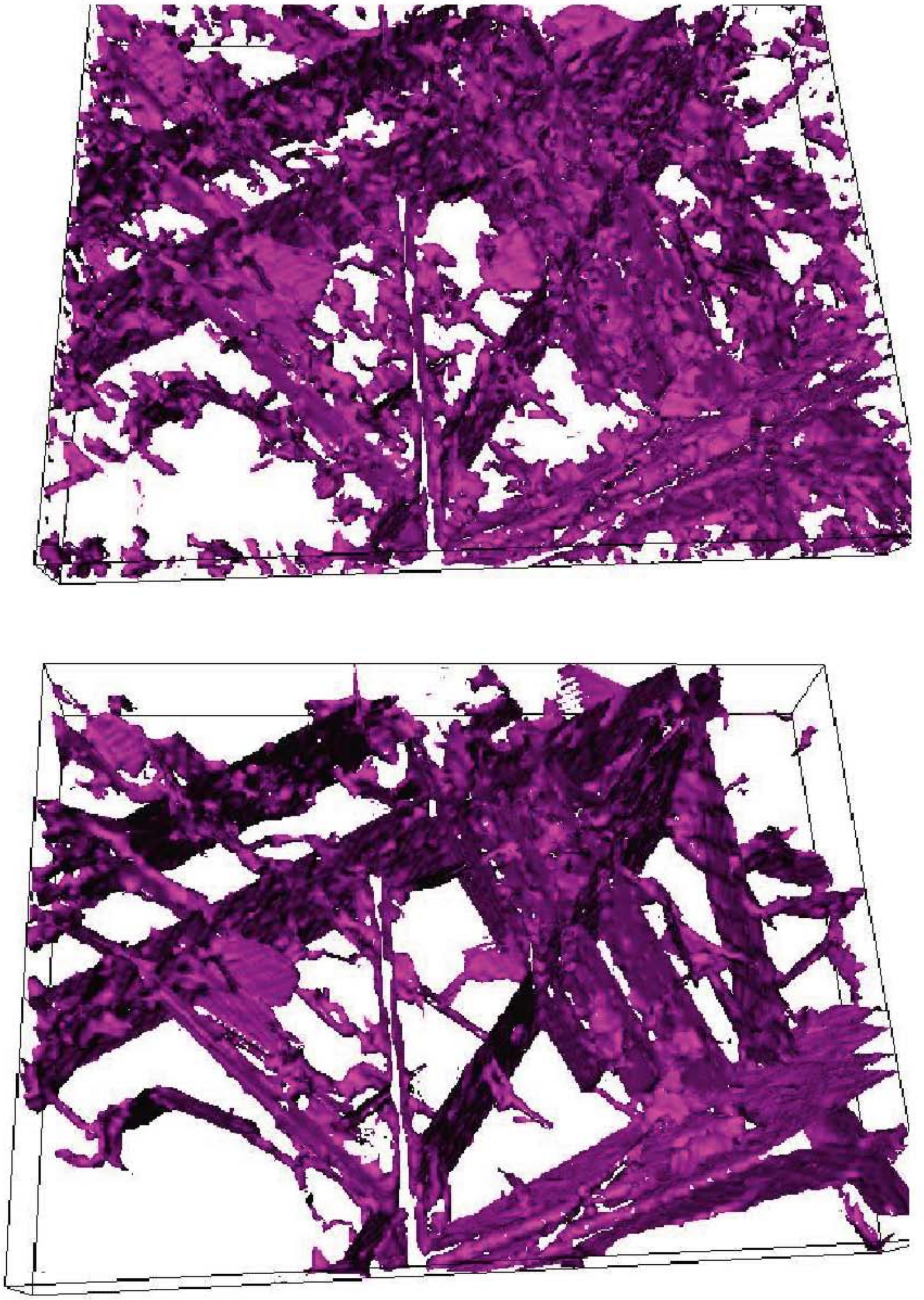

Figure 7-10. Illustration of porosity (top) and flow fields. Depth interval shown is 400 to 500 m below ground level. The flow is from West to East. View from South. The figures are isosurfaces (surfaces of equal value) of porosity and absolute flow magnitude. Colour has no significance.

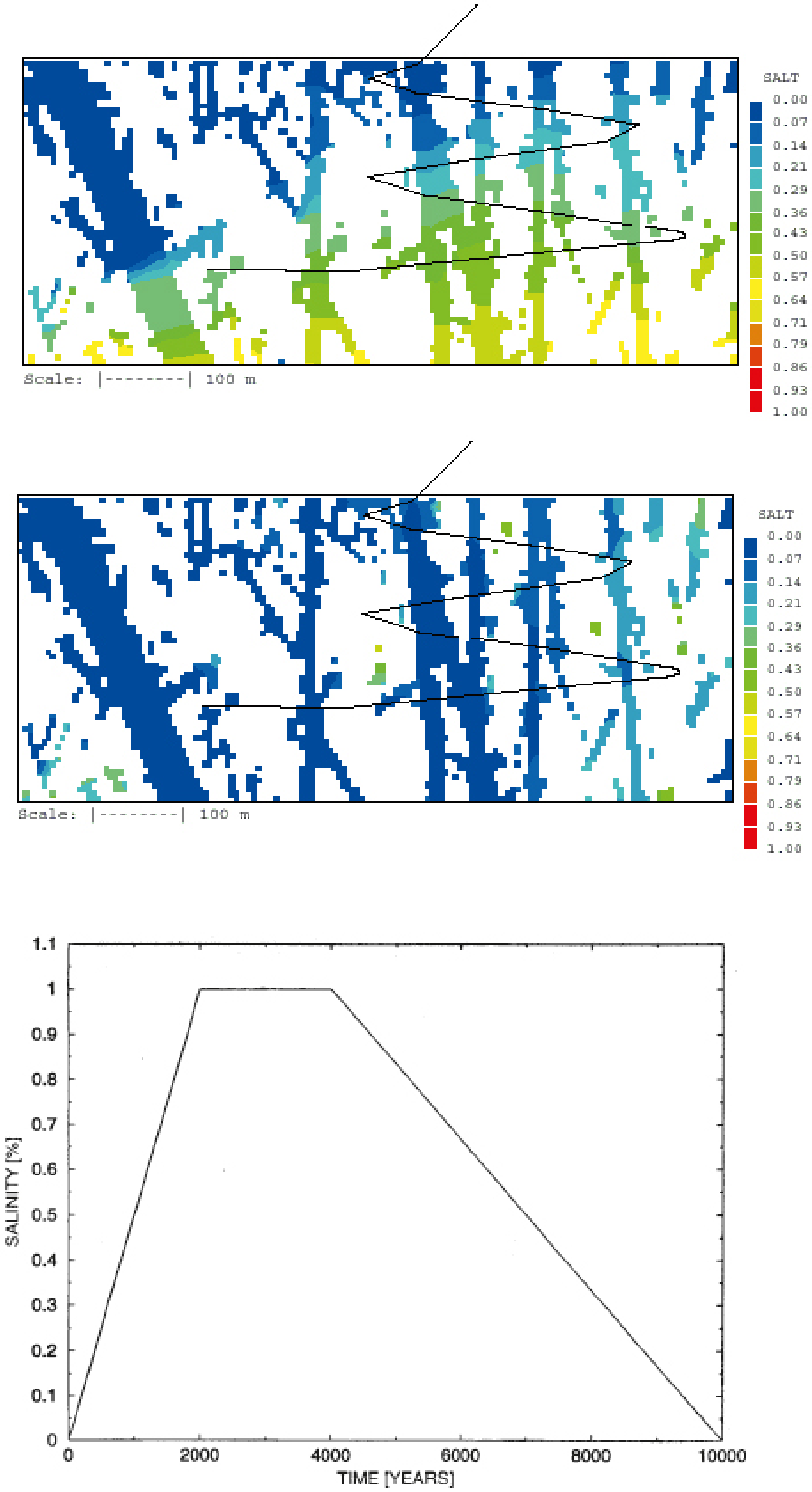

***Figure 7-11.** Effect of gravity. Vertical sections of salinity (in %) field after 10,000 years of simulation with (top) and without gravity activated (middle). Salinity of inflowing water as a function of time (bottom).*

7.5 PARTRACK

Transport simulations can be based on two principally different methods, solving an advection/diffusion equation for the solute or tracking particles. In DarcyTools both methods are used. It is of course of value to base both methods on the same concepts and assumptions concerning the subgrid processes.

The particle tracking routine PARTRACK is described and tested in Svensson (2001a). That version was however based on a lognormal distribution of rate coefficients. FRAME, as described in this report, is based on power-law distributions, which are preferred as the general fracture network is based on such distributions.

As part of the general development of FRAME, a power-law distribution has also been introduced in PARTRACK. The objective of this section is to show some sample results that demonstrate that this has been achieved.

As PARTRACK is now based on FRAME, it will also use the same input parameters. For the results to be presented the following was specified: $\beta_t = 10$, $k = 1.8$ and $D_e = 10^{-10}$ m²/s (constant for the applications presented).

A one-dimensional channel with a steady state flow, with uniform velocity, is used. The length of the channel is 10 m and the transport velocity 10^{-4} m/s. This gives an advective transport time of 10^5 s (» 28 hours). The concentration at the outlet as a function of time, i.e. the breakthrough curve (BTC), is used to illustrate the results.

In Figure 7-12, three BTC:s are shown. If no dispersion effects are active, all particles will arrive after about 27 hours. If Taylor dispersion is added an insignificant dispersion will result for $D_m = 10^{-10}$ m²/s. Decreasing D_m to 10^{-12} m²/s gives some dispersion as can be seen in Figure 7-12. If FRAME is added, the BTC will be significantly modified as can be expected.

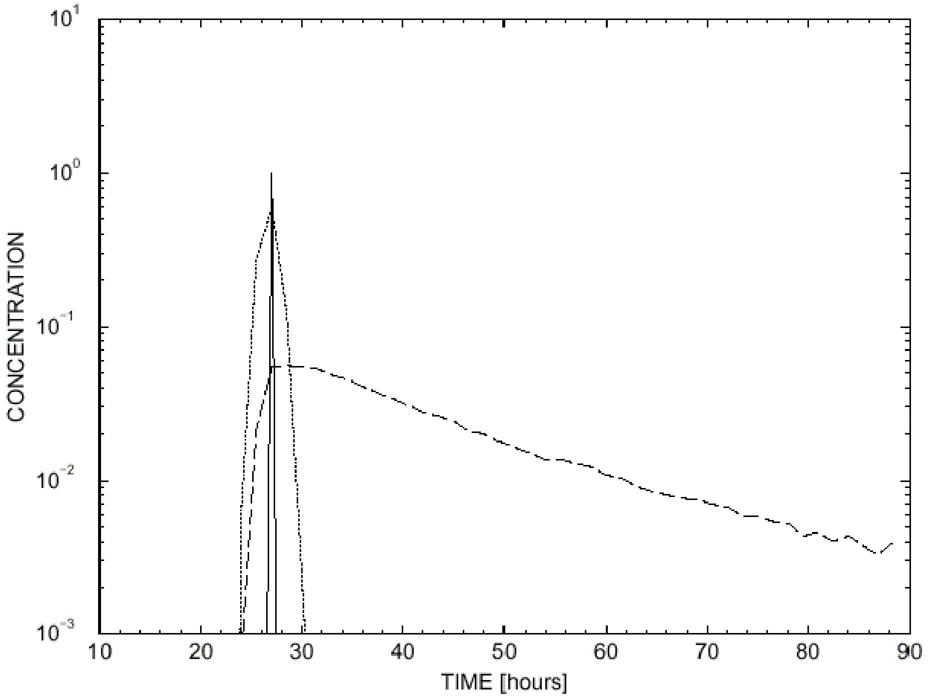

Figure 7-12. *BTC:s in a one-dimensional channel.*
——— *No dispersion.*
········ *Taylor dispersion added ($D_m = 10^{-12}$ m²/s).*
------- *FRAME and Taylor dispersion added.*

Next we use the laboratory model in order to show a real world application. In the West to East flow considered, particles are released in fracture zone EW1, see Figure 1-1, and then tracked through the domain till they reach the eastern boundary. Figure 7-13 shows the flow paths generated by 100 particles. The main flow path is through EW1, changing to the NNW structures and leaving through NE1. Note that in this view from above, NE1 gives a wider impression, as this zone is not vertical. It is also worth noting that rather few flow paths are active in the transport.

The only objective of these simulations is to show some introductory simulations from PARTRACK and the subgrid model FRAME. More sensitivity studies and applications will be presented elsewhere. Verification and Validation studies are also found in Report 2.

7.6 Conclusions

The key feature of the GEHYCO method is that properties (conductivity, flow wetted surface and kinematic porosity) are defined for conductive elements that form a fracture network. The specific results from the present study can be summarized as follows:

- the fracture network generates a connected system of pore-space that we define as the kinematic porosity. Part of this porosity is defined as stagnant volumes, based on a flow criterion,
- storage volumes are representing fractures smaller than the minimum fracture size in the network and all other volumes that exchange matter with the kinematic volumes by molecular diffusion only. Computationally storage volumes are simulated by the model FRAME,
- simple test cases, generic studies and applications to the Äspö HRL demonstrate that the concepts are useful and easily employed in numerical models of the continuum type.

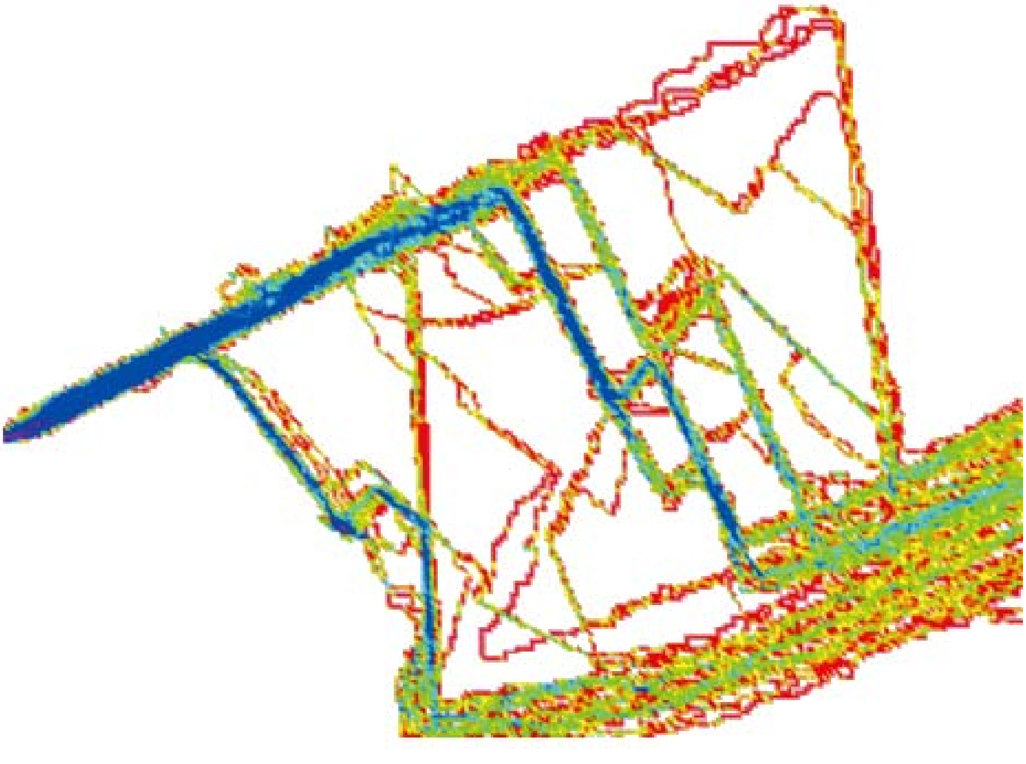

Figure 7-13. *Flow channels formed by 100 particle tracks in a flow field with gradient from West to East. Blue indicates high intensity of tracks, red low.*

8 Discussion

Even if the main part of this report is, intentionally, short it may be difficult to “put the pieces together” and get a good grasp of DarcyTools. We will therefore use the discussion section to summarize the key features of DarcyTools and also to give a hint about possible future developments.

Key features:

- **Mathematical model.** DarcyTools is based on conservation laws (mass, heat, momentum and mass fractions) and state laws (density, porosity, etc.). The subgrid model utilizes the multi-rate diffusion concept and the fracture network (resolved and subgrid) is based on fractal scaling laws.
- **Unstructured grid.** DarcyTools is based on a Cartesian unstructured grid, which offers great flexibility in description of geometries.
- **Continuum model.** Even if a fracture network forms the basis of the approach, DarcyTools should be classified as a continuum porous-medium (CPM) model.
- **Fractures and fracture network.** Fractures and deformation zones are idealised as conductive elements, to which properties (conductivity, porosity, flow wetted surface, etc.) are ascribed. Empirical laws are used for the determination of these properties. The fracture network is based on fractal scaling laws and statistical distributions (random in space, Fisher distribution for orientation, etc).
- **GEHYCO.** This is the algorithm, based on the intersecting volume concept that transforms the fracture network (with properties of conductive elements) to grid cell properties.
- **FRAME.** Subgrid processes are parameterized as “diffusive exchange with immobile zones”. FRAME uses the multi-rate diffusion model and fractal scaling laws, to formulate a simple and effective subgrid model.
- **SOLVE.** When the continuum model is generated, effective CFD-methods are used to solve the resulting finite-volume equations. DarcyTools uses the MIGAL-solver, which is a multigrid solver with the capability to solve coupled problems (like pressure and salinity) in a fully coupled way. A parallel option takes advantage of multi-core processors.
- **PARTRACK.** This particle tracking algorithm is fully integrated with DarcyTools and uses the same basic concepts as FRAME. PARTRACK can handle Taylor dispersion, sorption and matrix diffusion simultaneously in large 3D grids ($> 10^6$ cells).
- **Verification and Validation.** A set of verification and validation studies is presented (see Report 2). This is considered to be an essential feature of the code.

Future versions

It is expected that Version 3.4 will last for several years to come. Detailed improvements will most certainly be done, motivating future releases, as experiences from applications are gathered. It is also expected that technical developments (hardware, numerical techniques, etc) will be implemented.

The present view is that Version 4.0 will include a Navier-Stokes solver. This feature will open new possibilities to simulate, for example, flow and transport inside a fracture.

9 Conclusion

The main objective of this report is to provide the theoretical basis of DarcyTools. The main part of the report is written in a descriptive style, with the intention that also non-specialists in groundwater modelling may find it accessible. More detailed accounts of various topics are provided in appendices.

It is the ambition to establish DarcyTools as a state of the art computer code for simulation of flow and transport in fractured and/or porous media. Many novel and powerful features have been introduced. These features have been verified and also been shown to be “fit for purpose” considering the applications at hand.

10 References

SKB's (Svensk Kärnbränslehantering AB) publications can be found at www.skb.se/publications.

AIAA Journal, 1998. Special issue. Vol 36, No 5. The American Institute of Aeronautics and Astronautics.

Andersson J, Hermansson J, Elert M, Gylling B, Moreno L, Selroos J-O, 1998. Derivation and treatment of the flow wetted surface and other geosphere parameters in the transport models FARF31 and COMP23 for use in safety assessment. SKB R-98-60, Svensk Kärnbränslehantering AB.

Casey M, Wintergerste T (eds), 2000. Best practice guidelines. Version 1. ERCOFTAC Special Interest Group on "Quality and Trust in Industrial CFD". European Research Community on Flow, Turbulence and Combustion.

Cliffe K A, Morris S T, Porter J D, 1998. Assessment model validity document. NAMMU: a program for calculating groundwater flow and transport through porous media. SKB R-99-51, Svensk Kärnbränslehantering AB.

Dershowitz W, Eiben T, Follin S, Andersson J, 1999. SR 97 – Alternative models project. Discrete fracture network modelling for performance assessment of Aberg. SKB R-99-43, Svensk Kärnbränslehantering AB.

Enssle C P, Poppei J, 2010. Implementation and testing of an improved methodology to simulate resaturation processes with DarcyTools. SKB R-09-54, Svensk Kärnbränslehantering AB.

Ferry M, 2002. MIGAL. [Online]. Available at: http://www.mfrdc.com/migal.htm.

Fisher N I, Lewis T, Embleton B J J, 1993. Statistical analysis of spherical data. Cambridge: Cambridge University Press.

Follin S, Stigsson M, Svensson U, 2005. Variable-density groundwater flow simulations and particle tracking – numerical modelling using DarcyTools. Preliminary site description Simpevarp subarea – version 1.2. SKB R-05-11, Svensk Kärnbränslehantering AB.

Follin S, Stigsson M, Svensson U, 2006. Hydrogeological DFN modelling using structural and hydraulic data from KLX04. Preliminary site description Laxemar subarea – version 1.2. SKB R-06-24, Svensk Kärnbränslehantering AB.

Forsmark T, Rhén I, 1999. Äspö Hard Rock Laboratory. Prototype repository. Hydrogeology interference test campaign 1 after drill campaign 3. SKB IPR-00-07, Svensk Kärnbränslehantering AB.

Gómez-Hernández J J, Hendricks Franssen H J W M, Sahuquillo A, Capilla J E, 1999. Calibration of 3-D transient groundwater flow models for fractured rock. In: Stauffer F, Kinzelbach W, Kovar K, Hoehn E (eds). Calibration and reliability in groundwater modelling: coping with uncertainty: proceedings of the ModelCare'99 conference held in Zurich, Switzerland, 20–23 September 1999. Wallingford: IAHS. (IAHS Publication 265), pp 185–194.

Haggerty R, Gorelick S M, 1995. Multiple-rate mass transfer for modeling diffusion and surface reactions in media with pore-scale heterogeneity. Water Resources Research, 31, pp 2383–2400.

Haggerty R, McKenna S A, Meigs L C, 2000. On the late-time behavior of tracer test breakthrough curves. Water Resources Research, 36, pp 3467–3479.

Harlow F H, Welsch J E, 1965. Numerical calculations of time-dependent viscous incompressible flow of fluid with free surface. Physics of Fluids, 8, pp 2182–2189.

Jackson C P, Hoch A R, Todman S, 2000. Self-consistency of heterogeneous continuum porous medium representation of a fractured medium. Water Resources Research, 36, pp 189–202.

La Pointe P R, Wallman P, Follin S, 1995. Estimation of effective block conductivities based on discrete network analyses using data from the Äspö site. SKB TR 95-15, Svensk Kärnbränslehantering AB.

La Pointe P R, Cladouhos T, Follin S, 1999. Calculation of displacements on fractures intersecting canisters by earthquakes: Aberg, Beberg and Ceberg examples. SKB TR-99-03, Svensk Kärnbränslehantering AB.

Neretnieks I, 1993. Solute transport in fractured rock -applications to radionuclide waste repositories. In: Bear J, Tsang C-F, de Marsily G (eds). Flow and contaminant transport in fractured rock. San Diego: Academic Press, pp 39–127.

Niemi A, Kontio K, Kuusela-Lahtinen A, Vaittinen T, 1999. Estimation of block conductivities from hydrologically calibrated fracture networks – description of methodology and application to Romuvaara investigation area. Posiva 99-19, Posiva Oy, Finland.

Outters N, Shuttle D, 2000. Sensitivity analysis of a discrete fracture network model for performance assessment of Aberg. SKB R-00-48, Svensk Kärnbränslehantering AB.

Patankar S V, 1980. Numerical heat transfer and fluid flow. New York: Hemisphere. (Series in computational methods in mechanics and thermal sciences).

Pozdniakov S P, Tsang C-F, 1999. A semianalytical approach to spatial averaging of hydraulic conductivity in heterogeneous aquifers. Journal of Hydrology, 216, pp 78–98.

Renard P, de Marsily G, 1997. Calculating equivalent permeability: a review. Advances in Water Resources, 20, pp 253–278.

Rhén I (ed), Gustafson G, Stanfors R, Wikberg P, 1997. Äspö HRL – Geoscientific evaluation 1997/5. Models based on site characterization 1986–1995. SKB TR-97-06, Svensk Kärnbränslehantering AB.

Ross, S M, 1985. Introduction to probability models. 3rd ed. Orlando, FL: Academic Press.

Sahimi M, 1995. Flow and transport in porous media and fractured rock: from classical methods to modern approaches. Weinheim: VCH.

Spalding D B, 1981. A general purpose computer program for multi-dimensional one- and two-phase flow. Mathematics and Computers in Simulation, 8, pp 267–276. (See also http://www.cham.co.uk/).

Stanfors R, Rhén I, Tullborg E-L, Wikberg P, 1999. Overview of geological and hydrogeological conditions of the Äspö hard rock laboratory site. Applied Geochemistry, 14, pp 819–834.

Svensson U, 1991. Groundwater flow at Äspö and changes due to the excavation of the laboratory. SKB HRL Progress Report 25-91-03, Svensk Kärnbränslehantering AB.

Svensson U, 1997a. A regional analysis of groundwater flow and salinity distribution in the Äspö area. SKB TR 97-09, Svensk Kärnbränslehantering AB.

Svensson U, 1997b. A site scale analysis of groundwater flow and salinity distribution in the Äspö area. SKB TR 97-17, Svensk Kärnbränslehantering AB.

Svensson U, 1999a. Representation of fracture networks as grid cell conductivities. SKB TR-99-25, Svensk Kärnbränslehantering AB.

Svensson U, 1999b. A laboratory scale analysis of groundwater flow and salinity distribution in the Äspö area. SKB TR-99-24, Svensk Kärnbränslehantering AB.

Svensson U, 2001a. PARTRACK – A particle tracking algorithm for transport and dispersion of solutes in a sparsely fractured rock. SKB R-01-16, Svensk Kärnbränslehantering AB.

Svensson U, 2001b. A continuum representation of fracture networks. Part I: Method and basic test cases. Journal of Hydrology, 250, pp 170–186.

Svensson U, 2001c. A continuum representation of fracture networks. Part II: Application to the Äspö Hard Rock Laboratory. Journal of Hydrology, 250, pp 187–205.

Svensson U, 2001d. Äspö Hard Rock Laboratory. Prototype repository. Groundwater flow, pressure and salinity distributions around the Prototype repository. Continuum model No 1. SKB IPR-01-40, Svensk Kärnbränslehantering AB.

Svensson U, 2010a. DarcyTools, Version 3.4. Verification, validation and demonstration, SKB R-10-71, Svensk Kärnbränslehantering AB.

Svensson U, 2010b. Äspö Task Force on modelling of groundwater flow and transport of solutes. Task 7A, 7B and 7C. Numerical simulations of flow and transport at the Olkiluoto site, Finland. SKB P-11-17, Svensk Kärnbränslehantering AB.

Svensson U, 2010c. Evaluation of a new method to estimate the hydration time of the tunnel backfill. SKB R-10-06, Svensk Kärnbränslehantering AB.

Svensson U, Ferry M, 2010. DarcyTools, Version 3.4. User's guide. SKB R-10-72, Svensk Kärnbränslehantering AB.

Svensson U, Follin S, 2004. Äspö Hard Rock Laboratory. Äspö Task Force. Task 6A, 6B and 6B2. Simulation of tracer transport considering both experimental and natural time scales. SKB IPR-04-42, Svensk Kärnbränslehantering AB.

Svensson U, Laaksoharju M, Gurban I, 2002. Impact of the tunnel construction on the groundwater system at Äspö. Task 5. Äspö Task Force on groundwater flow and transport of solutes. SKB IPR-02-45, Svensk Kärnbränslehantering AB.

Wen X H, Gómez-Hernández J, 1996. Upscaling hydraulic conductivities in heterogeneous media: an overview. Journal of Hydrology, 183, pp ix–xxxii.

Winberg A (ed), 1998. Äspö Hard Rock Laboratory. TRUE Block Scale Project. Scientific and technical status. Position report prepared for the 2nd TRUE Block Scale review meeting, Stockholm, Nov 17, 1998. SKB IPR-99-07, Svensk Kärnbränslehantering AB.

Winberg A (ed), 2000. TRUE Block Scale Project. Final report of the detailed characterisation stage. Compilation of premises and outline of programme for tracer tests in the block scale. SKB ICR-00-02, Svensk Kärnbränslehantering AB.

Winberg A, Andersson P, Hermanson J., Byegård J, Cvetkovic V, Birgersson L, 2000. Äspö Hard Rock Laboratory. Final report of the first stage of the tracer retention understanding experiments. SKB TR-00-07, Svensk Kärnbränslehantering AB.

Appendix A

Numerical Methods

A.1 Introduction

DarcyTools computes fracture network flows using a continuum model in which the mass conservation Equation A-1 is associated to several mass fraction transport Equations A-2 for the salinity and/or particle mass concentrations, and to a heat transport Equation A-3. In relations (1), (2) and (3) ρ, *u, v, w, T* and *C* represent respectively the fluid density, the velocity components, the temperature and the mass fraction of the transported quantity. Q, Q_c and Q_T are source terms per unit volume of fluid mass (i.e. injection-withdrawal), of mass of transported quantity (e.g. local exchanges with the rock) and of heat (i.e. enthalpy).

$$\frac{\partial \rho\theta}{\partial t} + \frac{\partial}{\partial x}(\rho u) + \frac{\partial}{\partial y}(\rho v) + \frac{\partial}{\partial z}(\rho \omega) = Q \tag{A-1}$$

$$\begin{aligned} \frac{\partial \rho\theta\, C}{\partial t} &+ \frac{\partial}{\partial x}\left(\rho u C - \rho\gamma D_x \frac{\partial C}{\partial x} \right) \\ &+ \frac{\partial}{\partial y}\left(\rho v C - \rho\gamma D_y \frac{\partial C}{\partial y} \right) \\ &+ \frac{\partial}{\partial z}\left(\rho w C - \rho\gamma D_z \frac{\partial C}{\partial z} \right) = QC + Q_C \end{aligned} \tag{A-2}$$

$$\begin{aligned} \frac{\partial \left(\rho\theta c_p + (1-\theta)c \right) T}{\partial t} &+ \frac{\partial}{\partial x}\left(\rho u c_p T - \lambda_x \frac{\partial T}{\partial x} \right) \\ &+ \frac{\partial}{\partial y}\left(\rho v c_p T - \lambda_y \frac{\partial T}{\partial y} \right) \\ &+ \frac{\partial}{\partial z}\left(\rho w c_p T - \lambda_z \frac{\partial T}{\partial z} \right) = Q\, c_p T + Q_T \end{aligned} \tag{A-3}$$

D_x, D_y and D_z are the normal terms of the diffusion-dispersion tensor. λ_x, λ_y and λ_z are the normal terms of the equivalent (i.e. rock with fluid) thermal conductivity tensor, c is the rock thermal capacity and c_p the specific heat of the fluid.

The mass conservation equation is turned into a pressure equation under the well known Darcy's assumption (Equation A-4).

$$\begin{aligned} \rho u &= -\frac{K_x}{g}\frac{\partial P}{\partial x} \\ \rho v &= -\frac{K_y}{g}\frac{\partial P}{\partial y} \\ \rho w &= -\frac{K_z}{g}\frac{\partial P}{\partial z} - K_z(\rho - \rho_0) \end{aligned} \tag{A-4}$$

where K_x, K_y and K_z are the local hydraulic conductivities in x, y and z direction, g the gravity acceleration, ρ_0 a reference fluid density (8) and P the dynamic fluid pressure relative to the reference hydrostatic pressure.

$$P = p + \rho_0 g\, z \tag{A-5}$$

The hydraulic conductivities K are related to the permeability k field through relation (6):

$$K = \frac{\rho g k}{\mu} \tag{A-6}$$

The fluid property like the dynamic viscosity μ, the density ρ and the specific heat c_p are given by state laws:

$$\mu = \mu_0[1 + a_1S + a_2S^2 + b_1(T-T_\mu) + b_2(T-T_\mu)^2]^{n_\mu} \tag{A-7}$$

$$\rho = \rho_0[1 + a_1S + a_2S^2 - \beta_1(T-T_\rho) - \beta_2(T-T_\rho)^2] \tag{A-8}$$

$$c_p = c_{p0}\,(1 + c_1S + c_2S^2) \tag{A-9}$$

while the porosity θ and the compaction of the matrix γ are provided with the following dependencies:

$$\theta = \theta_0\,\gamma \tag{A-10}$$

$$\gamma = 1 + (\sigma/\theta_0)(P-P_{ref})/\rho g \tag{A-11}$$

In the above formulas S represents the salinity (salt mass fraction), θ_0 a reference porosity field given for a reference pressure field P_{ref}, σ the specific storativity field. n_μ, a_i, b_i, c_i, α_i, β_I, μ_0, ρ_0, c_{p0}, T_μ, and T_ρ are constants.

A.1.1 Finite Volume Integration

The finite volume method integrates Equations A-1, A-2 and A-3 over the faces of a finite number of control volumes by converting volume integrals into surface integrals using Ostrogradsky's theorem:

$$\int_V div(\vec{F})\,dV = \int_{\partial V} \vec{F} \cdot \vec{n}\,dA \tag{A-12}$$

So that, according to the Mean Value Theorem:

$$\int_V div(\vec{F})\,dV = \sum_{i=1}^{nbfaces} A_i \vec{F}_i \cdot \vec{n}_i \tag{A-13}$$

where, A_i and n_i are respectively the area and the outside-normal of the cell face named i and where the field value F_i is evaluated at face center.

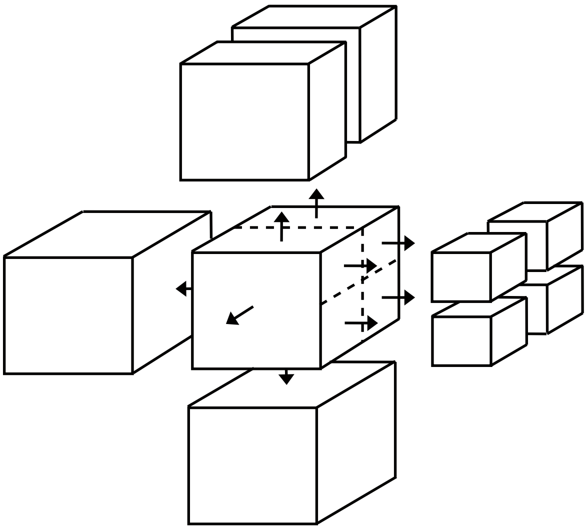

Figure A-1. Unstructured Cartesian control volumes, faces and normals.

A.1.2 Grid arrangement

Among the common grid arrangements, DarcyTools uses the “node-centered” arrangement in which the pressure and the scalar variables (mass fractions) are located at center of grid cells. The main advantage of this formulation is in the fact that control volumes coincide with grid cells and that cell vertexes are directly defined by grid nodes.

The main drawback is in the fact that, for non-uniform meshes, the faces of control volumes may not be located mid-way between variable locations or may not be orthogonal to the line joining cell centers. More sophisticated interpolations are therefore necessary to get a second order discretisation of convective and diffusive fluxes.

A.1.3 Stability

The strength of the finite volume integration is its conservative formulation for which any flux getting out from a control volume is automatically entering the neighboring volume. Nevertheless this strength may be a drawback when considering the convergence process. Given a bounded conservative scheme, the convective term interpolation for an east cell face can be written:

$$\vec{F}.\vec{n}\Big|_e = \phi_e\ \rho\vec{u}.\vec{n}\Big|_e = \left(\alpha_e\ \phi_E + (1-\alpha_e)\phi_P\right)\ \rho\vec{u}.\vec{n}\Big|_e \qquad \text{(A-14)}$$

where the value of α_e depends on u to ensure the monotony and remains in the interval [0,1] to ensure the boundess of the scheme. The subscripts e, E, and P indicate respectively the east face value, the east variable and the center variable.

Therefore, for the convective term of the transport Equation A-2, by applying relation (14) for the integrals of relation (12) leads to the following algebraic relation:

$$\int_V div\,(\rho\vec{u}\phi)\,dV = \left(\int_V div\,(\rho\vec{u})\,dV - \sum_{nb} a_{nb}\right)\phi_P + \sum_{nb} a_{nb}\phi_{nb} \qquad \text{(A-15)}$$

Because of Equation A-1 and for stationary problem with no internal mass source term, relation (15) apparently leads to a central coefficient (applied to ϕ_P) equal to the opposite sum of neighboring coefficients. This property, even if not necessary, is highly desirable for stability. Unfortunately, during the convergence process, relation (1) may be temporarily highly unsatisfied. Hence, in spite of the bounded form Equation A-14 the discretisation of the transport equation from Equation A-2 may become unstable. For this reason, DarcyTools substitutes the source term *CQ* of Equation A-2 by its evaluation from relation (1) and finally solves Equations A-16 and A-17 instead of Equations A-2 and A-3.

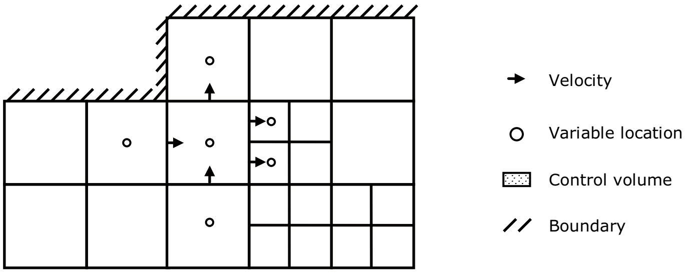

Figure A-2. *Node-centered arrangement labeling.*

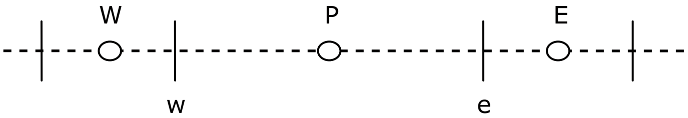

Figure A-3. *East-West stencil labeling.*

$$
\begin{aligned}
\rho\theta\frac{\partial C}{\partial t} &+ \frac{\partial}{\partial x}\left(\rho u C - \rho\gamma D_x \frac{\partial C}{\partial x}\right) \\
&+ \frac{\partial}{\partial y}\left(\rho v C - \rho\gamma D_y \frac{\partial C}{\partial y}\right) \\
&+ \frac{\partial}{\partial z}\left(\rho w C - \rho\gamma D_z \frac{\partial C}{\partial z}\right) = \left(\frac{\partial \rho u}{\partial x} + \frac{\partial \rho v}{\partial y} + \frac{\partial \rho w}{\partial z}\right) C + Q_C
\end{aligned}
\tag{A-16}
$$

$$
\begin{aligned}
\rho\theta\frac{\partial c_p T}{\partial t} &+ \frac{\partial\ (1-\theta)cT}{\partial t} \\
&+ \frac{\partial}{\partial x}\left(\rho u c_p T - \lambda_x \frac{\partial T}{\partial x}\right) \\
&+ \frac{\partial}{\partial y}\left(\rho v c_p T - \lambda_y \frac{\partial T}{\partial y}\right) \\
&+ \frac{\partial}{\partial z}\left(\rho w c_p T - \lambda_z \frac{\partial T}{\partial z}\right) = \left(\frac{\partial \rho u}{\partial x} + \frac{\partial \rho v}{\partial y} + \frac{\partial \rho w}{\partial z}\right) c_p T + Q_T
\end{aligned}
\tag*{(A-17}
$$

The main advantage of this technique is to ensure a central coefficient always equal to the opposite sum of neighboring coefficients. A second advantage is that the source terms (*CQ and* c_pQT) due to fluid mass source disappears from relation (16) and (17). This simplifies the implementation of boundary conditions since the internal mass source terms have to be specified only once: for the mass conservation Equation A-1. In return, the mass fractions C must be specified where the fluid mass source Q is positive (no necessary condition when $Q<0$). It should also be noted that, for time varying density or porosity, the time derivative term lost its conservative form.

A.1.4 Spatial scheme

Also for stability reason, the fluxes discretisation in space must involved both convective and diffusive terms in order to produce positive coefficients. Then, considering the face *f* separating two control volumes I and J,

DarcyTools uses the hybrid scheme to express the fluxes as:

$$F_f = c\phi_f - d\phi_{,xf} = a^-\phi_{P(i)} - a^+\phi_{E(i)} = a^+\phi_{P(j)} - a^-\phi_{W(j)} \tag{A-18}$$

$$
\begin{cases}
a^+ = a^- - c \\
a^- = \max\left(0,\, c,\, \dfrac{h^+c + 2d}{h^+ + h^-}\right)
\end{cases}
\tag{A-19}
$$

with the faces values linearly interpolated as:

$$\phi_f = \frac{h^-\phi_{E(i)} + h^+\phi_{P(i)}}{h^+ + h^-} = \frac{h^-\phi_{P(j)} + h^+\phi_{W(j)}}{h^+ + h^-} \tag{A-20}$$

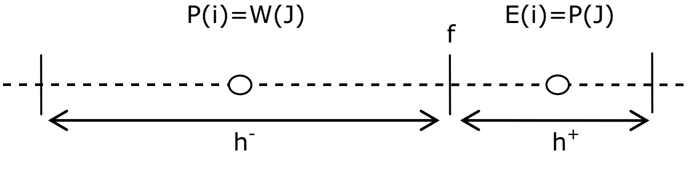

Figure A-4. *East-West face flux labeling.*

A.2 Time derivative

To ensure the precision of time dependent simulations, DarcyTools implements two different implicit time schemes. The default one is the Euler first order implicit scheme given by:

$$\left.\frac{\partial\phi}{\partial t}\right|_n = \frac{\phi_n - \phi_{n-1}}{t_n - t_{n-1}} \qquad \text{(A-21)}$$

The alternative is a second order implicit scheme that differentiates a parabola forced through solutions at three non-equally spaced time levels:

$$\left.\frac{\partial\phi}{\partial t}\right|_n = \frac{2\Delta t_1 + \Delta t_2}{\Delta t_1(\Delta t_1 + \Delta t_2)}\,\phi_n - \frac{\Delta t_1 + \Delta t_2}{\Delta t_1 \Delta t_2}\phi_{n-1} + \frac{\Delta t_1}{\Delta t_2(\Delta t_1 + \Delta t_2)}\phi_{n-2} \qquad \text{(A-22)}$$

where Δt_1 and Δt_2 represent respectively the time steps t_n-t_{n-1} and t_{n-1}-t_{n-2}.

A.2.1 Algebraic Set of Equations

After the discretisation step, Equation A-1 as well as all the Equations A-16 can be written with the general algebraic form:

$$a_p\,\phi_P = \sum_{nb} a_{nb}\phi_{nb} + S_\phi \qquad \text{(A-23)}$$

where a_p and a_{nb} are positive coefficients and where a_p, because of the transient term, is greater than the sum of the neighboring coefficients a_{nb}. Whenever it is possible, if the source term operator S_ϕ depends on the solution field ϕ DarcyTools increases the diagonal dominance of the operator by rewriting it as follows:

$$S_\phi = Q_{src} - Q_{phi}\,\phi_P \quad \text{with} \quad Q_{phi} > 0 \qquad \text{(A-24)}$$

and by including Q_{phi} into the central coefficient.

$$\left(a_p + Q_{phi}\right)\phi_P = \sum_{nb} a_{nb}\phi_{nb} + Q_{src} \qquad \text{(A-25)}$$

This linearization of the operator source term is also a practical way for users to fix different kind of boundary conditions. For example, setting a *BIG* value in Q_{phi} and a *BIGxVAL* value in Q_{src} becomes equivalent to the Dirichlet boundary condition: ϕ=*VAL*. Setting Q_{src} to *VQ* and Q_{phi} to zero is also the easiest way to specify an inlet fluid mass flux in the pressure Equation A-1. When an inlet fluid mass is set (Q>0) it can also be of interest to specify only the inlet salinity instead of fixing the mean cell value by a Dirichlet condition. In that case the implicit input must be removed by setting Q_{phi} to *VQ* and the effective input forced by setting Q_{src} to VQS_{in}.

A.3 Discretisation

With structured grids, local refinements may drastically increase the total number of cells by propagating cell size reductions until boundaries. To avoid this generation of useless cells in regions of poor interest, DarcyTools uses adaptive Cartesian grids. Starting with a single cell that covers the entire domain, the grid generator successively splits cells requiring refinement in two half children cells and repeats this procedure for each direction until the cell size or the total number of cells reaches threshold values.

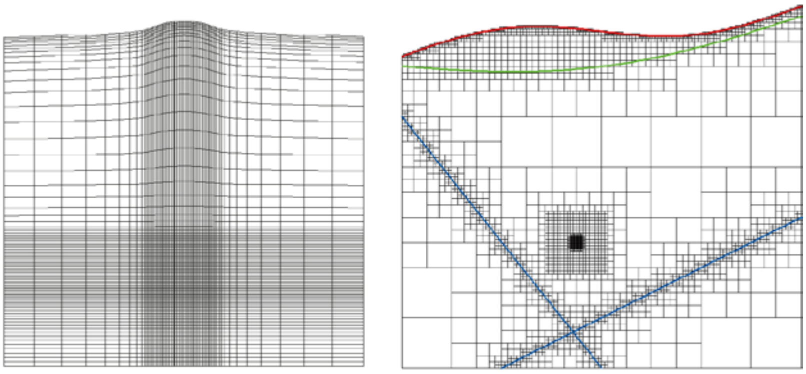

Figure A-5. *Structured vs unstructured grids.*

A.3.1 Grid geometry

To minimize the storage required for grid node coordinates, the cell size and origin location are represented by 4 bytes and 1 byte integers.

```
type T_CELL
 integer(4) :: ix = 0
 integer(4) :: iy = 0
 integer(4) :: iz = 0
 integer(1) :: lx = 0
 integer(1) :: ly = 0
 integer(1) :: lz = 0
 integer(2) :: mk = 0
end type
```

So that cell minimum and maximum coordinates are given by:

```
x0 = xor + dxmin * ix
y0 = yor + dymin * iy
z0 = zor + dzmin * iz

x1 = xor + dxmin * (ix + 2**lx)
y1 = yor + dymin * (iy + 2**ly)
z1 = zor + dzmin * (iz + 2**lz)
```

with

```
dxmin = xspan * 2**(-lm)
dymin = yspan * 2**(-lm)
dzmin = zspan * 2**(-lm)
```

xor, yor and zor represents the origin coordinates of the domain and xspan, yspan and zspan the size of the domain in x, y and z direction. ix, iy and iz are the position indices of the cell, lx, ly and lz are the coarsening levels and lm the maximum allowed coarsening level. The 2 bytes integer attribute mk is a marker used to transfer the cell properties from the grid generator to the solver.

Though cell information could be stored in an octree data structure, DarcyTools implements a fully unstructured data structure for performance and flexibility reasons. Hence, the cells information is stored in a T_CELL array and the connectivity in three T_FACE arrays corresponding to x, y and z faces. Each face contains only two 4 bytes integer values named low and high. These values are the indices of the cells located respectively on the low and high side of the face (e.g. west and east side of an x face).

```
type T_FACE
 integer(4) :: low = 0
 integer(4) :: high = 0
end type
```

A high or low null value indicates that the face is located on the domain boundary. Strictly negative values mean that the face is located on a removed zone boundary whose marker corresponds to the value.

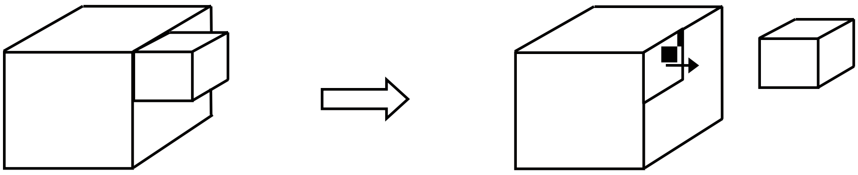

Figure A-6. *Face between unequal sized cells.*

Then, accordingly to relation (13), DarcyTools integrates the divergence term of the continuity and the conservation equations by traversing the faces arrays and by adding the flux contributions to each discrete equation (i.e. to each control volume balance). Since the size of the two linked cells (low and high) may differ due to the local refinement capability, the area of the face involved in the flux evaluation is given by the smallest cell.

```
Ax = dymin * dzmin * 2**(min(lylow,lyhigh)+min(lzlow,lzhigh))
Ay = dxmin * dzmin * 2**(min(lxlow,lxhigh)+min(lzlow,lzhigh))
Az = dxmin * dymin * 2**(min(lxlow,lxhigh)+min(lylow,lyhigh))
```

A.4 Governing equations

The governing equations become:

$$\begin{aligned} h_x h_y h_z \frac{\partial \rho\theta}{\partial t} &+ \sum_i^{xfaces} \delta_i A_{xi} \frac{K_{xi}}{g} \left.\frac{\partial P}{\partial x}\right|_i \\ &+ \sum_j^{yfaces} \delta_j A_{yj} \frac{K_{yj}}{g} \left.\frac{\partial P}{\partial y}\right|_j \\ &+ \sum_k^{zfaces} \delta_k A_{zk} \frac{K_{zk}}{g} \left.\frac{\partial P}{\partial z}\right|_k = h_x h_y h_z Q + S_{DM} \end{aligned} \tag{A-26}$$

$$\begin{aligned} & h_x h_y h_z \rho\theta \frac{\partial C}{\partial t} + \\ & \sum_i^{xfaces} \delta_i A_{xi} \left(\rho_i U_i C_i - \gamma_i D_{xi} \left.\frac{\partial C}{\partial x}\right|_i \right) - C \sum_i^{xfaces} \delta_i A_{xi} \rho_i U_i \quad + \\ & \sum_j^{yfaces} \delta_j A_{yj} \left(\rho_j V_j C_j - \gamma_j D_{yj} \left.\frac{\partial C}{\partial y}\right|_j \right) - C \sum_j^{yfaces} \delta_j A_{yj} \rho_j V_j \quad + \\ & \sum_k^{zfaces} \delta_k A_{zk} \left(\rho_k W_k C_k - \gamma_k D_{zk} \left.\frac{\partial C}{\partial z}\right|_k \right) - C \sum_k^{zfaces} \delta_k A_{zk} \rho_k W_k = h_x h_y h_z Q_C \end{aligned} \tag{A-27}$$

$$\begin{aligned} & h_x h_y h_z \rho\theta \frac{\partial c_p T}{\partial t} + h_x h_y h_z \frac{\partial (1-\theta) c T}{\partial t} + \\ & \sum_i^{xfaces} \delta_i A_{xi} \left(\rho_i U_i c_{pi} T_i - \lambda_{xi} \left.\frac{\partial T}{\partial x}\right|_i \right) - c_p T \sum_i^{xfaces} \delta_i A_{xi} \rho_i U_i \quad + \\ & \sum_j^{yfaces} \delta_j A_{yj} \left(\rho_j V_j c_{pj} T_j - \lambda_{yj} \left.\frac{\partial T}{\partial y}\right|_j \right) - c_p T \sum_j^{yfaces} \delta_j A_{yj} \rho_j V_j \quad + \\ & \sum_k^{zfaces} \delta_k A_{zk} \left(\rho_k W_k c_{pk} T_k - \lambda_{zk} \left.\frac{\partial T}{\partial z}\right|_k \right) - c_p T \sum_k^{zfaces} \delta_k A_{zk} \rho_k W_k = h_x h_y h_z Q_T \end{aligned} \tag{A-28}$$

where the only additional source term is given by:

$$S_{DM} = \sum_k^{zfaces} \delta_k A_{zk} K_{zk} \left(\rho_k - \rho_0 \right) \tag{A-29}$$

the mass fluxes by:

$$\begin{aligned} \rho U A_x &= -A_x \frac{K_x}{g} \frac{\partial P}{\partial x} \\ \rho V A_y &= -A_y \frac{K_y}{g} \frac{\partial P}{\partial y} \\ \rho W A_z &= -A_z \frac{K_z}{g} \frac{\partial P}{\partial z} - A_z K_z \left(\rho - \rho_0 \right) \end{aligned} \tag{A-30}$$

and the normal partial derivatives by:

$$
\begin{aligned}
\left.\frac{\partial \phi}{\partial x}\right|_i &= \frac{\phi_{high} - \phi_{low}}{x_{C_{high}} - x_{C_{low}}} \\
\left.\frac{\partial \phi}{\partial y}\right|_j &= \frac{\phi_{high} - \phi_{low}}{y_{C_{high}} - y_{C_{low}}} \\
\left.\frac{\partial \phi}{\partial z}\right|_k &= \frac{\phi_{high} - \phi_{low}}{z_{C_{high}} - z_{C_{low}}}
\end{aligned}
\tag{A-31}
$$

In relations (26) to (31), the subscripts i, j and k are relative to the x, y and z faces of the given control volume and the δ_i, δ_j and δ_k values are +1 when the faces are east, north or high and –1 otherwise. In relation (31) x_C, y_C and z_C represent the coordinates of the cell center of the high and low cells of the given face.

A.5 Operator format

The DarcyTools unstructured format for the operator *(A)* is as follows: Given N the number of cells and LEN the number of non-zero Aij coefficients MIGAL data structure consists of three arrays:

1- A real array A containing the real values Aij. The first N positions in A contain the diagonal elements Aii of the matrix, in order. Starting from position N+1 and up to LEN, the non-zero elements of A, excluding its diagonal elements, are stored row-wise.

2- An integer array JA containing the column indices of the element Aij as stored in the array A, including its diagonal. The length of JA is LEN.

3- An integer array LA containing the pointers to the beginning of each row in the arrays A and JA. The length of LA is N+1 with LA(N+1) containing the number LEN+1 i.e. the address in A and JA of the beginning of a fictitious row N+1. Since the first N values of A contains the diagonal LA(1) contains the number N+1.

Following this format, the product *P=A.X* can be computed by:

```
N=LA(1)-1
DO I=1,N
 P(I) = A(I)*X(I)
 DO L=LA(I),LA(I+1)-1
 P(I) = P(I) + A(L) * X(JA(L))
 ENDDO
ENDDO
```

When the operator couples *nbv* variables, each A_{ij} coefficient becomes a (nbv,nbv) block instead of being a single real value. However, the connectivity arrays *LA* and *JA* remain identical. Each block is stored in the natural fortran order *A(IV,JV,L)* where *IV* and *JV* represent the variable indexes and L the matrix index. For a block operator the product *P=A.X* can be computed by:

```
N=LA(1)-1
DO I=1,N
 DO IV=1,NBV
  P(IV,I) = A(IV,1,I)*X(1,I)
  DO JV=2,NBV
   P(IV,I) = P(IV,I) + A(IV,JV,I)*X(JV,I)
  ENDDO
  DO L=LA(I),LA(I+1)-1
   DO JV=1,NBV
    P(IV,I) = P(IV,I) + A(IV,JV,L) * X(JV,JA(L))
   ENDDO
  ENDDO
 ENDDO
ENDDO
```

A.6 MIGAL solver

DarcyTools uses the MIGAL algebraic multi-grid solver to solve the successive algebraic sets of equations resulting from discretisation. This use sums up in a single call to the routine MIGAL.

A.6.1 The basics

The set of linear Equations A-23 or resulting of the discretisation of the continuity and the transport equations can be expressed as:

$$A\,x = S \qquad \text{(A-32)}$$

where A represents the matrix of coefficients, x the variables array and S the right hand side vector of source terms.

They are several well-established iterative schemes to solve this set of linear equations. These include Jacobi, Gauss-Seidel, incomplete LU factorization, etc. But, each of them has a rate of convergence depending on the condition number of the matrix A. Hence, as the number of cells will increase, and because of the elliptic nature of the diffusion operator contained in the equation, the condition number of the matrix will increase and the rate of convergence will deteriorate. Further, a characteristic of all these iterative schemes is that the initial rate of convergence is rapid for the first iterations, and deteriorates as the iterations progress. It can be shown that the cause of this slow convergence is primarily the sluggish rate of convergence of the low frequency errors that are present in the solution. As the grid refined, these low frequency errors dominate the overall rate of convergence.

Hence, the concept of the multi-grid technique as implemented by MIGAL is as follows. Given the fact that the low frequencies converge slowly, it is possible to accelerate their rate of convergence by making them behave as high frequencies on coarser grids. For this, the basic principle consists in working on a subset of the fine grid points (e.g. keeping only odd or even nodes) to reduce the number of points and automatically raise the error signal frequency in the transformed grid space (see Figure A-7).

MIGAL proceeds as follows. Consider that we initiate a solution on a given fine grid. A few iterations are then performed on this fine grid to obtain an estimation x_F. For these iterations, the convergence is usually fast.

$$x_F = \tilde{A}^{-1} S \qquad \text{(A-33)}$$

The notation $(\sim)$ means $\tilde{A}^{-1}$ is not the inverse of matrix A but only an approximate (e.g. few relaxations of an iterative solver). Subsequently, the convergence begins to worsen so that the calculations are switches to a coarser grid with the aim of improving the fine grid estimation x_F at lower cost. For that, the residuals and the corresponding defect correction operator are formed on the fine grid and interpolated ("restricted") to the next coarse grid by:

$$R\,A\,\delta x_F = R\,(S - A x_F) \qquad \text{(A-34)}$$

where the restriction operator R (e.g. pure injection) is a $(NI_c \times NI_F)$ matrix that shorten the dimension of the right hand side from NI_F to NI_c.

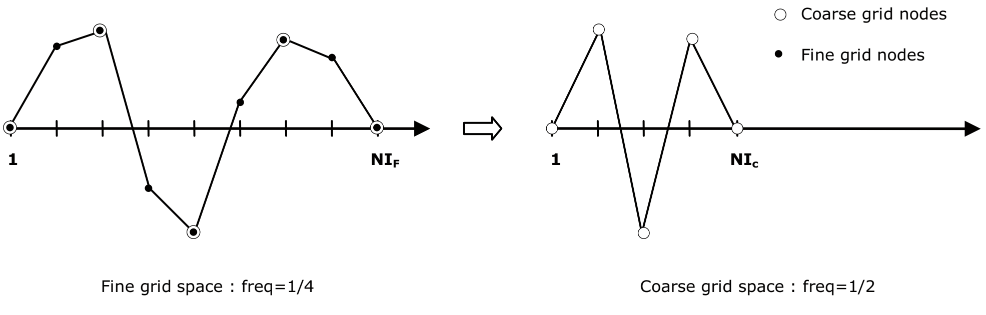

Figure A-7. Fine to coarse grid error frequency mutation.

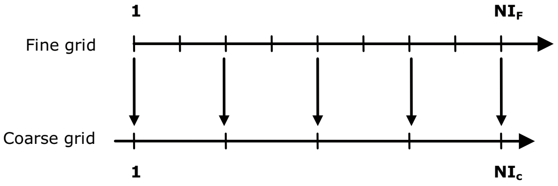

Figure A-8. *Pure injection restriction.*

At this point a second operator is introduced to shorten the left hand side of the operator. It is done by changing the fine grid correction variable δx_F for a coarse grid variable named δx_c so that the former can be interpolated ("prolongated") from the latter by:

$$\delta x_F = P\,\delta x_c \qquad \text{(A-35)}$$

where the prolongation operator P (e.g. linear interpolation) is a $(NI_F \; x \; NI_c)$ matrix that reduces the coarse grid operator size to $(NI_c \; x \; NI_c)$

$$(R\,A\,P)\,\delta x_c = R\,(S - Ax_F) \qquad \text{(A-36)}$$

Once the coarse grid operator (RAP) is formed, a few iterations are performed to obtain δx_c to the required accuracy and the fine grid correction is retrieved using Equation A-35.

Of course, since the error spectrum contains a wide range of frequencies, it is necessary to consider a number of coarse grids and to successively build the coarse operator of the coarse operators. On the coarsest grid, which must be a small grid, a direct solver can be used or, like with MIGAL, the necessary number of iterations can be performed. Finally the manner in which the grids are visited can vary.

In the simplest case, called V-cycle, each grid is visited in turn on the downward and upward legs of a V-cycle. On each grid a number of iterations are performed and the next grid is visited. With the W-cycle, each grid is visited in turn on the downward leg of the a W-cycle, then after that the correction is prolongated by one level, the error is again restricted to the lower level and the correction prolongated up to the next upper level (see Figure A-10). The iterations can be done during both the restriction part of the cycle (downward limb) and during the prolongation part (upward limb).

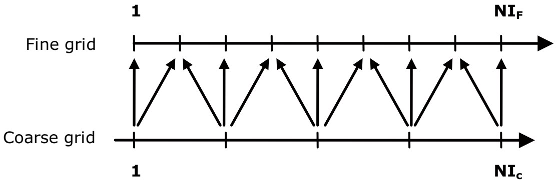

Figure A-9. *Linear prolongation.*

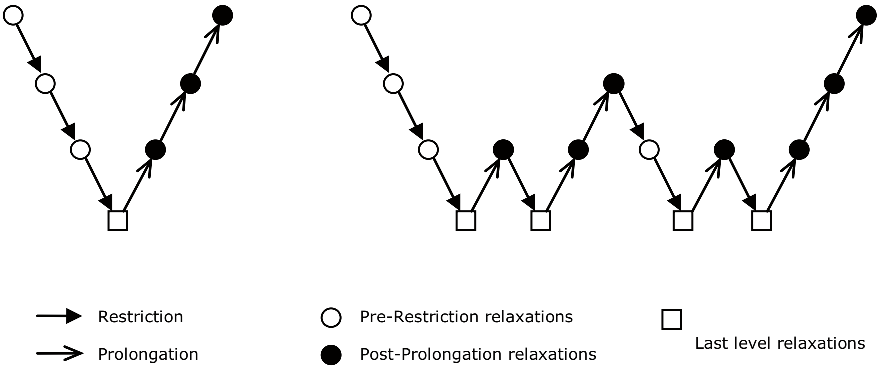

Figure A-10. *V and W multi-grid cycles.*

A.7 GMRES acceleration

The emphasis of basic multi-grid procedures is to improve the performance of the classical iterative solver (smoother) by adapting the operator to their intrinsic capabilities. This technique encounters some limits when the coefficients are highly anisotropic and when the mesh aspect ratios are quite large but the ILU0 smoother of MIGAL has demonstrated to be robust enough in many 3D applications. The main difficulty of the flows processed by DarcyTools comes from the sharp spatial variations of the coefficients that couple the high and low frequencies error components during the restriction/prolongation procedure and finally deteriorate the overall performance. To fight this wavelength coupling problem DarcyTools may use MIGAL as a GMRES preconditioner.

The GMRES method is a projection method based that consists in finding the optimal solution of the system (32) that belongs to the m-th Krylov subspace $K_{m.}$

$$K_m = span\ \{r_0, AM^{-1}r_0, [AM^{-1}]^2 r_0, \ldots, [\mathrm{AM}^{-1}]^{m-1} r_0\} \qquad \text{(A-37)}$$

where r_0 is the initial residual of (32) and where M^{-1} is a right preconditioning matrix whose function is to lower the condition number of the algebraic set of equations.

$$AM^{-1}u = S, \quad u = Mx \qquad \text{(A-38)}$$

For a given dimension *m*, the MIGAL-GMRES algorithm involves an Arnoldi loop that constructs an orthogonal basis of the right-preconditioned Krylov subspace by a modified Gram-Schmidt process, in which the new vector to be orthogonalized is obtained from the previous vector of the process.

The preconditioning matrix is only involved in the $z=M^{-1}v$ products and does not need to be explicitly formulated. Instead, since relation (38) shows that $M=A$ is the best preconditioning choice, some multi-grid cycles of MIGAL are advantageously used to compute an approximated value of z as being the solution of $Az=v$.

The drawback is that, since M now changes for each vector z depending on the convergence of MIGAL, it is necessary to store the orthogonal basis Z_m to retrieve the solution x_m. Therefore, since reaching an expected level of accuracy usually involves large sub-spaces, the method may become impractical because of large memory and computational requirements. For this reason MIGAL use a restarted GMRES procedure (step 4. Figure A-1) which limits the Krylov-subspace basis to a given size and iterates the initial estimation x_0.

```
1.  Start: Choose $x_0$ and a dimension m of the Krylov subspaces and initialize
        a (m+1) x m matrix H  to zero
2.  Arnoldi process:
      •  Compute $r_0=S-Ax_0$, $b=||r_0||$ and $v_1 = r_0/b$
      •  For j=1,…,m
           -  Compute $z_j = M^{-1} v_j$
           -  Compute $w = A z_j$
           -  For i=1,…,j
                 $H_{i,j} = (w,v_i)$
                 $w = w - H_{i,j} v_i$
           -  Compute $h_{j+1,j} = ||w||$ and $v_{j+1} = w/H_{j+1,j}$
      •  Define $Z_m = [z_1,…,z_m]$
3.  From the approximate solution: Compute $x_m = x_0 + Z_m y_m$ where
        $y_m = argmin_y||be_1 - Hy||$ and $e_1=[1,0,…,0]^T$
4.  Restart: if satisfied stop, else set $x_0 = x_m$ and goto 2.
```

Figure A-11. *MIGAL-GMRES algorithm.*

MIGAL preconditions the Krylov subspace by one multi-grid cycle. To increase this number of preconditioning cycles users may specify the parameter IPRECO in the MIGAL parameters list. For particularly difficult problems it is possible, on coarse grid levels, to replace the ILU(0) smoother by a GMRES ILU(0) preconditioned smoother. For this users have to stipulate the size of the desired Krylov subspace by setting the parameter IGMS to any non-zero value. The coarse grid smoother then becomes a GMRES solver right-preconditioned by NBPRER or NBRELAX ILU(0) relaxations depending of the limb of the multi-grid cycle actually performed. For flexibility, the IGMS parameter may be set independently of IGMRES, i.e. that MIGAL can implement different combinations of the multi-grid and GMRES algorithms.

A.8 Agglomeration algorithm

With unstructured meshes, MIGAL uses an agglomeration method for automatic grid coarsening. The idea of the agglomeration method is to fuse together or agglomerate neighbouring fine grid control volumes, creating a smaller set of larger control volumes or “blocks”. This process can be performed recursively, as shown in Figure A-13, thus generating an entire sequence of coarse meshes.

In fact, agglomeration multi-grid can be viewed as a graph algorithm, similar to algebraic multi-grid methods, where “seed” cell initiating an agglomerated block corresponds to a coarse grid point and the neighboring agglomerated points correspond to fine grid points, in the algebraic multi-grid terminology. In the same ways that semi-coarsening algebraic multi-grid, the agglomeration multi- grid method can employ a weighted graph to fit its coarsening strategy to its smoother anisotropic capabilities. The underlying aim of these weights is to select first the error components poorly damped by the relaxation scheme on the finer grid.

MIGAL uses four parameters to control the agglomeration of the control volumes, *nbmin, nbmax, ilink* and *alpha*. The two former are respectively the minimum and maximum number of fine cells to group together in one coarse block. The two latter are the kind of linking criterion to apply and the relative threshold of this criterion. The overall algorithm proceeds as follows:

1. Select a seed cell among cells (free cells) which have not yet been assigned to a block. Start a new block agglomeration.
2. Build a list (front) with the free neighboring cells of the seed cell which satisfy the agglomeration criterion.
3. If the front is empty but the seed cell satisfies the agglomeration criterion with a cell of a neighboring block, and if the size of this block is lower than *nbmax*, then assign the seed cell to the block and return to step 1.

SOLVER	*NBGRID*	*IGMRES*	*IPRECO*	*IGMS*
ILU(0)	1	0	-	0
GMRES not-preconditioned	1	n	0	0
GMRES ILU(0) preconditioned	1	n	n	0
Multi-grid[ILU(0)]*	n	0	-	0
GMRES multi-grid[ILU(0)] preconditioned	n	n	n	0
Multi-grid[GMRES-ILU(0) preconditioned]	n	0	-	n
GMRES multi-grid[GMRES-ILU(0) preconditioned] preconditioned	n	n	n	n

Figure A-12. *Multi-grid/GMRES possible combinations. (*)=default*

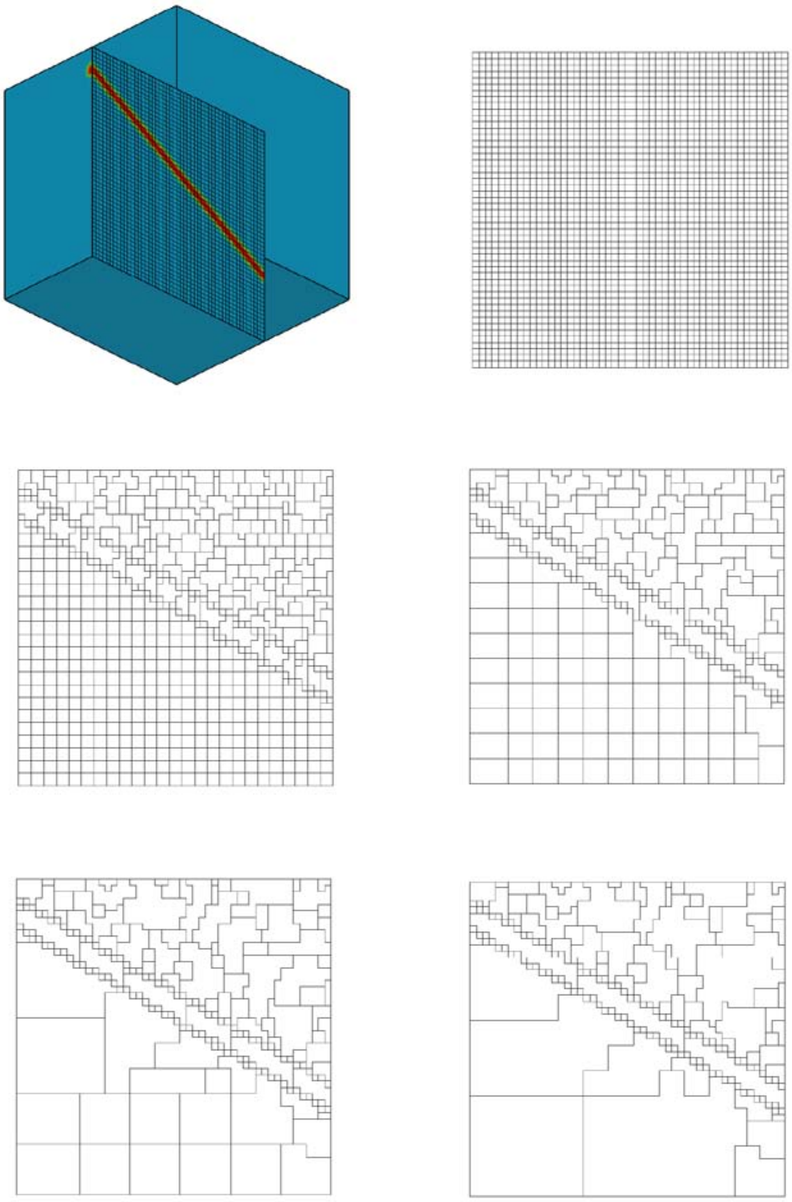

Figure A-13. Single fracture case.
Porosity, Original fine mesh and agglomerated levels (ilink=2, α=0.75).

4. Assign front cells to the current block unless its size reaches *nbmax* and propagate the front to the free neighboring cells satisfying the agglomeration criterion.
5. Perform an accretion step in order to make blocks as “rounded” as possible, rather than extended with connections to many other blocks. The accretion step adds to the current block those cells having two or more strong (as defined in step 2 above) connections to the block. Repeat this step until *nbmax* is reached or no more cells can be agglomerated this way.
6. If the total number of cells of the block is lower than *nbmin*, then repeat steps 4 and 5 until at least *nbmin* is reached.

Nbmin and *nbmax* default values are respectively the mean number of neighbors per cell and four times *nbmin*. For the few cases that would not perform well with this initial setting, reducing the minimum block size may improve the rate of convergence. For instance *nbmin=3* may be used for 3D isotropic cases in order get closer of the performance of the structured multi-grid solver.

A.9 Coarsening criterion

The coarsening algorithm should be able to handle arbitrary anisotropic meshes, but should also be able to reproduce structured-mesh semi-coarsening patterns for uniformly anisotropic problems on structured meshes. A simple-minded technique for graph-weighted coarsening would be to agglomerate the neighboring free cell which has the strongest connection to the current seed cell. The difficulty with this approach is that in regions where the anisotropic character is weak, the algorithm does not revert to the multi-directional coarsening strategy of the original algorithm. A more sophisticated approach is to pre-compute the maximum and/or the mean connection strength for each cell, and then agglomerate the free neighboring cell j to a block cell i only if:

(ilink=0) $|a_{ij}| > \alpha \max_{k\neq i}^{nb_i} |a_{ik}|$ OR $|a_{ji}| > \alpha \max_{k\neq j}^{nb_j} |a_{jk}|$

(ilink=1) $|a_{ij}| > \alpha \frac{1}{nb_i} \sum_{k\neq i}^{nb_i} |a_{ik}|$ OR $|a_{ji}| > \alpha \frac{1}{nb_j} \sum_{k\neq j}^{nb_j} |a_{jk}|$

(ilink=2) $|a_{ij}| > \alpha \max_{k\neq i}^{nb_i} |a_{ik}|$ AND $|a_{ji}| > \alpha \max_{k\neq j}^{nb_j} |a_{jk}|$

(ilink=3) $|a_{ij}| > \alpha \frac{1}{nb_i} \sum_{k\neq i}^{nb_i} |a_{ik}|$ AND $|a_{ji}| > \alpha \frac{1}{nb_j} \sum_{k\neq j}^{nb_j} |a_{jk}|$

Where nb_i and nb_j represent the number of connections of cells i and j, and α is a relative threshold which determines the degree of anisotropic coarsening. For $\alpha=0$ unweighted coarsening is recovered, while when $\alpha=1$ coarsening occurs only along stronger connections. MIGAL default values are *ilink=0* and $\alpha=0.75$ which reproduce directional coarsening in regions of strong anisotropies, and full or unweighted coarsening elsewhere.

Nevertheless, the choice of the coarsening criterion often depends on the relation between anisotropy and boundary conditions, and a user control is sometimes preferable. For example the AND rather and OR criterion alternative should be preferred for domain made of materials having very different conductivities see Figure A-14. In such a case ilink=2 or ilink=3 will clearly separate materials during coarsening while ilink=0 or ilink=1 allows agglomeration of heterogeneous cells.

It is important to note that, unlike coarsening criteria 0 and 1, the coarsening criteria 2 or 3 may lead to cells without strongly linked neighbor when $0<\alpha$. Hence during the recursive generation of coarse grid operators, MIGAL uses an extra parameter *(ratio)* to stop coarsening when the number of cells is not decreased by, at least, a factor of *ratio*:1. The default setting is *ratio=1.5.* It avoids the use of unnecessary coarse grids and, by limiting the total number of cells, decreases the overall CPU time per cycle.

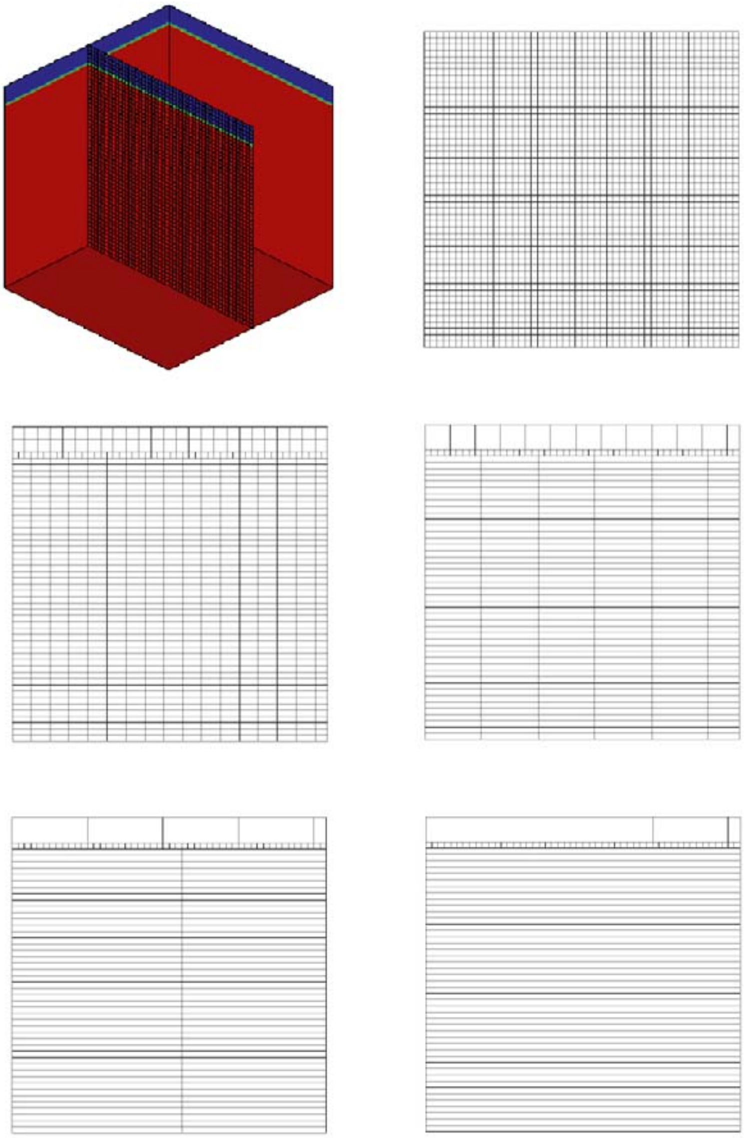

Figure A-14. *Strong anisotropy case.*
Porosity, Original fine mesh and agglomerated levels (ilink=2, a=0.75).

Appendix B

Some aspects of using the multirate model with a power law distribution of rates

Some aspects of using the multirate model with a power law distribution of rates

Hans-Olof Kuylenstierna

19th April 2002

1 Introduction

This paper deals with some aspects of using the multirate model of the immobile zone with a power law distribution of first-order rates. For an introduction to the subject, see Refs. 1 and 2. Sections 2, 3, 4 and 5 have a mathematical character and mainly discuss the relation between power law distributions for diffusion rates and first-order rates. The main conclusion is that the two power law distributions will have the same exponent if some conditions are fulfilled, a fact which was briefly mentioned in Ref. 2. Section 6 describes how the power law distribution for diffusion rate can be obtained starting from a power law distribution for fracture size and many other assumptions. Finally, Section 7 suggests how the theory presented in the earlier sections can be applied to computer simulations of tracer motion in fractured rock.

Many of the ideas in the paper originate from Refs. 1 and 2. Urban Svensson has contributed with basic ideas for Sections 6 and 7, while I have concentrated on mathematical issues.

2 The base of the model for the immobile zone

Consider a region of fractured rock. The fractures are filled with water (apart from possible solid material). A tracer is dissolved in the water at varying concentration. Water and tracer particles are subject to diffusion in the entire water-filled volume. Let the mobile zone be the part of the water-filled volume where also advection can occur. The mobile zone is assumed to be connected. (This means that a water or tracer particle anywhere in the zone can travel through the zone by means of advection or diffusion to any other location in the zone.) Let the immobile zone be the parts of the water-filled volume which do not belong to the mobile zone but which are accessible to particles in the mobile zone by means of diffusion. (There can also be parts of the water-filled volume which are inaccessible to water and tracer in the mobile zone, and which we shall not consider further.) The solid material surrounding both the mobile and immobile zones can adsorb tracer particles. Adsorbed particles are still regarded as being located in the respective zones.

Consider a volume of water belonging to the mobile or immobile zone. Assume that the concentration of tracer in the water is uniform in the volume and that the dissolved and adsorbed tracer are in equilibrium. Let us form the ratio of the amount of tracer, dissolved and adsorbed, to the concentration of tracer in the water. (If there is no adsorption, the ratio is equal to the volume of the water.) With the capacity of the volume I mean this ratio. (I hope I use the term correctly.)

The total capacity ratio β_{tot} is the ratio of the capacity of the immobile zone to the capacity of the mobile zone. When the mobile and immobile zones are in equilibrium, the ratio of the amount of tracer in the immobile zone to that in the mobile zone is equal to β_{tot}.

According to the multirate model described in Ref. 1, the immobile zone can be modelled as a continuous spectrum of first-order boxes. Each box is characterized by a first-order rate $\alpha > 0$, and the probability that a tracer particle in the box will leave the box and enter the mobile zone during a time interval dt is $\alpha\, dt$, regardless of the particle's history. The capacity ratio density function $b(\alpha) \geq 0$ specifies how the total capacity ratio β_{tot} is distributed over the spectrum of boxes. The capacity ratio for the boxes with rates in the interval $(\alpha, \alpha + d\alpha)$ is $b(\alpha)\, d\alpha$, and

$$\int_0^\infty b(\alpha)\, d\alpha = \beta_{\text{tot}}. \tag{1}$$

This means that when the mobile zone and all the first-order boxes are in equilibrium, the ratio of the amount of tracer in the boxes with rates in the interval $(\alpha, \alpha + d\alpha)$ to the amount of tracer in the mobile zone is $b(\alpha)\, d\alpha$. It is possible to conclude from this that if the tracer particles have an equilibrium distribution within the mobile zone, the probability that a randomly chosen particle in the mobile zone will enter any of the boxes with rates in the interval $(\alpha, \alpha + d\alpha)$ during a time interval dt is $b(\alpha)\, d\alpha\, \alpha\, dt$, regardless of whether the mobile zone is in equilibrium with the first-order boxes.

It may seem natural to divide the immobile zone into a spectrum of parts characterized by their sizes. (This could be done if we modelled the immobile zone as a collection of square fractures extending perpendicularly from the mobile zone, for example.) We shall however use a characteristic diffusion rate $\alpha_{\text{d}} > 0$ instead of the size as the characterizing variable in the spectrum. (It is usual to assume that there is a simple relationship between size and diffusion rate, as we will do in Section 6 using Formula 37.) Let us introduce the capacity ratio density function $b_{\text{d}}(\alpha_{\text{d}}) \geq 0$ to specify the distribution of the total capacity ratio β_{tot} over the new spectrum. I.e., the capacity ratio for the parts of the immobile zone whose diffusion rates belong to the interval $(\alpha_\mathrm{d}, \alpha_\mathrm{d} + d\alpha_\mathrm{d})$ is $b_\mathrm{d}(\alpha_\mathrm{d})\, d\alpha_\mathrm{d}$, and

$$\int_0^\infty b_\mathrm{d}(\alpha_\mathrm{d})\, d\alpha_\mathrm{d} = \beta_\mathrm{tot}. \tag{2}$$

For fixed diffusion rate α_d, let us model the corresponding part of the immobile zone with a multirate model specified by $b_{\mathrm{fo}|\mathrm{d}}(\alpha \mid \alpha_\mathrm{d}) \geq 0$ ("fo" for "first order"), where

$$\int_0^\infty b_{\mathrm{fo}|\mathrm{d}}(\alpha \mid \alpha_\mathrm{d})\, d\alpha = 1. \tag{3}$$

The multirate model for the entire immobile zone (all α_d) will then be specified by

$$b(\alpha) = \int_0^\infty b_{\mathrm{fo}|\mathrm{d}}(\alpha \mid \alpha_\mathrm{d}) b_\mathrm{d}(\alpha_\mathrm{d})\, d\alpha_\mathrm{d}. \tag{4}$$

(Some of the terminology and notation in this section is inspired by probability theory.)

3 A power law distribution for the diffusion rate

In Ref. 2 a power law distribution for the diffusion rate α_d is suggested (among a few other distributions). Power law distributions occur in connection with fractals and are therefore theoretically attractive. The distribution is given by the formula

$$b_\mathrm{d}(\alpha_\mathrm{d}) = \begin{cases} \dfrac{\beta_\mathrm{tot}}{I(\alpha_{\mathrm{d,min}}, \alpha_{\mathrm{d,max}}, k-2)} \alpha_\mathrm{d}^{k-3}, & \alpha_{\mathrm{d,min}} < \alpha_\mathrm{d} < \alpha_{\mathrm{d,max}}, \\ 0 & \text{otherwise}, \end{cases} \tag{5}$$

where

$$I(x_\mathrm{min}, x_\mathrm{max}, p) = \int_{x_\mathrm{min}}^{x_\mathrm{max}} x^{p-1}\, dx = \begin{cases} \ln \dfrac{x_\mathrm{max}}{x_\mathrm{min}}, & p = 0, \\ \dfrac{x_\mathrm{max}^p - x_\mathrm{min}^p}{p}, & p \neq 0. \end{cases} \tag{6}$$

The exponent $k - 3$ has been chosen in conformance with Formula (27a) in Ref. 2.

4 Multirate models for fixed diffusion rate

In this section we shall study multirate models for the part of the immobile zone corresponding to a fixed diffusion rate α_{d}. In other words, we shall study $b_{\mathrm{fo|d}}(\alpha \mid \alpha_{\mathrm{d}})$.

$b_{\mathrm{fo|d}}(\alpha \mid \alpha_{\mathrm{d}})$ may or may not have properties P_1 and $P_2(k)$, which are defined as follows. k is a given real number.

P_1: There exists a function $f(\xi)$ such that

$$b_{\mathrm{fo|d}}(\alpha \mid \alpha_{\mathrm{d}}) = \frac{f(\alpha/\alpha_{\mathrm{d}})}{\alpha_{\mathrm{d}}} \tag{7}$$

for all α_{d} and α.

$P_2(k)$: The integral

$$\int_0^\infty f(\xi)\xi^{2-k}\,d\xi, \quad k \neq 2, \tag{8}$$

or the integral

$$\int_0^\infty f(\xi)\ln\xi\,d\xi, \quad k = 2, \tag{9}$$

converges at both 0 and ∞. (There is thus a different variant of this condition for each of the cases $k \neq 2$ and $k = 2$.)

If $b_{\mathrm{fo|d}}(\alpha \mid \alpha_{\mathrm{d}})$ has property P_1, the function $f(\xi)$ is uniquely determined. It is defined for all $\xi > 0$, $f(\xi) \geq 0$ for all $\xi > 0$, and

$$\int_0^\infty f(\xi)\,d\xi = 1. \tag{10}$$

Therefore, if $k = 2$, the integral in Formula 8 will converge. If $b_{\mathrm{fo|d}}(\alpha \mid \alpha_{\mathrm{d}})$ has properties P_1 and $P_2(k)$, let us define

$$\xi_{\mathrm{mean}}(k) = \begin{cases} \left(\int_0^\infty f(\xi)\xi^{2-k}\,d\xi\right)^{1/(2-k)}, & k \neq 2, \\ \exp\int_0^\infty f(\xi)\ln\xi\,d\xi, & k = 2. \end{cases} \tag{11}$$

The definitions etc. in this paragraph will be used in Section 5.

We shall now study three kinds of immobile zones, in order to get examples of what $b_{\mathrm{fo|d}}(\alpha \mid \alpha_{\mathrm{d}})$ can look like.

Consider a narrow and thin fracture which extends straightly a distance a from the mobile zone into the surrounding material. Let us assume that the fracture has constant cross-section area along its entire length. If there is any solid material in the fracture, it is assumed to be homogeneously distributed. Let D_{a} be the apparent diffusivity for tracer particles in the fracture. Let us choose the ratio D_{a}/a^2 as the characteristic diffusion rate α_{d} of the fracture. Let us assume that the immobile zone consists entirely of such fractures. The fractures may have different a and D_{a} values and therefore different α_{d} values. The part of the immobile zone consisting of fractures with a given α_{d} value then has the multirate model specified by

$$b_{\mathrm{fo|d}}(\alpha \mid \alpha_{\mathrm{d}}) = \sum_{j=1}^{\infty} \frac{8}{(2j-1)^2\pi^2} \delta\left(\alpha - \frac{(2j-1)^2\pi^2}{4}\alpha_{\mathrm{d}}\right), \tag{12}$$

where δ is the Dirac delta function. Immobile zone diffusion to which this formula applies is called layered diffusion (in finite layers).

If the cross-section area of a fracture is not constant along the fracture's length but proportional to the distance to the dead end of the fracture (i.e., the end which is not in contact with the mobile zone), then the term cylindrical diffusion is used, and the multirate model is specified by

$$b_{\mathrm{fo|d}}(\alpha \mid \alpha_{\mathrm{d}}) = \sum_{j=1}^{\infty} \frac{4}{u_j^2} \delta(\alpha - u_j^2 \alpha_{\mathrm{d}}). \tag{13}$$

u_j here denotes the jth solution of $J_0(u_j) = 0$, where J_0 is a Bessel function of the first kind. It should be noted that $u_{j+1} - u_j \approx \pi$ for large j.

If the cross-section area is proportional to the square of the distance to the dead end, the term spherical diffusion is used, and the formula is

$$b_{\mathrm{fo|d}}(\alpha \mid \alpha_{\mathrm{d}}) = \sum_{j=1}^{\infty} \frac{6}{j^2\pi^2} \delta(\alpha - j^2\pi^2\alpha_{\mathrm{d}}). \tag{14}$$

Formulas 12, 13 and 14 have been taken from Table 1 in Ref. 2, although the notation has been changed somewhat.

We shall now investigate how the formulas for layered, cylindrical and spherical diffusion are related to properties P_1 and $P_2(k)$.

It is rather easy to show that the three formulas all have property P_1. Therefore to each formula there is a corresponding function $f(\xi)$. For each formula, $f(\xi) = 0$ for small ξ, and therefore the integrals in Formulas 8 and 9 converge at 0 for all k. Moreover, $f(\xi) = O(\xi^{-3/2})$ on average (loosely speaking) for large ξ, and therefore the two integrals converge at ∞ for all $k > 3/2$. Thus, the three formulas all have property $P_2(k)$ for all $k > 3/2$.

Property P_1 means that $b_{\mathrm{fo|d}}(\alpha \mid \alpha_{\mathrm{d}})$, when viewed as a function of α, is equal for all α_{d} except for stretching and contraction. P_1 therefore indicates some kind of scale-invariance with respect to α_{d}. Small ξ correspond to low first-order rates α and therefore to slow first-order boxes, i.e. boxes where particles stay for a long time on average once they have entered. For fixed α_{d}

the immobile zone fractures in the three diffusion models have finite length, or more precisely, they have a fixed D_a/a^2 ratio, and therefore it is natural that there is a limit to how slow first-order boxes there are, or equivalently, that $f(\xi) = 0$ for small ξ. Large ξ, on the other hand, correspond to high rates α and fast first-order boxes. $f(\xi)$'s $O(\xi^{-3/2})$ behaviour for large ξ is common to the three diffusion models, although the shapes of the fractures vary between the models. Fast boxes in the multirate model mostly have to do with particles that leave the immobile zone fractures soon after they have entered them, probably not diffusing far into the fractures. The fractures do not vary much in cross-section area in the parts nearest to the mobile zone, and therefore it is perhaps natural that all three diffusion models exhibit the same $O(\xi^{-3/2})$ behaviour for large ξ.

From the discussion in the previous two paragraphs we can draw the following conclusions. Consider the class of diffusion models where $b_{\mathrm{fo|d}}(\alpha \mid \alpha_{\mathrm{d}})$ has properties P_1 and $P_2(k)$ for $k > 3/2$. The models for layered, cylindrical and spherical diffusion belong to this class. The three models are probably members of a rather large group of diffusion models which seem to be realistic from a mathematical point of view and which belong to the class.

5 The multirate model for the entire immobile zone

There are two ways to obtain $b(\alpha)$, which specifies the multirate model for the entire immobile zone. The first way is to choose some suitable $b(\alpha)$ without consideration of $b_{\mathrm{d}}(\alpha_{\mathrm{d}})$ and $b_{\mathrm{fo|d}}(\alpha \mid \alpha_{\mathrm{d}})$. The second way is to choose $b_{\mathrm{d}}(\alpha_{\mathrm{d}})$ and $b_{\mathrm{fo|d}}(\alpha \mid \alpha_{\mathrm{d}})$ first and then use Formula 4 to calculate $b(\alpha)$.

When $b(\alpha)$ is obtained the first way, a power law distribution is a possible choice, as suggested in Ref. 2. $b(\alpha)$ will then be given by the formula

$$b(\alpha) = \begin{cases} \dfrac{\beta_{\mathrm{tot}}}{I(\alpha_{\mathrm{min}}, \alpha_{\mathrm{max}}, k-2)} \alpha^{k-3}, & \alpha_{\mathrm{min}} < \alpha < \alpha_{\mathrm{max}}, \\ 0 & \text{otherwise.} \end{cases} \tag{15}$$

Note the similarity to Formula 5.

We shall now see what $b(\alpha)$ will look like when it is obtained the second way, provided that certain conditions are fulfilled.

We shall assume that $b_{\mathrm{d}}(\alpha_{\mathrm{d}})$ is given by Formula 5 and that $b_{\mathrm{fo|d}}(\alpha \mid \alpha_{\mathrm{d}})$ has properties P_1 and $P_2(k)$ as defined in Section 4. The k in $P_2(k)$ shall be the same as in Formula 5. Using Formulas 4 and 5 and property P_1 we get

$$\begin{aligned}
b(\alpha) &= \int_0^\infty b_{\mathrm{fo|d}}(\alpha \mid \alpha_{\mathrm{d}}) b_{\mathrm{d}}(\alpha_{\mathrm{d}})\, d\alpha_{\mathrm{d}} \\
&= \int_{\alpha_{\mathrm{d,min}}}^{\alpha_{\mathrm{d,max}}} \frac{f(\alpha/\alpha_{\mathrm{d}})}{\alpha_{\mathrm{d}}} \frac{\beta_{\mathrm{tot}}}{I(\alpha_{\mathrm{d,min}}, \alpha_{\mathrm{d,max}}, k-2)} \alpha_{\mathrm{d}}^{k-3}\, d\alpha_{\mathrm{d}} \\
&= \left[\xi = \frac{\alpha}{\alpha_{\mathrm{d}}},\quad \alpha_{\mathrm{d}} = \frac{\alpha}{\xi},\quad d\alpha_{\mathrm{d}} = -\frac{\alpha\, d\xi}{\xi^2}\right] \\
&= \int_{\alpha/\alpha_{\mathrm{d,min}}}^{\alpha/\alpha_{\mathrm{d,max}}} \frac{f(\xi)}{\alpha/\xi} \frac{\beta_{\mathrm{tot}}}{I(\alpha_{\mathrm{d,min}}, \alpha_{\mathrm{d,max}}, k-2)} \left(\frac{\alpha}{\xi}\right)^{k-3} \left(-\frac{\alpha\, d\xi}{\xi^2}\right) \\
&= \frac{\beta_{\mathrm{tot}}}{I(\alpha_{\mathrm{d,min}}, \alpha_{\mathrm{d,max}}, k-2)} \alpha^{k-3} \int_{\alpha/\alpha_{\mathrm{d,max}}}^{\alpha/\alpha_{\mathrm{d,min}}} f(\xi)\xi^{2-k}\, d\xi. \qquad (16)
\end{aligned}$$

Had the integral in the last term not been dependent on α, $b(\alpha)$ would have been proportional to α^{k-3}. Let us therefore study the integral more closely.

Let $\epsilon > 0$ be some small number. Property $P_2(k)$ implies that there are numbers ξ_{min} and ξ_{max} with $0 < \xi_{\mathrm{min}} \le \xi_{\mathrm{max}}$ such that

$$\int_0^{\xi'} f(\xi)\xi^{2-k}\, d\xi < \epsilon \int_0^\infty f(\xi)\xi^{2-k}\, d\xi \qquad (17)$$

for all ξ' with $0 < \xi' < \xi_{\mathrm{min}}$ and

$$\int_{\xi'}^\infty f(\xi)\xi^{2-k}\, d\xi < \epsilon \int_0^\infty f(\xi)\xi^{2-k}\, d\xi \qquad (18)$$

for all $\xi' > \xi_{\mathrm{max}}$. If also $\xi_{\mathrm{max}}\alpha_{\mathrm{d,min}} < \xi_{\mathrm{min}}\alpha_{\mathrm{d,max}}$, then

$$\frac{\displaystyle\int_{\alpha/\alpha_{\mathrm{d,max}}}^{\alpha/\alpha_{\mathrm{d,min}}} f(\xi)\xi^{2-k}\, d\xi}{\displaystyle\int_0^\infty f(\xi)\xi^{2-k}\, d\xi} \in \begin{cases} [0,\epsilon), & 0 < \alpha < \xi_{\mathrm{min}}\alpha_{\mathrm{d,min}}, \\ [0,1], & \xi_{\mathrm{min}}\alpha_{\mathrm{d,min}} \le \alpha \le \xi_{\mathrm{max}}\alpha_{\mathrm{d,min}}, \\ (1-2\epsilon, 1], & \xi_{\mathrm{max}}\alpha_{\mathrm{d,min}} < \alpha < \xi_{\mathrm{min}}\alpha_{\mathrm{d,max}}, \\ [0,1], & \xi_{\mathrm{min}}\alpha_{\mathrm{d,max}} \le \alpha \le \xi_{\mathrm{max}}\alpha_{\mathrm{d,max}}, \\ [0,\epsilon), & \xi_{\mathrm{max}}\alpha_{\mathrm{d,max}} < \alpha. \end{cases} \qquad (19)$$

This formula suggests that the numerator integral could be approximated by a function which is equal to the denominator integral when α belongs to some interval and equal to 0 outside the interval.

Let us assume that ξ_{min} and ξ_{max} can be chosen so that they satisfy the following two conditions in addition to those already given. ξ_{min} and ξ_{max} shall not be too far apart, in order that the intervals $\xi_{\mathrm{min}}\alpha_{\mathrm{d,min}} \le \alpha \le$

$\xi_{\max}\alpha_{\mathrm{d,min}}$ and $\xi_{\min}\alpha_{\mathrm{d,max}} \le \alpha \le \xi_{\max}\alpha_{\mathrm{d,max}}$ in Formula 19 shall not be too wide. The relation $\xi_{\min} \le \xi_{\mathrm{mean}}(k) \le \xi_{\max}$ shall hold, where $\xi_{\mathrm{mean}}(k)$ was defined by Formula 11. If such $\xi_{\min}$ and $\xi_{\max}$ can be found, then the numerator integral can be approximated as described with the interval being $\xi_{\mathrm{mean}}(k)\alpha_{\mathrm{d,min}} < \alpha < \xi_{\mathrm{mean}}(k)\alpha_{\mathrm{d,max}}$. $b(\alpha)$ can consequently be approximated by the function

$$b_{\mathrm{appr}}(\alpha) = \begin{cases} \dfrac{\beta_{\mathrm{tot}}}{I(\alpha_{\mathrm{d,min}}, \alpha_{\mathrm{d,max}}, k-2)}\alpha^{k-3}\displaystyle\int_0^\infty f(\xi)\xi^{2-k}\,d\xi, \\ \qquad\qquad \xi_{\mathrm{mean}}(k)\alpha_{\mathrm{d,min}} < \alpha < \xi_{\mathrm{mean}}(k)\alpha_{\mathrm{d,max}}, \\ 0 \qquad\qquad \text{otherwise}, \end{cases} \tag{20}$$

which thanks to the definition of $\xi_{\mathrm{mean}}(k)$ can also be written

$$b_{\mathrm{appr}}(\alpha) = \begin{cases} \dfrac{\beta_{\mathrm{tot}}}{I(\xi_{\mathrm{mean}}(k)\alpha_{\mathrm{d,min}}, \xi_{\mathrm{mean}}(k)\alpha_{\mathrm{d,max}}, k-2)}\alpha^{k-3}, \\ \qquad\qquad \xi_{\mathrm{mean}}(k)\alpha_{\mathrm{d,min}} < \alpha < \xi_{\mathrm{mean}}(k)\alpha_{\mathrm{d,max}}, \\ 0 \qquad\qquad \text{otherwise}. \end{cases} \tag{21}$$

This choice of $b_{\mathrm{appr}}(\alpha)$ has the advantages that the intervals in Formulas 5 and 21 are equally wide in a logarithmic sense and that

$$\int_0^\infty b_{\mathrm{appr}}(\alpha)\,d\alpha = \int_0^\infty b(\alpha)\,d\alpha = \beta_{\mathrm{tot}}. \tag{22}$$

Note the similarity between Formulas 5, 15 and 21.

The definition of $\xi_{\mathrm{mean}}(k)$ in Formula 11, case $k \neq 2$, was chosen in order that Formula 22 should hold. When $k = 2$, Formula 22 would hold regardless of the value of $\xi_{\mathrm{mean}}(k)$. The definition of $\xi_{\mathrm{mean}}(k)$ in Formula 11, case $k = 2$, was chosen because

$$\lim_{k\to 2}\left(\int_0^\infty f(\xi)\xi^{2-k}\,d\xi\right)^{1/(2-k)} = \exp\int_0^\infty f(\xi)\ln\xi\,d\xi. \tag{23}$$

Let us summarize our results about the second way of obtaining $b(\alpha)$ as follows. Assume that $b(\alpha)$ is calculated from $b_{\mathrm{d}}(\alpha_{\mathrm{d}})$ and $b_{\mathrm{fo|d}}(\alpha \mid \alpha_{\mathrm{d}})$ using Formula 4. Assume that $b_{\mathrm{d}}(\alpha_{\mathrm{d}})$ is given by Formula 5 and that $b_{\mathrm{fo|d}}(\alpha \mid \alpha_{\mathrm{d}})$ has properties P_1 and $P_2(k)$, where k is the same as in Formula 5. Let $\xi_{\mathrm{mean}}(k)$ be defined by Formula 11. Let $\epsilon > 0$ be some suitably small number. Assume that $\xi_{\min}$ and $\xi_{\max}$ can be chosen so that they are not too far apart and satisfy the conditions $0 < \xi_{\min} \le \xi_{\mathrm{mean}}(k) \le \xi_{\max}$ and $\xi_{\max}\alpha_{\mathrm{d,min}} < \xi_{\min}\alpha_{\mathrm{d,max}}$ as well as the condition stated using Formulas 17 and 18. Then

$$b(\alpha) = \frac{\beta_{\mathrm{tot}}}{I(\alpha_{\mathrm{d,min}}, \alpha_{\mathrm{d,max}}, k-2)}\alpha^{k-3}\int_{\alpha/\alpha_{\mathrm{d,max}}}^{\alpha/\alpha_{\mathrm{d,min}}} f(\xi)\xi^{2-k}\,d\xi, \tag{24}$$

where the integral satisfies Formula 19. Moreover, $b(\alpha)$ can be approximated by the function

$$b_{\text{appr}}(\alpha) = \begin{cases} \dfrac{\beta_{\text{tot}}}{I(\xi_{\text{mean}}(k)\alpha_{\text{d,min}}, \xi_{\text{mean}}(k)\alpha_{\text{d,max}}, k-2)} \alpha^{k-3}, \\ \qquad\qquad \xi_{\text{mean}}(k)\alpha_{\text{d,min}} < \alpha < \xi_{\text{mean}}(k)\alpha_{\text{d,max}}, \\ 0 \qquad\qquad \text{otherwise}, \end{cases} \tag{25}$$

where $b_{\text{appr}}(\alpha)$ satisfies Formula 22.

6 A derivation of the power law distribution for diffusion rate from fracture properties

In this section we shall see how the power law distribution for diffusion rate, as given by Formula 5, can be obtained starting from a power law distribution for fracture size and other assumptions. There are many assumptions made in this section, and some of them are perhaps not realistic.

We assume that fractures are randomly and homogeneously distributed in the solid material surrounding the mobile zone. We assume that a length scale a can in some manner be associated with each fracture. The number d^2N of fractures with centres within a volume dV of surrounding material and with length scales in the interval $(a, a + da)$ is assumed to satisfy the power law formula

$$d^2N \begin{cases} \propto a^{-D_f-1}\, da\, dV, & a_{\min} < a < a_{\max}, \\ = 0 & \text{otherwise}, \end{cases} \tag{26}$$

where "$\propto$" denotes proportionality. (Regarding the designation D_f see the end of this section.)

It is reasonable to assume that a fracture intersects the mobile zone if the distance from the centre of the fracture to the mobile zone is in the order of a or less. The number d^2N_{im} of fractures intersecting an area dA_{m} of the mobile zone and with length scales in the interval $(a, a + da)$ is therefore assumed to satisfy

$$d^2N_{\text{im}} \propto a^{-D_f-1}\, da\, a\, dA_{\text{m}} = a^{-D_f}\, da\, dA_{\text{m}}. \tag{27}$$

(From now on, we do not mention the condition $a_{\min} < a < a_{\max}$ explicitly.)

To simplify the discussion we shall assume that the fractures in the material surrounding the mobile zone are not in direct contact with each other. (However, those of the fractures which intersect the mobile zone are in indirect contact with each other via the zone.) We shall also assume that fractures which intersect the mobile zone and which have the same length scale a have equal properties in other respects too.

In a fracture intersecting the mobile zone, let the immobile zone volume denote the volume of water in the fracture which is accessible to water and tracer in the mobile zone. The immobile zone is formed by the immobile zone volumes of all the fractures intersecting the mobile zone.

Consider the assumption that the volume of a fracture intersecting the mobile zone is proportional to $a^{\gamma+2}$. This should be the case if the length, width and thickness of the fracture were proportional to a, a and a^{γ}, respectively. We shall however instead assume that the capacity of the immobile zone volume of the fracture is proportional to $a^{\gamma+2}$. This assumption is perhaps less realistic, but it is necessary if we want to arrive at a power law distribution for the diffusion rate. Consider again the fractures intersecting the area dA_{m} of the mobile zone and with length scales in the interval $(a, a+da)$. It follows from our assumption (and from Formula 27) that the capacity $R_{\mathrm{im}}\,d^2V_{\mathrm{im}}$ of the immobile zone volume of these fractures satisfies

$$R_{\mathrm{im}}\,d^2V_{\mathrm{im}} \propto a^{\gamma+2}a^{-D_{\mathrm{f}}}\,da\,dA_{\mathrm{m}} = a^{\gamma-D_{\mathrm{f}}+2}\,da\,dA_{\mathrm{m}}. \tag{28}$$

(R_{im} and d^2V_{im} are explained in the following paragraph.)

Let R_{m} and $R_{\mathrm{im,tot}}$ be the retardation factors for the mobile and immobile zones, respectively. The retardation factor for a zone specifies the ratio of the total amount of tracer (both dissolved and adsorbed) to the amount of dissolved tracer in the zone at equilibrium. Let dV_{m} be the volume of the mobile zone corresponding to the area dA_{m}. $dA_{\mathrm{m}}/dV_{\mathrm{m}}$ is thus the area-to-volume ratio of the mobile zone. Let dV_{im} be the volume of the immobile zone in contact with the area dA_{m} of the mobile zone. The capacities of the two volumes can be expressed as $R_{\mathrm{m}}\,dV_{\mathrm{m}}$ and $R_{\mathrm{im,tot}}\,dV_{\mathrm{im}}$, which leads to the formula

$$\beta_{\mathrm{tot}} = \frac{R_{\mathrm{im,tot}}\,dV_{\mathrm{im}}}{R_{\mathrm{m}}\,dV_{\mathrm{m}}}. \tag{29}$$

The analogous formula for the part of the immobile zone with length scales in the interval $(a, a+da)$ is

$$b_a(a)\,da = \frac{R_{\mathrm{im}}\,d^2V_{\mathrm{im}}}{R_{\mathrm{m}}\,dV_{\mathrm{m}}}, \tag{30}$$

where R_{im} may depend on a. We have here introduced the capacity ratio density function $b_a(a)$, which specifies how the total capacity ratio β_{tot} is distributed over the spectrum of length scales a. As usual,

$$\int_0^{\infty} b_a(a)\,da = \beta_{\mathrm{tot}}. \tag{31}$$

Multiplication of Formulas 28 and 30 yields

$$b_a(a) \propto \frac{dA_{\mathrm{m}}}{R_{\mathrm{m}}\,dV_{\mathrm{m}}}a^{\gamma-D_{\mathrm{f}}+2}. \tag{32}$$

10

From Formulas 31 and 32 we get

$$\beta_{\mathrm{tot}} \propto \frac{dA_{\mathrm{m}}}{R_{\mathrm{m}}\, dV_{\mathrm{m}}} \tag{33}$$

and

$$b_a(a) = \begin{cases} \dfrac{\beta_{\mathrm{tot}}}{I(a_{\mathrm{min}}, a_{\mathrm{max}}, \gamma - D_{\mathrm{f}} + 3)} a^{\gamma - D_{\mathrm{f}} + 2}, & a_{\mathrm{min}} < a < a_{\mathrm{max}}, \\ 0 & \text{otherwise}, \end{cases} \tag{34}$$

where we have taken the condition $a_{\mathrm{min}} < a < a_{\mathrm{max}}$ in Formula 26 into account.

We shall now set up a relation between a and the diffusion rate α_{d} (Formula 37), and using this relation we shall transform Formula 34 into the sought formula for the diffusion rate distribution $b_{\mathrm{d}}(\alpha_{\mathrm{d}})$ (Formula 39).

As in Section 4 and in Ref. 2 we shall use the relation

$$\alpha_{\mathrm{d}} \propto \frac{D_{\mathrm{a}}}{a^2}, \tag{35}$$

where D_{a} is the apparent diffusivity in a fracture of the immobile zone. We shall also assume that

$$D_{\mathrm{a}} \propto a^{\Psi}. \tag{36}$$

Combining these two formulas yields

$$\alpha_{\mathrm{d}} \propto a^{\Psi - 2}. \tag{37}$$

We also have the relation

$$b_{\mathrm{d}}(\alpha_{\mathrm{d}})|d\alpha_{\mathrm{d}}| = b_a(a)|da|, \tag{38}$$

as both sides express the same capacity ratio in different ways. (Absolute values have been taken since $d\alpha_{\mathrm{d}}$ and da may have equal or opposite signs depending on Ψ.) With routine calculations, where Formulas 37 and 38 are used, we can transform Formula 34 into

$$b_{\mathrm{d}}(\alpha_{\mathrm{d}}) = \begin{cases} \dfrac{\beta_{\mathrm{tot}}}{I(\alpha_{\mathrm{d,min}}, \alpha_{\mathrm{d,max}}, k - 2)} \alpha_{\mathrm{d}}^{k-3}, & \alpha_{\mathrm{d,min}} < \alpha_{\mathrm{d}} < \alpha_{\mathrm{d,max}}, \\ 0 & \text{otherwise}, \end{cases} \tag{39}$$

where

$$\frac{\alpha_{\mathrm{d,max}}}{\alpha_{\mathrm{d,min}}} = \left(\frac{a_{\mathrm{max}}}{a_{\mathrm{min}}} \right)^{|2 - \Psi|} \tag{40}$$

(the exact values of $\alpha_{\mathrm{d,min}}$ and $\alpha_{\mathrm{d,max}}$ depend on the implicit proportionality constant in Formula 37),

$$k = \frac{D_\mathrm{f} - \gamma - 2\Psi + 1}{2 - \Psi}, \tag{41}$$

and (from Formula 33)

$$\beta_\mathrm{tot} \propto \frac{dA_\mathrm{m}}{R_\mathrm{m}\, dV_\mathrm{m}}. \tag{42}$$

As Formula 39 is the same as Formula 5, we have now reached our goal to derive Formula 5 from our assumptions. Formulas 40, 41 and 42 can be used to calculate the parameters in Formula 5.

(In Ref. 3, Sections 3.1 and 5.7.2, and Ref. 4, Section 2.2.1, the designations D_f and D are used, respectively, and they are said to denote fractal dimension. Let us neglect fracture thickness in the present section's model of the fractures in the material surrounding the mobile zone, so that the fractures are regarded as surfaces with area proportional to a^2. I believe that the use of D_f in this model is then similar to the use of D_f and D in Refs. 3 and 4. Probably there exist one or more exact definitions of the concept fractal dimension in the mathematical literature. I am not sure whether the use of D_f and D in the present section and Refs. 3 and 4 is in accord with those definitions.)

7 Practical use of the multirate model in computer simulations of tracer motion

In this section it will be discussed how the multirate model with a power law distribution can be included in computer simulations of tracer motion in fractured rock.

We assume that the domain of rock where tracer motion is to be simulated is divided into cells by a computational grid, as is usual in numerical calculations. We further assume that the domain can be divided into a number of subdomains, each consisting of a group of cells. The properties of the immobile zone are assumed to be similar in cells which belong to the same subdomain. What is meant by this similarity will be specified further on.

Section 2 starts, "consider a region of fractured rock". This region is the setting for all of Sections 2, 3, 4 and 5. In connection with the concepts introduced in the previous paragraph, it is suitable to assume that the region refers to any one of the cells. If we look at Section 2, β_tot, $b(\alpha)$, $b_\mathrm{d}(\alpha_\mathrm{d})$ and $b_{\mathrm{fo|d}}(\alpha \mid \alpha_\mathrm{d})$ then all refer to this cell. If we consider the entire domain, there is one β_tot, one $b(\alpha)$, one $b_\mathrm{d}(\alpha_\mathrm{d})$ and one $b_{\mathrm{fo|d}}(\alpha \mid \alpha_\mathrm{d})$ for each cell. However, as we have assumed that the cells of a subdomain have similar immobile zone properties, we shall assume that $b_{\mathrm{fo|d}}(\alpha \mid \alpha_\mathrm{d})$ is equal in all cells of the subdomain, while $b(\alpha)$ and $b_\mathrm{d}(\alpha_\mathrm{d})$ are proportional to β_tot within the subdomain. In other words, each of the three functions $b(\alpha)/\beta_\mathrm{tot}$, $b_\mathrm{d}(\alpha_\mathrm{d})/\beta_\mathrm{tot}$ and $b_\mathrm{fo|d}(\alpha \mid \alpha_\mathrm{d})$ is equal for all cells in a subdomain but may vary between subdomains. In Section 3, $\alpha_\mathrm{d,min}$, $\alpha_\mathrm{d,max}$ and k are assumed to be constant within a subdomain, while β_tot and $b_\mathrm{d}(\alpha_\mathrm{d})$ may vary between cells. It follows from Formula 5 that $b_\mathrm{d}(\alpha_\mathrm{d})$ is proportional to β_tot within the subdomain. Regarding Section 4 it is sufficient to say that $b_\mathrm{fo|d}(\alpha \mid \alpha_\mathrm{d})$ is assumed not to vary between the cells of a subdomain. In Section 5 two ways to obtain $b(\alpha)$ are discussed. In the paragraph about the first way, α_min, α_max and k are assumed to be constant and $b(\alpha)$ proportional to β_tot within a subdomain. What has been said above about Sections 3 and 4 is true also for the part of Section 5 discussing the second way.

Section 6 can also be read with the domain, subdomains and cells in mind. a_min, a_max, $\alpha_\mathrm{d,min}$, $\alpha_\mathrm{d,max}$, D_f, γ, Ψ, k and $R_\mathrm{im,tot}$ should then be assumed to be constant within each subdomain. R_im and D_a may vary with a, but for fixed a they should be constant within a subdomain. The implicit proportionality constants in all the proportionality relations (i.e., formulas including "$\propto$") in the section are also assumed to be constant within each subdomain. The number of fractures d^2N_im, the area dA_m and the volumes dV_m, dV_im and d^2V_im are assumed to refer to any one cell and may vary between cells. dA_m is the area of the part of the mobile zone which belongs to the cell, for example. (However, it is better to assume that dV and d^2N in Formula 26 refer to an arbitrary volume within a subdomain.) R_m, β_tot, $b_a(a)$ and $b_\mathrm{d}(\alpha_\mathrm{d})$ are also assumed to refer to a cell and may vary between cells. Formulas 34 and 39 show that $b_a(a)$ and $b_\mathrm{d}(\alpha_\mathrm{d})$ are proportional to β_tot within a subdomain.

We shall now discuss possible ways to choose a multirate model for inclusion in computer simulations of tracer motion.

The task amounts to choosing a function $b(\alpha)$ for each cell. We shall treat each subdomain separately, so let us focus on one subdomain. Let us decide that each $b(\alpha)$ shall be of the form given in Formula 15. As has already been said, α_min, α_max and k are assumed to be constant within the subdomain while β_tot may vary from cell to cell. The remaining problem is to choose these parameters. When doing this it is possible to use more or less of the theory presented in this paper. If as much as possible of the theory is to be used, we can proceed as follows.

Following Section 6, we assume that dA_m, dV_m and R_m are somehow known for each cell in the subdomain. β_tot can then be calculated for each cell using Formula 42, provided that we can somehow choose the implicit proportionality constant. (If dA_m and dV_m are known for each cell, a possible way to calculate R_m is to use the relation $(R_\mathrm{m} - 1)\, dV_\mathrm{m} \propto dA_\mathrm{m}$.) Let us also assume that the constants a_min, a_max, D_f, γ and Ψ are known, as well as the implicit proportionality constant in Formula 37. $\alpha_\mathrm{d,min}$ and $\alpha_\mathrm{d,max}$ can then be calculated using Formula 37, and k using Formula 41. $b_\mathrm{d}(\alpha_\mathrm{d})$

for each cell will then be given by Formula 39 or Formula 5.

Following Section 4, we must choose $b_{\text{fo|d}}(\alpha \mid \alpha_{\text{d}})$, which should be the same for all cells in the subdomain. $b_{\text{fo|d}}(\alpha \mid \alpha_{\text{d}})$ should have properties P_1 and $P_2(k)$. Formulas 12, 13 and 14 are possible choices, provided that $k > 3/2$. (The choice of $b_{\text{fo|d}}(\alpha \mid \alpha_{\text{d}})$ may influence the already mentioned choice of the implicit proportionality constant in Formula 37.) $\xi_{\text{mean}}(k)$ should also be calculated using Formula 11. I believe that this calculation may have to be done numerically.

Now we have both $b_{\text{d}}(\alpha_{\text{d}})$ and $b_{\text{fo|d}}(\alpha \mid \alpha_{\text{d}})$, and $b(\alpha)$ could then be calculated using Formula 4. But then $b(\alpha)$ would not generally have the form given in Formula 15. However, if the conditions stated in Section 5 are fulfilled, we can use $b_{\text{appr}}(\alpha)$ given by Formula 21 instead of the $b(\alpha)$ of Formula 4. The sought α_{min} and α_{max} will then be given by $\alpha_{\text{min}} = \xi_{\text{mean}}(k)\alpha_{\text{d,min}}$ and $\alpha_{\text{max}} = \xi_{\text{mean}}(k)\alpha_{\text{d,max}}$. We have already obtained k and β_{tot}, and therefore we now know all parameters for the multirate model for the subdomain.

References

1. R. Haggerty and S. M. Gorelick. Multiple-rate mass transfer for modeling diffusion and surface reactions in media with pore-scale heterogeneity. *Water Resources Research*, 31(10):2383–2400, 1995.

2. R. Haggerty, S. A. McKenna and L. C. Meigs. On the late-time behavior of tracer test breakthrough curves. *Water Resources Research*, 36(12):3467–3479, 2000.

3. M. Sahimi. *Flow and Transport in Porous Media and Fractured Rock. From Classical Methods to Modern Approaches.* VCH Verlagsgesellschaft mbH, Weinheim, 1995.

4. P. R. LaPointe, T. Cladouhos and S. Follin. *Calculation of displacements on fractures intersecting canisters induced by earthquakes: Aberg, Beberg and Ceberg examples.* Technical Report TR-99-03. Svensk Kärnbränslehantering AB, Stockholm, January 1999.

Appendix C

A numerical method for generating a two-dimensional set of random numbers with a certain multivariate normal distribution

by Hans-Olof Kuylenstierna, 1994-06-15.

Contents

C.1 Introduction

This report describes a numerical method for generating a two-dimensional set of random numbers with a multivariate normal distribution characterized by a certain covariance structure.

A reader who only wants to learn the numerical method and the character of the random numbers that can be calculated using it can read Chapters C.1–C.8 straight through and skip the appendices. A reader who is also interested in derivations should read the entire report, in which case the following order is recommended: Chapters C.1–C.3, Appendix C1, Chapters C.4–C.7, Appendix C2, Chapter C.8, Appendix C3.

C.2 Multivariate normal distributions

In this chapter we shall introduce the concept of multivariate normal distribution.

Let n and m be non-negative integers, and let a_{ij}, $1 \leq i \leq n$, $1 \leq j \leq m$, and b_i, $1 \leq i \leq n$, be real numbers. Consider the joint probability distribution of the n stochastic variables $Y_i = \Sigma_{j=1}^{m} a_{ij} X_j + b_i$, $1 \leq i \leq n$, where X_j, $1 \leq j \leq m$, are independent stochastic variables with a standard normal distribution, i.e. a normal distribution with expected value 0 and standard deviation 1. This joint probability distribution will depend on the choice of n, m, a_{ij}, $1 \leq i \leq n$, $1 \leq j \leq m$, and b_i, $1 \leq i \leq n$.

Now consider the totality of joint probability distributions obtained from all possible choices of n, m, a_{ij}, $1 \leq i \leq n$, $1 \leq j \leq m$, and b_i, $1 \leq i \leq n$, as described in the previous paragraph. These distributions are called "multivariate normal distributions".

The following theorem is an elementary result about multivariate normal distributions: Let n be a non-negative integer, let X_i, $1 \leq i \leq n$, be stochastic variables with a multivariate normal distribution, and let also X_i, $1 \leq i \leq n$, be stochastic variables with a multivariate normal distribution. If $E[X_i] = E[Y_i]$, $1 \leq i \leq n$, and $\mathrm{Cov}(X_{i1}, X_{i2}) = \mathrm{Cov}\,(Y_{i1}, Y_{i2})$, $1 \leq i_1, i_2 \leq n$, then the two multivariate normal distributions are the same. In other words, a multivariate normal distribution is completely characterized by its expected values and covariances.

Multivariate normal distributions are discussed in Ross (1985, p 65–68).

C.3 Definition set 1

The definitions in this chapter shall be valid in some parts of the report. In those parts, it will be explicitly stated that the definitions in this chapter shall be valid.

Let x_0, y_0, a and b be real numbers which satisfy $a, b > 0$ and $x_0^2 + \mathrm{y}_0^2 = \mathrm{a}^2 – \mathrm{b}^2$. Define the quadratic form Q by letting

$$Q(x, y) = \frac{\left(b^2 + y_0^2\right)x^2 - 2x_0 y_0 xy + \left(b^2 + x_0^2\right)y^2}{a^2 b^2}$$

for all real numbers x and y.

C.4 Presentation of the quadratic form Q

Definition set 1 shall be valid in this chapter.

In this chapter we shall become a little familiar with the quadratic form Q.

With regard to the result of Section C1.2, it is clear that $Q(x, y) \geq 0$ for all x and y, equality holding precisely when $x, y = 0$.

In Section C1.4 it is shown that the equation $Q(x, y) = 1$ describes an ellipse with foci $(-x_0, -y_0)$ and (x_0, y_0) and half axis lengths a and b.

More generally, in Section C1.5 it is shown that for every real number $d > 0$ the equation $Q(x, y) = d^2$ describes an ellipse which has the same centre, orientation and shape but which is d times as large as the one described by $Q(x, y) = 1$.

C.5 Presentation of the numerical problem

Definition set 1 shall be valid in this chapter. Consider the following problem: Let n_r and n_k be non-negative integers. Construct a numerical method for generating random numbers H_{rk}, $1 \leq r \leq n_r$, $1 \leq k \leq n_k$, (H_{rk} are treated formally as stochastic variables here) which have a multivariate normal distribution characterized by

$E[H_{rk}] = 0,\ 1 \leq r \leq n_r, \quad 1 \leq k \leq n_k,$

$$\mathrm{Cov}\left(H_{r_1k_1}, H_{r_2k_2}\right) = \exp\left(-\frac{Q(r_2 - r_1, k_2 - k_1)}{2}\right), \qquad 1 \leq r_1, r_2 \leq n_r,\ 1 \leq k_1, k_2 \leq n_k.$$

We shall not give an exact solution to this problem in the report. However, in Chapter C.6 a variant of this problem where the covariances are only specified approximately will be given, and in Chapter C.8 a solution to this approximate problem will be given.

C.6 The approximate version of the numerical problem

Definition set 1 shall be valid in this chapter.

The approximate version of the numerical problem is the following: Let n_r and n_k be non-negative integers, and let ε be a positive real number. Construct a numerical method for generating random numbers H_{rk}, $1 \leq r \leq n_r$, $1 \leq k \leq n_k$, which have a multivariate normal distribution which satisfies

$E[H_{rk}] = 0,\ 1 \leq r \leq n_r, \quad 1 \leq k \leq n_k,$

$\mathrm{Var}\,(H_{rk}) = 1,\ 1 \leq r \leq n_r, \quad 1 \leq k \leq n_k,$

$$\left|\mathrm{Cov}\left(H_{r_1k_1},\ H_{r_2k_2}\right) - \ \exp\left(-\frac{Q(r_2 - r_1,\ k_2 - k_1)}{2}\right)\right| \leq \varepsilon, \qquad 1 \leq r_1,\ r_2 \leq n_r,\ 1 \leq k_1,\ k_2 \leq n_k.$$

C.7 Definition set 2

The definitions in this chapter shall be valid in some parts of the report. In those parts, it will be explicitly stated that the definitions in this chapter shall be valid.

The definitions in this chapter are given under the assumption that definition set 1 is valid, as the entities introduced there are referred to here. In those parts of the report where definition set 2 will be valid, definition set 1 will also be valid.

Numbers which can be written as integers divided by 2 we shall call “half-integers”. (If this is a standard term I do not know.) As Z normally denotes the set of integers, let $Z_{1/2}$ denote the set of half-integers. If e.g. r_0 is a half-integer variable and r_{01} and $r_{0\mathrm{h}}$ are half-integers, the expression $r_{01} \leq r_0 \leq r_{0\mathrm{h}}$ (1/2) shall mean that r_0 shall assume all half-integer values from r_{01} to $r_{0\mathrm{h}}$.

Let x_h and y_h be non-negative half-integers.

Let

$$M_{\mathrm{n}} = \left\{ (x, y) \in Z_{\frac{1}{2}} \times Z_{\frac{1}{2}} \middle| |x| \le x_{\mathrm{h}} \wedge |y| \le y_{\mathrm{h}} \right\},$$

$$M_{\mathrm{f}} = \left\{ (x, y) \in Z_{\frac{1}{2}} \times Z_{\frac{1}{2}} \middle| |x| > x_{\mathrm{h}} \vee |y| > y_{\mathrm{h}} \right\},$$

i.e. M_{n} is the set of those half-integer pairs in which the absolute value of the first half-integer is less than or equal to x_{h} and the absolute value of the second half-integer is less than or equal to y_{h}, and M_{f} is the set of those half-integer pairs that do not belong to M_{n}. "n" and "f" stand for "near" and "far", respectively.

In the report expressions like $(r, k) - M_{\mathrm{n}}$, where r and k are integers, will occur.

$(r, k) - M_{\mathrm{n}}$ means the set of half-integer pairs which can be written as differences between (r, k) and elements in M_{n}.

Let

$$\sigma_{\mathrm{n}} = \sqrt{\sum_{(x,y) \in M_{\mathrm{n}}} \exp\left(-2Q(x, y)\right)},$$

$$\sigma_{\mathrm{f}} = \sqrt{\sum_{(x,y) \in M_{\mathrm{f}}} \exp\left(-2Q(x, y)\right)}.$$

In the sum in the definition of σ_{n}, the term $\exp(-2Q(0.0)) = \exp(-2 \times 0) = 1$ is always present, and all terms are positive, so $\sigma_{\mathrm{n}} \ge 1$ The definition of σ_{f} is correct because the infinite series converges, which is shown in Section C2.4.

C.8 The solution to the approximate numerical problem

Definition sets 1 and 2 shall be valid in this chapter. We also keep the definitions from Chapter C.6.

The following is a solution to the approximate numerical problem:

Let

$$d = \max\left(\frac{1}{\sqrt{2} \times b}, \frac{1}{2\sqrt{2} \times b} + \sqrt{\max\left(0, \ln \frac{2\sqrt{\pi ab}}{\min\left(\frac{\varepsilon}{3}, \frac{1}{2}\right)}\right)} \right),$$

and let x_{h} and y_{h} be the smallest half-integers that still satisfy

$$x_{\mathrm{h}} \ge d\sqrt{b^2 + x_0^2} - \frac{1}{4}, \; y_{\mathrm{h}} \ge d\sqrt{b^2 + y_0^2} - \frac{1}{4}.$$

Let F_{r0k0}, $1 - x_{\mathrm{h}} \le r_0 \le n_{\mathrm{r}} + x_{\mathrm{h}}$ (1/2), $1 - y_{\mathrm{h}} \le k_0 \le n_{\mathrm{k}} + y_{\mathrm{h}}$ (1/2), be independent random numbers with a standard normal distribution these can be easily generated on a computer. Let

$$H_{rk} = \frac{\sum_{(r_0, k_0) \in (r,k) - M_{\mathrm{n}}} \left(\exp(-Q(r - r_0, k - k_0)) \times F_{r_0 k_0} \right)}{\sigma_{\mathrm{n}}}, \quad 1 \le r \le n_r, 1 \le k \le n_k.$$

The joint probability distribution of the H_{rk} will then meet the specifications given in Chapter C.6.

A derivation of this solution is given in Appendix C.

Appendix C1

Properties of the quadratic form *Q*

C1.1 Introduction

Throughout this appendix, definition set 1 shall be valid.

In this appendix, various properties of the quadratic form Q will be deduced. The results of the appendix are used in different parts of the report.

C1.2 $(x^2 + y^2)/ a^2 \le Q (x, y) \le (x^2 + y^2)/b^2$

In this section we shall show that

$$\frac{x^2+y^2}{a^2} \le Q(x, y) \le \frac{x^2+y^2}{b^2}$$

for all real numbers x and y.

Indeed, we have

$$-(y_0x - x_0y)^2 \le 0 \le (x_0x + y_0y)^2$$

$$-y_0^2x^2 + 2x_0y_0xy - x_0^2y^2 \le 0 \le x_0^2x^2 + 2x_0y_0xy + y_0^2y^2$$

$$b^2(x^2 + y^2) \le (b^2 + y_0^2)x^2 - 2x_0y_0xy + (b^2 + x_0^2)y^2 \le (b^2 + x_0^2 + y_0^2)(x^2 + y^2)$$

$$b^2(x^2 + y^2) \le (b^2 + y_0^2)x^2 - 2x_0y_0xy + (b^2 + x_0^2)y^2 \le a^2(x^2 + y^2)$$

$$\frac{x^2+y^2}{a^2} \le Q(x, y) \le \frac{x^2+y^2}{b^2}.$$

C1.3 $x^2 \le (b^2 + x_0^2)\, Q (x, y)$ and $y^2 \le (b^2 + y_0^2)\, Q (x, y)$

In this section we shall show that

$$x^2 \le (b^2 + x_0^2)\, Q(x, y),\ y^2 \le (b^2 + y_0^2)\, Q(x, y)$$

for all real numbers x and y.

To show the first inequality, we have

$$\frac{(b^2 + y_0^2)x^2 - 2x_0y_0xy + (b^2 + x_0^2)y^2}{a^2b^2} = Q(x, y)$$

$$\frac{(b^2 + x_0^2)\left((b^2 + y_0^2)x^2 - 2x_0y_0xy + (b^2 + x_0^2)y^2\right)}{a^2b^2} = (b^2 + x_0^2)Q(x, y)$$

$$\frac{(b^2 + x_0^2 + y_0^2)b^2x^2 + x_0^2y_0^2x^2 - 2(b^2 + x_0^2)x_0y_0xy + (b^2 + x_0^2)^2y^2}{a^2b^2} = (b^2 + x_0^2)Q(x, y)$$

$$\frac{a^2b^2x^2 + \left(x_0y_0x - (b^2 + x_0^2)y\right)^2}{a^2b^2} = (b^2 + x_0^2)Q(x, y)$$

$$x^2 \le (b^2 + x_0^2)Q(x, y).$$

The second inequality can be shown analogously.

C1.4 *Q* (*x*, *y*) = 1 describes an ellipse

In this section we shall show that the equation $Q(x, y) = 1$ describes an ellipse with foci $(-x_0, -y_0)$ and (x_0, y_0) and half-axis lengths a and b.

Consider the following sequence of equations:

$$Q(x, y) = 1$$

$$\Updownarrow$$

$$\left(b^2 + y_0^2\right)x^2 - 2x_0y_0xy + \left(b^2 + x_0^2\right)y^2 = a^2b^2$$

$$\Updownarrow$$

$$\left(a^2 - x_0^2\right)x^2 - 2x_0y_0xy + \left(a^2 - y_0^2\right)y^2 = a^2\left(a^2 - x_0^2 - y_0^2\right)$$

$$\Updownarrow$$

$$a^2\left(x^2 \pm 2x_0x + x_0^2 + y^2 \pm 2y_0y + y_0^2\right) = a^4 \pm 2a^2\left(x_0x + y_0y\right) + x_0^2x^2 + 2x_0y_0xy + y_0^2y^2$$

$$\Updownarrow$$

$$a^2\left(\left(x \pm x_0\right)^2 + \left(y \pm y_0\right)^2\right) = \left(a^2 \pm \left(x_0x + y_0y\right)\right)^2$$

$$\Uparrow$$

$$a\sqrt{\left(x \pm x_0\right)^2 + \left(y \pm y_0\right)^2} = a^2 \pm \left(x_0x + y_0y\right)$$

$$\Updownarrow$$

$$4a\sqrt{\left(x \pm x_0\right)^2 + \left(y \pm y_0\right)^2} = 4a^2 + \left(x \pm x_0\right)^2 + \left(y \pm y_0\right)^2 - \left(x \mp x_0\right)^2 - \left(y \mp y_0\right)^2$$

$$\Updownarrow$$

$$\begin{aligned}
&2a\left(\sqrt{\left(x + x_0\right)^2 + \left(y + y_0\right)^2} + \sqrt{\left(x - x_0\right)^2 + \left(y - y_0\right)^2} + \right.\\
&\left. + \sqrt{\left(x \pm x_0\right)^2 + \left(y \pm y_0\right)^2} - \sqrt{\left(x \mp x_0\right)^2 + \left(y \mp y_0\right)^2}\right) =\\
&= 4a^2 + \left(\sqrt{\left(x \pm x_0\right)^2 + \left(y \pm y_0\right)^2} - \sqrt{\left(x \mp x_0\right)^2 + \left(y \mp y_0\right)^2}\right) \times\\
&\times \left(\sqrt{\left(x + x_0\right)^2 + \left(y + y_0\right)^2} + \sqrt{\left(x - x_0\right)^2 + \left(y - y_0\right)^2}\right)
\end{aligned}$$

$$\Updownarrow$$

$$\begin{aligned}
0 &= \left(2a - \sqrt{\left(x \pm x_0\right)^2 + \left(y \pm y_0\right)^2} + \sqrt{\left(x \mp x_0\right)^2 + \left(y \mp y_0\right)^2}\right) \times\\
&\times \left(2a - \sqrt{\left(x + x_0\right)^2 + \left(y + y_0\right)^2} - \sqrt{\left(x - x_0\right)^2 + \left(y - y_0\right)^2}\right)
\end{aligned}$$

$$\Uparrow$$

$$0 = 2a - \sqrt{\left(x + x_0\right)^2 + \left(y + y_0\right)^2} - \sqrt{\left(x - x_0\right)^2 + \left(y - y_0\right)^2}$$

$$\Updownarrow$$

$$\sqrt{\left(x + x_0\right)^2 + \left(y + y_0\right)^2} + \sqrt{\left(x - x_0\right)^2 + \left(y - y_0\right)^2} = 2a$$

Obvious equivalences and implications have been indicated with arrows. Each equation containing “+ _” or “+ ¯” signs is to be regarded as the statement that both versions of the equation hold. Because of the direction of the two implication arrows, it is clear that the last equation in the sequence implies the first one. However, the first one also implies the last one, which we shall show here. Start by assuming that the first equation holds. Then the fifth equation must also hold. Moreover, in Section C1.2 it is shown that $(x^2 + y^2)/a^2 \leq Q(x, y)$. As $Q(x, y) = 1$, we have $\sqrt{x^2 + y^2} \leq a$. As $x_0^2 + y_0^2 = a^2 - b^2$, we also have $\sqrt{x_0^2 + y_0^2} \leq a$. Now the Schwarz inequality gives us $|x_0 x + y_0 y| \leq \sqrt{x_0^2 + y_0^2} \times \sqrt{x^2 + y^2} \leq a \times a = a^2$, which in turn yields $0 \leq a^2 \pm (x_0 x + y_0 y)$. Together with this fact, the fifth equation gives us the sixth one. Adding together the two versions of this equation and dividing the sum equation by a directly gives us the last equation.

As the first and the last equation in the sequence are thus equivalent, it only remains to show that the last equation describes the specified ellipse.

An ellipse can be defined as the set of those points whose distances to two given points, the foci of the ellipse, have a constant given sum. This is indeed expressed by the last equation of the sequence, if $(-x_0, -y_0)$ and (x_0, y_0) are the foci and $2a$ is the total distance. Imagining an ellipse, one can see that the total distance is equal to the length of the long axis of the ellipse, and one can also see that half the interfocal distance, half the short axis and half the given total distance form a right triangle. The half long axis length must therefore be a, and the half short axis length must be:

$$\sqrt{a^2 - \left(\sqrt{x_0^2 + y_0^2}\right)^2} = \sqrt{a^2 - x_0^2 - y_0^2} = b.$$

C1.5 $Q(x, y) = d^2$ also describes an ellipse

In this section we shall show that for every real number $d > 0$ the equation $Q(x, y) = d^2$ describes an ellipse which has the same centre $(x, y = 0)$, orientation and shape but which is d times as large as the one described by $Q(x, y) = 1$. (The ellipse $Q(x, y) = 1$ is discussed in the previous section.)

We can convince ourselves that the ellipse mentioned which is d times as large as the $Q(x, y) = 1$ one, must be described by the equation $Q(x/\mathrm{d}, y/\mathrm{d}) = 1$. However, this equation is equivalent to $Q(x, y) = d^2$, which is easily seen on inspection of the definition of Q.

C1.6 Linear transformation between (x, y) and (ξ, η) coordinates

In this section we shall introduce a coordinate transformation and determine some of its properties.

Define

$$t_{x\xi} = \frac{b^2 + x_0^2 + ab}{a+b}, \quad t_{x\eta} = \frac{x_0 y_0}{a+b},$$

$$t_{y\xi} = \frac{x_0 y_0}{a+b}, \quad t_{y\eta} = \frac{b^2 + y_0^2 + ab}{a+b},$$

and introduce a linear transformation from new coordinates ξ and η to the old ones x and y by

$$x = t_{x\xi}\xi + t_{x\eta}\eta, \quad y = t_{y\xi}\xi + t_{y\eta}\eta.$$

The area scale of the transformation is

$$t_{x\xi}t_{y\eta} - t_{x\eta}t_{y\xi} =$$

$$= \frac{\left(b^2 + x_0^2 + ab\right)\left(b^2 + y_0^2 + ab\right) - x_0 y_0 x_0 y_0}{(a+b)^2} =$$

$$= \frac{\left(b^2 + x_0^2 + y_0^2 + b^2 + ab\right)ab + \left(b^2 + x_0^2 + y_0^2\right)b^2}{(a+b)^2} =$$

$$= \frac{\left(a^2 + b^2 + ab\right)ab + a^2 b^2}{(a+b)^2} = \frac{\left(a^2 + 2ab + b^2\right)ab}{(a+b)^2} = ab.$$

I.e. if a variable substitution in a double integral is to be made, the formula

$dx\, dy = ab\, d\xi d\eta$

should be used.

We have

$$t_{y\eta}x - t_{x\eta}y = t_{y\eta}\left(t_{x\xi}\xi + t_{x\eta}\eta\right) - t_{x\eta}\left(t_{y\xi}\xi + t_{y\eta}\eta\right) =$$

$$= (t_{x\xi}t_{y\eta} - t_{x\eta}t_{y\xi})\ \xi = ab\xi,$$

$$-t_{y\xi}x + t_{x\xi}y = -t_{y\xi}\left(t_{x\xi}\xi + t_{x\eta}\eta\right) + t_{x\xi}\left(t_{y\xi}\xi + t_{y\eta}\eta\right) =$$

$$= (t_{x\xi}t_{y\eta} - t_{x\eta}t_{y\xi})\ \eta = ab\eta,$$

so the inverse transformation is given by

$$\xi = \frac{t_{y\eta}\ x - t_{x\eta}y}{ab}, \quad \eta = \frac{-t_{y\xi}x + t_{x\xi}y}{ab}.$$

We have

$$t_{x\xi}^2 + t_{x\eta}^2 = \frac{\left(b^2 + x_0^2 + ab\right)^2 + \left(x_0 y_0\right)^2}{(a+b)^2} =$$

$$= \frac{\left(b^2 + x_0^2\right)\left(b^2 + 2ab\right) + \left(b^2 + x_0^2\right)x_0^2 + a^2b^2 + x_0^2y_0^2}{(a+b)^2} =$$

$$= \frac{\left(b^2 + x_0^2\right)\left(b^2 + 2ab\right) + \left(b^2 + x_0^2 + y_0^2\right)x_0^2 + a^2b^2}{(a+b)^2} =$$

$$= \frac{\left(b^2 + x_0^2\right)\left(b^2 + 2ab\right) + a^2x_0^2 + a^2b^2}{(a+b)^2} =$$

$$= \frac{\left(b^2 + x_0^2\right)\left(a^2 + 2ab + b^2\right)}{(a+b)^2} = b^2 + x_0^2,$$

$$t_{x\xi}t_{y\xi} + t_{x\eta}t_{y\eta} = \frac{\left(b^2 + x_0^2 + ab\right)x_0y_0 + x_0y_0\left(b^2 + y_0^2 + ab\right)}{(a+b)^2} =$$

$$= \frac{\left(b^2 + x_0^2 + y_0^2 + 2ab + b^2\right)x_0y_0}{(a+b)^2} = \frac{\left(a^2 + 2ab + b^2\right)x_0y_0}{(a+b)^2} = x_0y_0,$$

$$t_{y\xi}^2 + t_{y\eta}^2 = \frac{\left(x_0y_0\right)^2 + \left(b^2 + y_0^2 + ab\right)^2}{(a+b)^2} =$$

$$= \frac{x_0^2y_0^2 + \left(b^2 + y_0^2\right)\left(b^2 + 2ab\right) + \left(b^2 + y_0^2\right)y_0^2 + a^2b^2}{(a+b)^2} =$$

$$= \frac{\left(b^2 + y_0^2\right)\left(b^2 + 2ab\right) + \left(b^2 + x_0^2 + y_0^2\right)y_0^2 + a^2b^2}{(a+b)^2} =$$

$$= \frac{\left(b^2 + y_0^2\right)\left(b^2 + 2ab\right) + a^2y_0^2 + a^2b^2}{(a+b)^2} =$$

$$= \frac{\left(b^2 + y_0^2\right)\left(a^2 + 2ab + b^2\right)}{(a+b)^2} = b^2 + y_0^2,$$

and therefore

$$\xi^2+\eta^2=\left(\frac{t_{y\eta}x-t_{x\eta}y}{ab}\right)^2+\left(\frac{-t_{y\xi}x+t_{x\xi}y}{ab}\right)^2=$$

$$=\frac{\left(t_{y\xi}^2+t_{y\eta}^2\right)x^2-2\left(t_{x\xi}t_{y\xi}+t_{x\eta}t_{y\eta}\right)xy+\left(t_{x\xi}^2+t_{x\eta}^2\right)y^2}{a^2b^2}=$$

$$=\frac{\left(b^2+y_0^2\right)x^2-2x_0y_0xy+\left(b^2+x_0^2\right)y^2}{a^2b^2}=Q(x,y).$$

C1.7 Identity with four *Q*

In this section we shall show that

$$Q(x_1+x_2,y_1+y_2)+Q(x_2-x_1,y_2-y_1)=2(Q(x_1,y_1)+Q(x_2,y_2))$$

for all real numbers x_1, y_1, x_2 and y_2.

Using the coordinate transformation in Section C1.6, we let (x_1, y_1) and (x_2, y_2) correspond to (ξ_1, η_1) and (ξ_2, η_2), respectively. As the transformation is linear, (x_1+x_2, y_1+y_2) and (x_2-x_1, y_2-y_1) will then correspond to ($\xi_1+\xi_2$, $\eta_1+\eta_2$) and ($\xi_2-\xi_1$, $\eta_2-\eta_1$), respectively. With the new coordinates the above equation can be written

$$(\xi_1+\xi_2)^2+(\eta_1+\eta_2)^2+(\xi_2-\xi_1)^2+(\eta_2-\eta_1)^2=2\left(\xi_1^2+\eta_1^2+\xi_2^2+\eta_2^2\right),$$

which is an obvious identity.

C1.8 Triangle inequality with *Q*

In this section we shall show that

$$\left|\sqrt{Q(x_2,y_2)}-\sqrt{Q(x_1,y_1)}\right|\le\sqrt{Q(x_2-x_1,y_2-y_1)},$$

$$\sqrt{Q(x_1+x_2,y_1+y_2)}\le\sqrt{Q(x_1,y_1)}+\sqrt{Q(x_2,y_2)}$$

for all real numbers x_1, y_1, x_2 and y_2.

Changing to new coordinates as in the previous section, the above inequalities can be written

$$\left|\sqrt{\xi_2^2+\eta_2^2}-\sqrt{\xi_1^2+\eta_1^2}\right|\le\sqrt{(\xi_2-\xi_1)^2+(\eta_2-\eta_1)^2},$$

$$\sqrt{(\xi_1+\xi_2)^2+(\eta_1+\eta_2)^2}\le\sqrt{\xi_1^2+\eta_1^2}+\sqrt{\xi_2^2+\eta_2^2}.$$

These inequalities are the well-known triangle inequality in two dimensions, which we do not prove here.

Appendix C2

Properties of σ_f

C2.1 Introduction

Throughout this appendix, definition sets 1 and 2 shall be valid.

In this appendix, a few properties of σ_f will be deduced. The results of the appendix are used in Chapter C.7 and Appendix C3.

C2.2 An upper estimation of an integral

In this section we shall show that if c and d are real numbers which satisfy $0 < c \le d/2$, then

$$\iint\limits_{Q(x,y)\ge d^2} \exp\left(-2\left(\sqrt{Q(x,y)}-c\right)^2\right)\times dx\, dy \le$$

$$\le \pi ab \exp\left(-2(d-c)^2\right).$$

Indeed, we have

$$\iint\limits_{Q(x,y)\ge d^2} \exp\left(-2\left(\sqrt{Q(x,y)}-c\right)^2\right)\times dx\, dy =$$

= [substitution from x, y to ξ, η as described in Section C1.6]=

$$= \iint\limits_{\xi^2+\eta^2\ge d^2} \exp\left(-2\left(\sqrt{\xi^2+\eta^2}-c\right)^2\right)\times ab\, d\xi d\eta =$$

$$= \left[\xi = \rho\cos\varphi,\ \eta = \rho\sin\varphi,\ d\xi d\eta = \rho d\varphi d\rho\right] =$$

$$= ab\int_d^\infty\int_0^{2\pi} \exp\left(-2(\rho-c)^2\right)\times \rho d\varphi d\rho =$$

$$= 2\pi ab\int_d^\infty \frac{\rho}{\rho-c}(\rho-c)\exp\left(-2(\rho-c)^2\right)\times d\rho \le$$

$$\le \pi ab\int_d^\infty 4(\rho-c)\exp\left(-2(\rho-c)^2\right)\times d\rho =$$

$$= \pi ab\left[-\exp\left(-2(\rho-c)^2\right)\right]_d^\infty = \pi ab\exp\left(-2(d-c)^2\right),$$

because $\rho/(\rho-c) \le 2$ when $\rho \ge 2c$.

C2.3 A sufficient condition that $\sigma_f \le \delta$

In this section we shall show that for any given real number $\delta > 0$, if we choose the real number d and the half-integers x_h and y_h so that they satisfy

$$d \ge \frac{1}{\sqrt{2}\times b},\quad 4\pi ab\exp\left(-2\left(d-\frac{1}{2\sqrt{2}\times b}\right)^2\right) \le \delta^2,$$

$$x_h + \frac{1}{4} \ge d\sqrt{b^2+x_0^2},\quad y_h + \frac{1}{4} \ge d\sqrt{b^2+y_0^2},$$

then $\sigma_f \le \delta$.

Indeed, we have

$$\sigma_{\mathrm{f}}^2 = \sum_{(x',y')\in M_{\mathrm{f}}} \exp\left(-2Q(x',y')\right) =$$

$$= \sum_{(x',y')\in M_{\mathrm{f}}} 4 \int_{y'-\frac{1}{4}}^{y'+\frac{1}{4}} \int_{x'-\frac{1}{4}}^{x'+\frac{1}{4}} \exp\left(-2Q(x',y')\right)\times dx\, dy \leq$$

$$\leq [\text{comment 1}] \leq$$

$$\leq 4 \sum_{(x',y')\in M_{\mathrm{f}}} \int_{y'-\frac{1}{4}}^{y'+\frac{1}{4}} \int_{x'-\frac{1}{4}}^{x'+\frac{1}{4}} \exp\left(-2\left(\sqrt{Q(x,y)} - \frac{1}{2\sqrt{2}\times b}\right)^2\right)\times dx\, dy =$$

$$= 4 \iint\limits_{|x|\geq x_{\mathrm{h}}+\frac{1}{4}\vee|y|\geq y_{\mathrm{h}}+\frac{1}{4}} \exp\left(-2\left(\sqrt{Q(x,y)} - \frac{1}{2\sqrt{2}\times b}\right)^2\right)\times dx\, dy \leq$$

$$\leq [\text{comment 2}] \leq$$

$$\leq 4 \iint\limits_{Q(x,y)\geq d^2} \exp\left(-2\left(\sqrt{Q(x,y)} - \frac{1}{2\sqrt{2}\times b}\right)^2\right)\times dx\, dy \leq$$

$$\leq [\text{comment 3}] \leq 4\pi ab \exp\left(-2\left(d - \frac{1}{2\sqrt{2}\times b}\right)^2\right) \leq \delta^2,$$

i.e. $\sigma_{\mathrm{f}} \leq \delta$. However, some of the above steps need comments:

Comment 1. Because $|x–x'| \leq 1/4$ and $|y–y'| \leq 1/4$, $(x–x')^2 + (y–y')^2 \leq 1/8$. According to Section C1.2, $Q(x–x', y–y') \leq ((x–x')^2 + (y–y')^2)/b^2$. According to Section C1.8, $\sqrt{Q(x',y')} \geq \left|\sqrt{Q(x,y)} - \sqrt{Q(x-x',y-y')}\right|$. Using these facts, we have

$$\sqrt{Q(x',y')} \geq \left|\sqrt{Q(x,y)} - \sqrt{Q(x-x',y-y')}\right| \geq$$

$$\geq \sqrt{Q(x,y)} - \sqrt{Q(x-x',y-y')} \geq \sqrt{Q(x,y)} - \frac{\sqrt{(x-x')^2+(y-y')^2}}{b} \geq$$

$$\geq \sqrt{Q(x,y)} - \frac{1}{2\sqrt{2}\times b}.$$

Because $(x', y') \in M_{\mathrm{f}}$, $|x'| > x_{\mathrm{h}}$ or $|y'| > y_{\mathrm{h}}$. As x', x_{h}, y' and y_{h} are half-integers, $|x'| \geq x_{\mathrm{h}} + 1/2$ or $|y'| \geq y_{\mathrm{h}} + 1/2$ must hold. As $|x–x'| \leq 1/4$ and $|y–y' \leq 1/4$, $|x| \geq x_{\mathrm{h}} + 1/4$ or $|y| \geq y_{\mathrm{h}} + 1/4$ must hold. According to comment 2, then $Q(x, y) \geq d^2$ most hold. As d satisfies $d \geq (\sqrt{2}\times\mathrm{b})$, we have

$$\sqrt{Q(x,\ y)} \geq d \geq \frac{1}{\sqrt{2}\times b} > \frac{1}{2\sqrt{2}\times b}.$$

The above inequality $\sqrt{Q(x',\ y')} \geq \sqrt{Q(x,\ y)} - 1/\left(2\sqrt{2}\times b\right)$ can therefore be squared, and we obtain

$$Q(x',y') \geq \left(\sqrt{Q(x,y)} - \frac{1}{2\sqrt{2}\times b}\right)^2.$$

Comment 2. We shall show that if $|x| \geq x_\mathrm{h} + 1/4$ or $|y| \geq y_\mathrm{h} + 1/4$, then $Q(x, y) \geq d^2$. In fact, remembering that $x_\mathrm{h} + 1/4 \geq d\sqrt{b^2 + x_0^2}$ and $y_\mathrm{h} + 1/4 \geq d\sqrt{b^2 + y_0^2}$, we can conclude that $x^2/(b^2 + x_0^2) \geq d^2$ or $x^2/(b^2 + x^2{}_0) \geq d^2$ or $y^2/(b^2 + y^2{}_0) \geq d^2$. However, according to Section C1.3 $Q(x, y)$ is greater than or equal to both $x^2/(b^2 + x^2{}_0)$ and $y^2/(b^2 + y^2{}_0)$. Therefore $Q(x, y) \geq d^2$ must hold in both cases.

Comment 3. The inequality follows directly from what is shown in Section C2.2.

C2.4 σ_f is finite for all x_h and y_h

Consider the definition of σ_f:

$$\sigma_\mathrm{f} = \sqrt{\sum_{(x,y)\in M_\mathrm{f}} \exp\left(-2Q(x, y)\right)}.$$

In order that the definition shall be valid, it is necessary that the infinite series in the definition converges. This is indeed the case, as we shall show in this section.

For any choice of the non-negative half-integers x_h and y_h, M_f will contain all but a finite number of the elements of $Z_{1/2} \times Z_{1/2}$. Therefore, either the series will converge for all choices of x_h and y_h, or it will diverge for all choices. But in Section C2.3 it was shown that if sufficiently large x_h and y_h values are chosen, the series will converge. Thus, the series will converge for all choices of x_h and y_h.

Appendix C3

Derivation of the solution to the approximate numerical problem

Definition sets 1 and 2 as well as the definitions made in Chapters C.6 and C.8 shall be valid in this appendix.

In this appendix we shall show that the numerical method described in Chapter C.8 really is a solution to the approximate numerical problem stated in Chapter C.6. The derivation will be given in four parts.

Part 1. We shall show that the H_{rk} have a multivariate normal distribution.

This is really the case, as the H_{rk} are linear combinations of a set of independent random numbers with a standard normal distribution.

Part 2. We shall show that $E[H_{rk}] = 0,\ 1 \le r \le n_r,\ 1 \le k \le n.$

This is the case because the H_{rk} are linear combinations of a set of random numbers with expected value 0.

Part 3. We shall show that $\mathrm{Var}(H_{rk}) = 1,\ 1 \le r \le n_r,\ 1 \le k \le n.$

As the $F_{r_0k_0}$ are independent and have variance 1, we have

$$\mathrm{Var}(H_{rk}) = \mathrm{Var}\left(\frac{\sum\limits_{(r_0,k_0)\in(r,k)-M_\mathrm{n}}\left(\exp\left(-Q(r-r_0,k-k_0)\right)\times F_{r_0k_0}\right)}{\sigma_\mathrm{n}}\right) =$$

$$= \frac{\sum\limits_{(r_0,k_0)\in(r,k)-M_\mathrm{n}}\left(\exp\left(-Q(r-r_0,k-k_0)\right)\right)^2 \mathrm{Var}\left(F_{r_0k_0}\right)}{\sigma_\mathrm{n}^2} =$$

$$= \frac{\sum\limits_{(x,y)\in M_\mathrm{n}}\exp\left(-2Q(x,y)\right)}{\sigma_\mathrm{n}^2} = 1.$$

Part 4. We shall show that

$$\left|\mathrm{Cov}\left(H_{r_1k_1},\ H_{r_2k_2}\right) - \exp\left(-\frac{Q(r_2-r_1,\ k_2-k_1)}{2}\right)\right| \le \varepsilon, \qquad 1 \le r_1,\ r_2 \le n_r,\ 1 \le k_1,\ k_2 \le n_k.$$

This part of the derivation of the numerical method is rather complicated. We shall derive the inequality in a single sequence of inequalities and equalities. After that, some of the steps in the sequence will be commented.

$$\left|\mathrm{Cov}\left(H_{r_1k_1}, H_{r_2k_2}\right) - \exp\left(-\frac{Q(r_2-r_1,k_2-k_1)}{2}\right)\right| =$$

$$= \left|\mathrm{Cov}\left(H_{r_1k_1}, H_{r_2k_2}\right) - \frac{\sigma_\mathrm{n}^2+\sigma_\mathrm{f}^2}{\sigma_\mathrm{n}^2}\exp\left(-\frac{Q(r_2-r_1,k_2-k_1)}{2}\right) + \right.$$

$$\left. + \frac{\sigma_\mathrm{f}^2}{\sigma_\mathrm{n}^2}\exp\left(-\frac{Q(r_2-r_1,\ k_2-k_1)}{2}\right)\right| =$$

$$= [\text{comments } 1\text{–}2] =$$

$$= \left|\frac{\sum\limits_{(r_0,k_0)\in((r_1,k_1)-M_\mathrm{n})\cap((r_2,k_2)-M_\mathrm{n})}\exp\left(-Q(r_1-r_0,k_1-k_0)-Q(r_2-r_0,k_2-k_0)\right)}{\sigma_\mathrm{n}^2} - \right.$$

$$-\frac{\sum\limits_{(r_0,k_0)\in Z_{\frac{1}{2}}\times Z_{\frac{1}{2}}}\exp\left(-Q(r_1-r_0,k_1-k_0)-Q(r_2-r_0,k_2-k_0)\right)}{\sigma_{\mathrm{n}}^2}+$$

$$\left.+\frac{\sigma_{\mathrm{f}}^2}{\sigma_{\mathrm{n}}^2}\exp\left(-\frac{Q\left(r_2-r_1,\ k_2-k_1\right)}{2}\right)\right|=$$

$$=\left|-\frac{\sum\limits_{(r_0,k_0)\in((r_1,k_1)-M_{\mathrm{n}})\cap((r_2,k_2)-M_{\mathrm{f}})}\exp\left(-Q(r_1-r_0,k_1-k_0)-Q(r_2-r_0,k_2-k_0)\right)}{\sigma_{\mathrm{n}}^2}-\right.$$

$$-\frac{\sum\limits_{(r_0,k_0)\in((r_1,k_1)-M_{\mathrm{f}})\cap((r_2,k_2)-M_{\mathrm{n}})}\exp\left(-Q(r_1-r_0,k_1-k_0)-Q(r_2-r_0,k_2-k_0)\right)}{\sigma_{\mathrm{n}}^2}-$$

$$-\frac{\sum\limits_{(r_0,k_0)\in((r_1,k_1)-M_{\mathrm{f}})\cap((r_2,k_2)-M_{\mathrm{f}})}\exp\left(-Q(r_1-r_0,k_1-k_0)-Q(r_2-r_0,k_2-k_0)\right)}{\sigma_{\mathrm{n}}^2}+$$

$$\left.+\frac{\sigma_{\mathrm{f}}^2}{\sigma_{\mathrm{n}}^2}\exp\left(-\frac{Q\left(r_2-r_1,\ k_2-k_1\right)}{2}\right)\right|\le$$

$$\le\left[\text{triangle inequality}+\text{comments 3–4}\right]\le$$

$$\le\frac{\sigma_{\mathrm{n}}\sigma_{\mathrm{f}}}{\sigma_{\mathrm{n}}^2}+\frac{\sigma_{\mathrm{f}}\sigma_{\mathrm{n}}}{\sigma_{\mathrm{n}}^2}+\frac{\sigma_{\mathrm{f}}^2}{\sigma_{\mathrm{n}}^2}+\frac{\sigma_{\mathrm{f}}^2}{\sigma_{\mathrm{n}}^2}=\frac{\sigma_{\mathrm{f}}}{\sigma_{\mathrm{n}}}\left(2+2\frac{\sigma_{\mathrm{f}}}{\sigma_{\mathrm{n}}}\right)\le\left[\text{comments 5–6}\right]\le$$

$$\le\frac{\frac{\varepsilon}{3}}{1}\left(2+2\times\frac{\frac{1}{2}}{1}\right)=\varepsilon$$

Comment 1. We shall show that

$$\mathrm{Cov}\left(H_{r_1k_1},H_{r_2k_2}\right)=$$

$$=\frac{\sum\limits_{(r_0,k_0)\in((r_1,k_1)-M_{\mathrm{n}})\cap((r_2,k_2)-M_{\mathrm{n}})}\exp\left(-Q(r_1-r_0,k_1-k_0)-Q(r_2-r_0,k_2-k_0)\right)}{\sigma_{\mathrm{n}}^2}.$$

The $F_{r_0k_0}$ are independent and have variance 1, so Cov($F_{r_{01}k_{01}}$, $F_{r_{02}k_{02}}$) is equal to 1 when ($r_{01}k_{01}$) = ($r_{02}k_{02}$) and 0 otherwise. Therefore we have

$$\mathrm{Cov}\left(H_{r_1k_1},H_{r_2k_2}\right)=$$

$$=\mathrm{Cov}\left(\frac{\sum\limits_{(r_0,k_0)\in(r_1,k_1)-M_{\mathrm{n}}}\left(\exp\left(-Q(r_1-r_0,k_1-k_0)\right)\times F_{r_0k_0}\right)}{\sigma_{\mathrm{n}}},\right.$$

$$\left.\frac{\sum\limits_{(r_0,k_0)\in(r_2,k_2)-M_{\mathrm{n}}}\left(\exp\left(-Q(r_2-r_0,k_2-k_0)\right)\times F_{r_0k_0}\right)}{\sigma_{\mathrm{n}}}\right)=$$

$$= \frac{\sum_{(r_0,k_0)\in((r_1,k_1)-M_{\mathrm{n}})\cap((r_2,k_2)-M_{\mathrm{n}})} \left(\exp\left(-Q(r_1-r_0,k_1-k_0)\right)\times\exp\left(-Q(r_2-r_0,k_2-k_0)\right)\right)}{\sigma_{\mathrm{n}}^2} =$$

$$= \frac{\sum_{(r_0,k_0)\in((r_1,k_1)-M_{\mathrm{n}})\cap((r_2,k_2)-M_{\mathrm{n}})} \exp\left(-Q(r_1-r_0,k_1-k_0)-Q(r_2-r_0,k_2-k_0)\right)}{\sigma_{\mathrm{n}}^2}.$$

Comment 2. We shall show that

$$\sum_{(r_0,k_0)\in Z_{\frac{1}{2}}\times Z_{\frac{1}{2}}} \exp\left(-Q(r_1-r_0,k_1-k_0)-Q(r_2-r_0,k_2-k_0)\right) =$$

$$= \left(\sigma_{\mathrm{n}}^2+\sigma_{\mathrm{f}}^2\right)\exp\left(-\frac{Q(r_2-r_1,k_2-k_1)}{2}\right).$$

From the definition of Q it is easy to see that $2Q((r_2–r_1)/2, (k_2–k_1)/2) = Q(r_2–r_1, k_2–k_1)/2$. This fact together with the result of Section C1.7 gives us

$$Q(r_1-r_0,k_1-k_0)+Q(r_2-r_0,k_2-k_0)=$$

$$=2\left(Q\left(\frac{r_2-r_1}{2},\frac{k_2-k_1}{2}\right)+Q\left(\frac{r_1+r_2}{2}-r_0,\frac{k_1+k_2}{2}-k_0\right)\right)=$$

$$=\frac{Q(r_2-r_1,k_2-k_1)}{2}+2Q\left(\frac{r_1+r_2}{2}-r_0,\frac{k_1+k_2}{2}-k_0\right).$$

This identity enables us to conclude that

$$\sum_{(r_0,k_0)\in Z_{\frac{1}{2}}\times Z_{\frac{1}{2}}} \exp\left(-Q(r_1-r_0,k_1-k_0)-Q(r_2-r_0,k_2-k_0)\right) =$$

$$= \sum_{(r_0,k_0)\in Z_{\frac{1}{2}}\times Z_{\frac{1}{2}}} \exp\left(-\frac{Q(r_2-r_1,k_2-k_1)}{2}-2Q\left(\frac{r_1+r_2}{2}-r_0,\frac{k_1+k_2}{2}-k_0\right)\right)=$$

$$= \exp\left(-\frac{Q(r_2-r_1,k_2-k_1)}{2}\right)\times\sum_{(x,y)\in Z_{\frac{1}{2}}\times Z_{\frac{1}{2}}}\exp\left(-2Q(x,y)\right)=$$

$$= \exp\left(-\frac{Q(r_2-r_1,k_2-k_1)}{2}\right)\times\left(\sum_{(x,y)\in M_{\mathrm{n}}}\exp\left(-2Q(x,y)\right)+\sum_{(x,y)\in M_{\mathrm{f}}}\exp\left(-2Q(x,y)\right)\right)=$$

$$= \left(\sigma_{\mathrm{n}}^2+\sigma_{\mathrm{f}}^2\right)\exp\left(-\frac{Q(r_2-r_1,k_2-k_1)}{2}\right).$$

Comment 3. We shall show that the three sums on the left side of the inequality sign are less than or equal to $\sigma_{\mathrm{n}}\,\sigma_{\mathrm{f}}$, $\sigma_{\mathrm{f}}\,\sigma_{\mathrm{n}}$ and σ_{f}^2, respectively.

We shall only derive the first of these three inequalities here, as the other two can be derived analogously.

$$\sum_{(r_0,k_0)\in((r_1,k_1)-M_{\mathrm{n}})\cap((r_2,k_2)-M_{\mathrm{f}})} \exp\left(-Q(r_1-r_0,k_1-k_0)-Q(r_2-r_0,k_2-k_0)\right)=$$

$$= \sum_{(r_0,k_0)\in((r_1,k_1)-M_{\mathrm{n}})\cap((r_2,k_2)-M_{\mathrm{f}})} \left(\exp\left(-Q(r_1-r_0,k_1-k_0)\right)\times\exp\left(-Q(r_2-r_0,k_2-k_0)\right)\right)\le$$

$$\le [\text{Schwarz inequality}] \le$$

$$\leq \sqrt{\sum_{(r_0,k_0)\in(r_1,k_1)-M_\mathrm{n}} \left(\exp\left(-Q(r_1-r_0,k_1-k_0)\right)\right)^2} \times$$

$$\times \sqrt{\sum_{(r_0,k_0)\in(r_2,k_2)-M_\mathrm{f}} \left(\exp\left(-Q(r_2-r_0,k_2-k_0)\right)\right)^2} =$$

$$= \sqrt{\sum_{(x,y)\in M_\mathrm{n}} \exp\left(-2Q(x,y)\right)} \times \sqrt{\sum_{(x,y)\in M_\mathrm{f}} \exp\left(-2Q(x,y)\right)} =$$

$$= \sigma_\mathrm{n}\sigma_\mathrm{f}$$

Comment 4. We shall show that exp $(-Q(r_2-r_1, k_2-k_1)/2) \leq 1$.

It is sufficient to note that $Q(r_2-r_1, k_2-k_1) \geq 0$ which follows from the result of Section C1.2.

Comment 5. $\sigma_\mathrm{n} \geq 1$, as we noted in Chapter C.7.

Comment 6. We shall convince ourselves that $\sigma_\mathrm{f} \leq \varepsilon/3$ and $\sigma_\mathrm{f} \leq 1/2$.

The conditions on d, x_h and y_h given in Chapter C.8 imply that

$$d \geq \frac{1}{\sqrt{2}\times b},\ \ 4\pi ab\exp\left(-2\left(d-\frac{1}{2\sqrt{2}\times b}\right)^2\right) \leq \left(\min\left(\frac{\varepsilon}{3},\frac{1}{2}\right)\right)^2,$$

$$x_\mathrm{h}+\frac{1}{4} \geq d\sqrt{b^2+x_0^2},\ \ y_\mathrm{h}+\frac{1}{4} \geq d\sqrt{b^2+y_0^2}.$$

According to Section C1.3, then $\sigma_\mathrm{f} \leq \min(\varepsilon/3, 1/2)$.

Generation of random points with a Fisher distribution

Generation of random points with a Fisher distribution

Hans-Olof Kuylenstierna

13th March 2003

1 The Fisher distribution

The Fisher distribution is a probability distribution for the location of a point $\mathbf{V}$ on a unit sphere. (We let points be represented by their position vectors from the centre of the sphere.) The distribution has two parameters, the location parameter $\boldsymbol{\lambda}$, which is a point on the sphere, and the concentration parameter κ, which is a real number. If dS is the area of an infinitesimally small portion of the sphere around a point $\mathbf{v}$ on the sphere, the probability that $\mathbf{V}$ will belong to this portion is

$$\frac{\kappa}{4\pi\sinh\kappa}e^{\kappa\boldsymbol{\lambda}\cdot\mathbf{v}}\,dS. \tag{1}$$

From now on we shall assume that $\boldsymbol{\lambda} = (0, 0, 1)$ for simplicity. The formula then takes the form

$$\frac{\kappa}{4\pi\sinh\kappa}e^{\kappa w}\,dS, \tag{2}$$

where $\mathbf{v} = (u, v, w)$.

The total probability is obtained by integrating Formula 2 around the unit sphere. Let us check that the total probability equals 1. Let $u = \sin\theta\cos\phi$, $v = \sin\theta\sin\phi$, $w = \cos\theta$. We get

$$\begin{aligned}\int_0^\pi\int_0^{2\pi} e^{\kappa\cos\theta}\sin\theta\,d\phi\,d\theta &= 2\pi\left[-\frac{1}{\kappa}e^{\kappa\cos\theta}\right]_0^\pi = -\frac{2\pi}{\kappa}(e^{\kappa\cos\pi} - e^{\kappa\cos 0})\\ &= -\frac{2\pi}{\kappa}(e^{-\kappa} - e^{\kappa}) = \frac{4\pi\sinh\kappa}{\kappa},\end{aligned} \tag{3}$$

which is correct.

The three above formulas, as well as other formulas in this paper, are not valid in the case $\kappa = 0$. E.g., 1 should be substituted for $(\sinh\kappa)/\kappa$ when $\kappa = 0$. In order not to distract the reader (or the author) from the main subject, the case $\kappa = 0$ will normally not be treated specially.

2 A generation method from the literature

The following straightforward method to generate random points with a Fisher distribution on a computer is described in essence on p. 59 in Ref. 1. Because $\mathbf{V}$'s spherical coordinates Θ and Φ are independent random variables, they can be generated independently. Θ and Φ are calculated using the formulas $\Theta = F_\Theta^{-1}(U_\Theta)$ and $\Phi = F_\Phi^{-1}(U_\Phi)$, where F_Θ and F_Φ are the cumulative distribution functions of Θ and Φ, and where U_Θ and U_Φ are independent random numbers uniformly distributed over the interval $(0, 1)$.

There is however a possible disadvantage with this method, as we shall see now.

For simplicity, let us study the case $\kappa = 0$, where the Fisher distribution is equal to a uniform distribution on the sphere. In this case $\Theta = F_\Theta^{-1}(U_\Theta) = \arccos(1 - 2U_\Theta)$ and $\Phi = F_\Phi^{-1}(U_\Phi) = 2\pi U_\Phi$. On a computer U_Θ and U_Φ will be calculated by a random number generator. For numerical reasons U_Θ and U_Φ will have a discrete rather than a continuous distribution. It is realistic to assume that the possible U_Θ and U_Φ values will be closely and more or less evenly spaced numbers in the interval $(0, 1)$. (We shall not dwell on whether the endpoints 0 and 1 are possible values.) The distribution of generated points on the sphere will also be discrete. As the derivative of F_Θ^{-1} is very large near 0 and 1, the points will not be so closely spaced in the θ direction near the poles of the sphere. On the other hand, the points will be very closely spaced in the ϕ direction, as a small change in ϕ corresponds to a much smaller change in location near the poles.

Whether the not-so-close spacing of points in the θ direction near the poles is a disadvantage or not depends on the application in which the generated points are used.

A possible solution to the problem is to calculate U_Θ with a double precision random number generator, if one is available. (We assume then that single precision is used otherwise in the program.) U_Θ's increased resolution will be enough to compensate for the large derivative of F_Θ^{-1} near 0 and 1. I have not tried this solution in a computer program.

3 A generation method developed by the author

In this section another method to generate random points with a Fisher distribution will be described. I developed the method in 1998–1999. I also wrote a subroutine to generate Fisher-distributed random points based on the method. The subroutine has been used at Computer-aided Fluid Engineering AB.

Let $\mathbf{r} = (x, y, z)$ denote an arbitrary point in space, and (unless $x = y = z = 0$) let $\mathbf{v} = (u, v, w)$ be its projection onto the unit sphere defined by $\mathbf{v} = \mathbf{r}/|\mathbf{r}|$. With spherical coordinates r, θ, ϕ we have $x = r \sin\theta \cos\phi$,

$y = r \sin\theta \sin\phi$, $z = r\cos\theta$, and $u = \sin\theta\cos\phi$, $v = \sin\theta\sin\phi$, $w = \cos\theta$.

Let D_1 be the three-dimensional domain consisting of all points $\mathbf{r}$ which satisfy

$$0 < r \le e^{(\kappa w - |\kappa|)/3}. \tag{4}$$

Consider a surface element dS around a point $\mathbf{v}$ on the sphere. The volume of the part of D_1 projected onto dS is

$$\frac{e^{\kappa w - |\kappa|}}{3}\, dS. \tag{5}$$

Let $\mathbf{R}$ be a random point uniformly distributed within D_1, and let $\mathbf{V} = \mathbf{R}/|\mathbf{R}|$ be its projection onto the sphere. Because the volume given by Formula 5 is proportional to the probability given by Formula 2, $\mathbf{V}$ will have a Fisher distribution.

We can generate $\mathbf{R}$ uniformly distributed within D_1 by generating $\mathbf{R}$ uniformly distributed within the larger domain D_2 defined by

$$|x|, |y| \le \sqrt{\frac{2}{1 + \sqrt{1 + (2\kappa/3)^2}}}, \qquad |z| \le 1, \tag{6}$$

and keeping $\mathbf{R}$ only if it is located within D_1. It remains to show (1) that D_1 is a subset of D_2, and (2) that the volume ratio of D_1 to D_2 is large enough that $\mathbf{R}$ can be kept often enough.

As a preparation for showing (1), we shall first calculate $\sin\theta$ for that θ in the interval $0 \le \theta \le \pi$ which maximizes the expression

$$e^{(\kappa\cos\theta - |\kappa|)/3} \sin\theta. \tag{7}$$

As the expression is positive in the interior of the interval and 0 at the endpoints, the maximum must be attained when the derivative is 0.

$$\frac{d}{d\theta}\left(e^{(\kappa\cos\theta - |\kappa|)/3} \sin\theta\right) = 0 \tag{8}$$

$$e^{(\kappa\cos\theta - |\kappa|)/3}\left(\cos\theta - \frac{\kappa}{3}\sin^2\theta\right) = 0 \tag{9}$$

$$\cos\theta = \frac{\kappa}{3}\sin^2\theta \tag{10}$$

$$1 - \sin^2\theta = \left(\frac{\kappa}{3}\right)^2 \sin^4\theta \tag{11}$$

$$\sin^{-4}\theta - \sin^{-2}\theta - \left(\frac{\kappa}{3}\right)^2 = 0 \tag{12}$$

$$\sin^{-2}\theta = \frac{1}{2} (\pm) \sqrt{\frac{1}{4} + \left(\frac{\kappa}{3}\right)^2} \tag{13}$$

$$\sin\theta = \sqrt{\frac{2}{1+\sqrt{1+(2\kappa/3)^2}}} \tag{14}$$

Let θ_0 denote the θ which maximizes Formula 7.

To show (1), we shall show that any point $\mathbf{r}$ belonging to D_1 also belongs to D_2. In other words, we shall show that if $\mathbf{r}$ satisfies Formula 4, then $\mathbf{r}$ also satisfies Formula 6. And this is indeed the case, because if $\mathbf{r}$ satisfies Formula 4, then

$$\begin{aligned} |x|, |y| &\le r\sin\theta \le e^{(\kappa w-|\kappa|)/3}\sin\theta = e^{(\kappa\cos\theta-|\kappa|)/3}\sin\theta \\ &\le e^{(\kappa\cos\theta_0-|\kappa|)/3}\sin\theta_0 \le \sin\theta_0 = \sqrt{\frac{2}{1+\sqrt{1+(2\kappa/3)^2}}} \end{aligned} \tag{15}$$

and

$$|z| \le r \le e^{(\kappa w-|\kappa|)/3} \le 1. \tag{16}$$

To show (2), let us first calculate the volumes of D_1 and D_2. We obtain the volume of D_1 by integrating Formula 5 around the unit sphere and using Formula 3. The volume is

$$\begin{aligned} \int_0^{\pi}\int_0^{2\pi} \frac{e^{\kappa\cos\theta-|\kappa|}}{3}\sin\theta\, d\phi\, d\theta &= \frac{e^{-|\kappa|}}{3}\int_0^{\pi}\int_0^{2\pi} e^{\kappa\cos\theta}\sin\theta\, d\phi\, d\theta \\ &= \frac{e^{-|\kappa|}}{3}\cdot\frac{4\pi\sinh\kappa}{\kappa} = \frac{e^{-|\kappa|}}{3}\cdot\frac{4\pi\sinh|\kappa|}{|\kappa|} = \frac{2\pi(1-e^{-2|\kappa|})}{3|\kappa|}. \end{aligned} \tag{17}$$

From Formula 6 the volume of D_2 is found to be

$$\frac{16}{1+\sqrt{1+(2\kappa/3)^2}}. \tag{18}$$

The following inequality shows that the volume ratio of D_1 to D_2 is greater than $\pi/36$ for all κ.

$$\begin{aligned} \frac{2\pi(1-e^{-2|\kappa|})}{3|\kappa|} \bigg/ \frac{16}{1+\sqrt{1+(2\kappa/3)^2}} &= \frac{\pi(1-e^{-2|\kappa|})(1+\sqrt{1+(2\kappa/3)^2})}{24|\kappa|} \\ > \frac{\pi(1-e^{-2|\kappa|})(1+2|\kappa|/3)}{24|\kappa|} &= \frac{\pi[(1+2|\kappa|/3)-(1+2|\kappa|/3)/e^{2|\kappa|}]}{24|\kappa|} \\ &> \frac{\pi[(1+2|\kappa|/3)-1]}{24|\kappa|} = \frac{\pi}{36} \end{aligned} \tag{19}$$

It is easy to show that the volume ratio equals $\pi/6$ when $\kappa = 0$, and that it approaches $\pi/36$ when $\kappa \to \pm\infty$. The volume ratio therefore varies with κ, but it is always greater than $\pi/36$. We have thus shown (2).

Let us summarize the method to generate Fisher-distributed random points described in this section. Generate three random numbers uniformly distributed e.g. over $(0, 1)$. Calculate from these numbers a random point $\mathbf{R}$ uniformly distributed within D_2, which is defined by Formula 6. If $\mathbf{R}$ belongs to D_1, defined by Formula 4, keep it, otherwise discard it and repeat the process until an $\mathbf{R}$ belonging to D_1 has been found. Calculate $\mathbf{V} = \mathbf{R}/|\mathbf{R}|$. $\mathbf{V}$ is then our random point with a Fisher distribution.

It is evident that the method described in this section does not have the possible disadvantage of the method in Section 2. As long as $|\kappa|$ is not large, the method should work well from all reasonable aspects (possibly except for speed). To be specific, I think that the method should work well at least for $|\kappa| < 20$ or so. (The choice of 20 as the limit will not be explained here.) I am not sure how well the method works numerically for larger $|\kappa|$.

Reference

1. N. I. Fisher, T. Lewis, B. J. J. Embleton. *Statistical analysis of spherical data.* First paperback edition. Cambridge university press, Cambridge, 1993.

Appendix E

Deriving estimates of the flow wetted surface in DarcyTools

E.1 Introduction

A substance dissolved in water (hereafter called a tracer) can be transported through a rock volume, provided there is a system of connected fractures and a flow through these. The tracer may enter crossing fractures, with or without a flow, and may also diffuse into the rock matrix. The strength of the diffusive process is related to the flow rate and the flow wetted surface (to be defined below) as it is through this surface matrix diffusion and diffusion into smaller fractures take place.

An up to date review of how the flow wetted surface (FWS) can be derived or estimated is given by Andersson et al. (1998) and there is hence no need to give an extensive background here. An account of how the FWS is derived in Discrete Fracture Network (DFN) models is given by Outters and Shuttle (2000).

The present analysis will be concerned with how the FWS can be derived in the stochastic continuum model DarcyTools. In DarcyTools the rock volume is divided into a regular system of computational cells and the key question is hence how the FWS can be estimated for such a cell. In Figure E-1 the situation is illustrated, schematically. If, as an illustration, we assume that the cell has the dimensions 1×1×1 m^3, the channel shown may have a surface area of 1×0.5 m^2. The FWS would then be 1 m^2, as an exposed area is found on both sides of the channel. It is clear from this illustration that the FWS can not be much larger than 2 m^2/m^3, if the simple channel model with two bounding surfaces is accepted. However, the surface may be very irregular and may also comprise parallel channels and the upper limit of 2 m^2/m^3 is hence only a "rough guide".

When a tracer travels through the channel illustrated in Figure E-1, it may exchange matter by diffusion with the rock volume exposed by the FWS. The significance of this exchange can be expected to be related to two parameters: the FWS per unit volume of water in the channel, a_w, and the residence time, t. The exchange will increase with both these parameters and a new variable the F-quotient (Andersson et al. 1998) has been introduced for this product:

$$F = a_w \times t \tag{E-1}$$

By simple algebra it is possible to write Equation E-1 as:

$$F = a_r L/q$$

where L is the cell dimension, a_r the FWS per unit rock volume and q the Darcy velocity. The present report will mainly be concerned with a_r and F, determined locally for a cell or integrated along a flow channel.

The objective of this appendix is hence to demonstrate how the FWS and F- quotient can be determined in DarcyTools.

E.2 Evaluated methods

Three different ways of calculating the FWS, for a computational cell, in DarcyTools will be investigated; these will now be described.

E.2.1 Gehyco method

The general method used in DarcyTools to derive hydraulic properties is called GEHYCO (GEneral HYdraulic COnditions). The central idea is to calculate "how much of a conductive element that intersects a computational cell and let that volume generate a contribution to the cell property in question". A full account of this method can be found in Svensson (2001b).

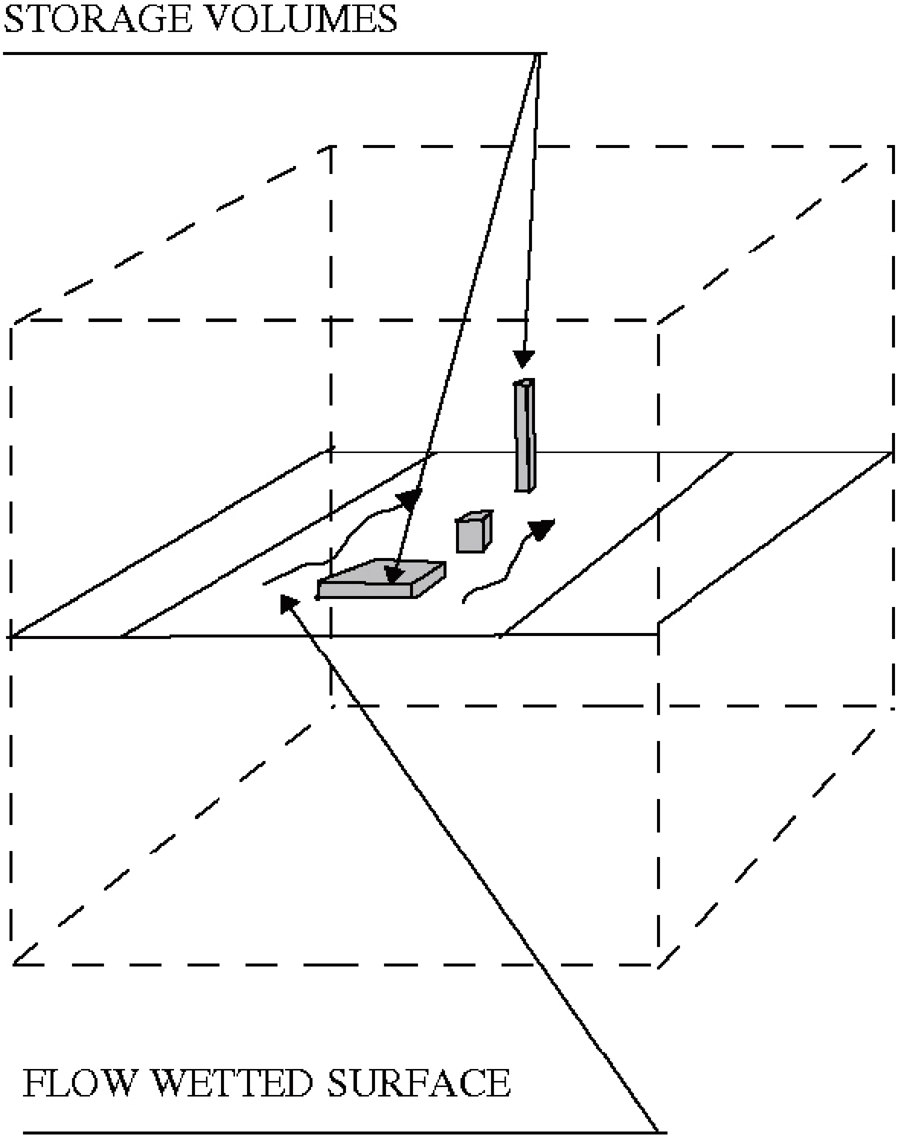

Figure E-1. Illustration of a computational cell with a channel with flow.

It is also possible to determine how much of a fracture surface that intersects a cell and let this "intersecting surface" give a contribution to the FWS in the cell. This method is hence conceptually straight forward and does not involve any further assumptions than those involved in the specification and generation of the fracture network.

E.2.2 P_{32} Method

When the background fracture network is generated, a power law distribution is assumed for the intensity, i.e. number of fractures in a size interval per unit volume. It is straight forward to use this power law to calculate the expected number of fractures for a number of length intervals and hence obtain the total surface area per unit volume, P_{32}.

In Table E-1 the contributions from different size groups are given together with the total area P_{32}. As can be seen, fractures down to a length-scale of three metres are assumed to contribute to P_{32}. The reason for choosing three metres as the lower limit, is that the cell size in the model simulations to be presented is three metres; the assumption being that all flow channels are picked up by the fracture network and grid chosen.

When the global P_{32} has been determined, we need to distribute the surface to each cell. This is done with the kinematic porosity as a weighting factor, as cell porosity values are available from GEHYCO. Finally we note that the local a_r value is twice the local P_{32} value. An underlying assumption of this method is that the local a_r-value is directly proportional to the local kinematic porosity; this is no more than an assumption.

Table E-1. Estimate of global P_{32} value from a power law for fracture intensity. The Laboratory scale model (Svensson 1999b) is used for the estimates.

Fracture set	Length interval [m]	Number, excluding isolated fractures	P_{32}	ΣP_{32}
Determ zones			0.014	0.014
1	160–320	12	0.004	0.018
2	80–160	70	0.004	0.022
3	40–80	425	0.007	0.029
4	20–40	2,050	0.008	0.037
5	10–20	9,150	0.009	0.046
6	5–10	38,800	0.008	0.054
7	3–5	95,600	0.006	0.060
				0.06

E.2.3 Aperture method

The third method to be evaluated derives the FWS by the following steps:

- A conductivity is available at each of the six cell walls.
- A transmissivity can be obtained by multiplying with the cell dimension, Δ.
- Use the relation between transport aperture and transmissivity ($e_T = 2.0T^{0.6}$) presented in Appendix H to calculate e_T, based on six cell wall values.
- The free volume in the cell is given by $\theta_k\Delta^3$, where θ_k is the kinematic porosity, and the area can hence be calculated as:

$$a_r = 2.0\frac{\theta_k \Delta^3}{e_T} \tag{E-2}$$

The method apparently involves a number of assumptions that can not easily be evaluated.

E.3 Results

In the evaluation of the methods a slightly modified version of the Laboratory scale model (Svensson 1999b) will be used. One modification is that the cell size is put to 3 metres (instead of 5 metres) and another that only a simple forcing (flow from west to east) will be used. The Äspö HRL is not included in the model and all flow channels will hence start at the western boundary and leave through the eastern one.

E.3.1 FWS values in cells

We start by discussing the global mean values of a_r, see Table E-2, and the corresponding histograms, see Figure E-2. Starting with the mean values, it is clear that all three estimates are in fair agreement and are also in agreement with the mean value of 0.1 m^2/m^3 suggested by Andersson et al. (1998). The distributions are however different, as can be seen in the histograms, see Figure E-2.

First it should be explained that the bar $0.5–1.0\times10^{-2}$ represents all cells with an a_r less than 10^{-2} m^2/m^3. Roughly two thirds of all cells have a very small a_r. This is due to the fact that the same fraction of cells is not intersected by any fracture and hence get zero porosity and zero a_r. From the histograms one may also note that all three methods generate most "active" a_r-values in the two intervals 0.1→0.5 and 0.5→0.1. It is also worth noting that method three (aperture based) generates very few cells with an a_r-value greater than 1.0.

E.3.2 FWS values along flow channels

The global a_r-values are not of much relevance, as it is the FWS along flow channels that will affect the exchange with the rock matrix. For this reason we will study the correlation between the cell Darcy velocity and cell a_r-value, for the simple flow situation described above, see Figure E-3. At a first glance the result may look rather similar for the three methods; a closer examination reveals however some interesting differences:

- Method three shows a week correlation between the Darcy velocity, q, and a_r. If a_r does not increase with q this implies that e_T increases with q, as a larger q should be correlated with a larger "channel cross section area".
- Method two shows a linear increase of a_r with q. The interpretation of this behaviour is that "a doubling of q doubles the width of the channel, with e_T kept constant".
- Method one can be viewed as being in between these two extremes and perhaps be interpreted as "increased q is correlated with an increase in both width and aperture of the channel".

A tentative conclusion is that method one is the more realistic one, from this point of view.

Next we study the variation of a_r along a streamtube. This requires that flow paths are calculated. In DarcyTools this is carried out in the submodel PARTRACK (Svensson 2001a). In the west to east flow considered, particles are released in fracture zone EW1, see Figure 1-2, and then tracked through the domain till they reach the eastern boundary. Figure E-4 shows the flow paths generated by 100 particles. The main flow path is through EW1, changing to the NNW structures and leaving through NE1. Note that in this view from above, NE1 gives a wider impression as this zone is not vertical. It is also worth noting that rather few flow channels are active in the transport.

Figure E-5 shows the variation of a_r for one flow path. The same trends as in Figure E-3 can be identified, i.e. method three generates a fairly constant a_r, method two shows the largest variations and method one is somewhere in between.

E.3.3 F-quotients along flow channels

Figure E-6 shows the variation of the cell F-quotients (Fi = $a_{r,\,i}\,\Delta/q_i$) along a flow path. The same differences between the methods as for a_r can be expected, but the implications for the F-quotients are a little bit different:

- In method three a_r is fairly constant and this is probably the reason for the rather small variation seen in this figure.
- Method two was found to give a correlation between a_r and q. It is hence not surprising that the F-quotient is fairly constant for long periods.
- Method one has a weaker correlation between a_r and q and hence shows a larger variability.

In Outters and Shuttle (2000) the integrated F-quotient along a flow path versus time was analysed. In that report also a curve was fitted to the results from the numerical model. Here, this curve will be used for comparisons with the three methods analysed in the present report. The F-quotient was hence summed up along a flow path; this was done for one hundred particles and the result can be studied in Figure E-7. The following should be noted:

- All results are in fair agreement with Outters and Shuttle (2000) (straight line in the figures). The fact that the present results are generally below the straight line can be explained by a somewhat higher P_{32}-value used in the model by Outters and Shuttle. Method three, which has the highest average a_r, is closest to the straight line.
- Method two, which has a strong correlation between a_r and q, gives the smallest spread around the mean value.

Table E-2. Global mean values of a_r for the three methods evaluated.

	Method		
	GEHYCO	**P_{32}**	**Aperture**
a_r (m^2/m^3)	0.12	0.13	0.18

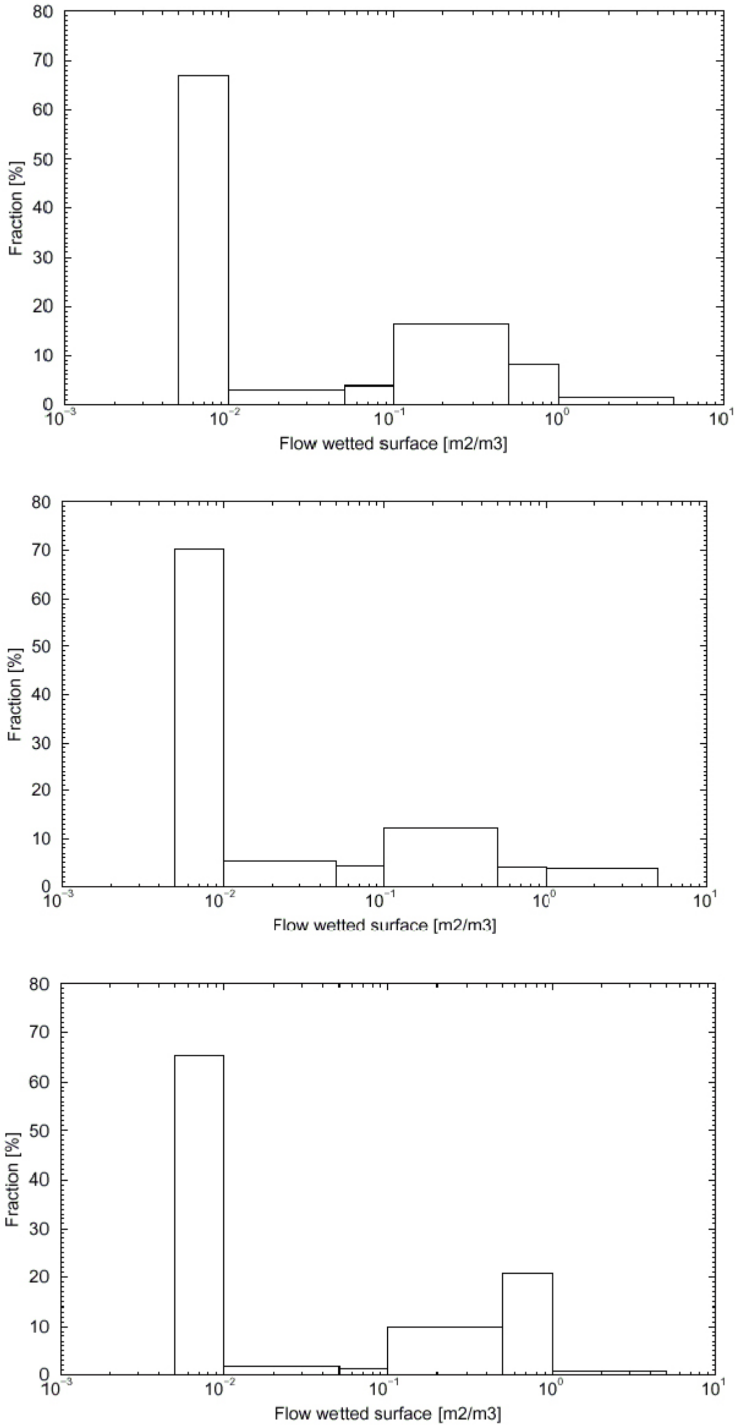

Figure E-2. Histograms of a_r [m^2/m^3]. Method one (top), two (middle) and three (bottom).

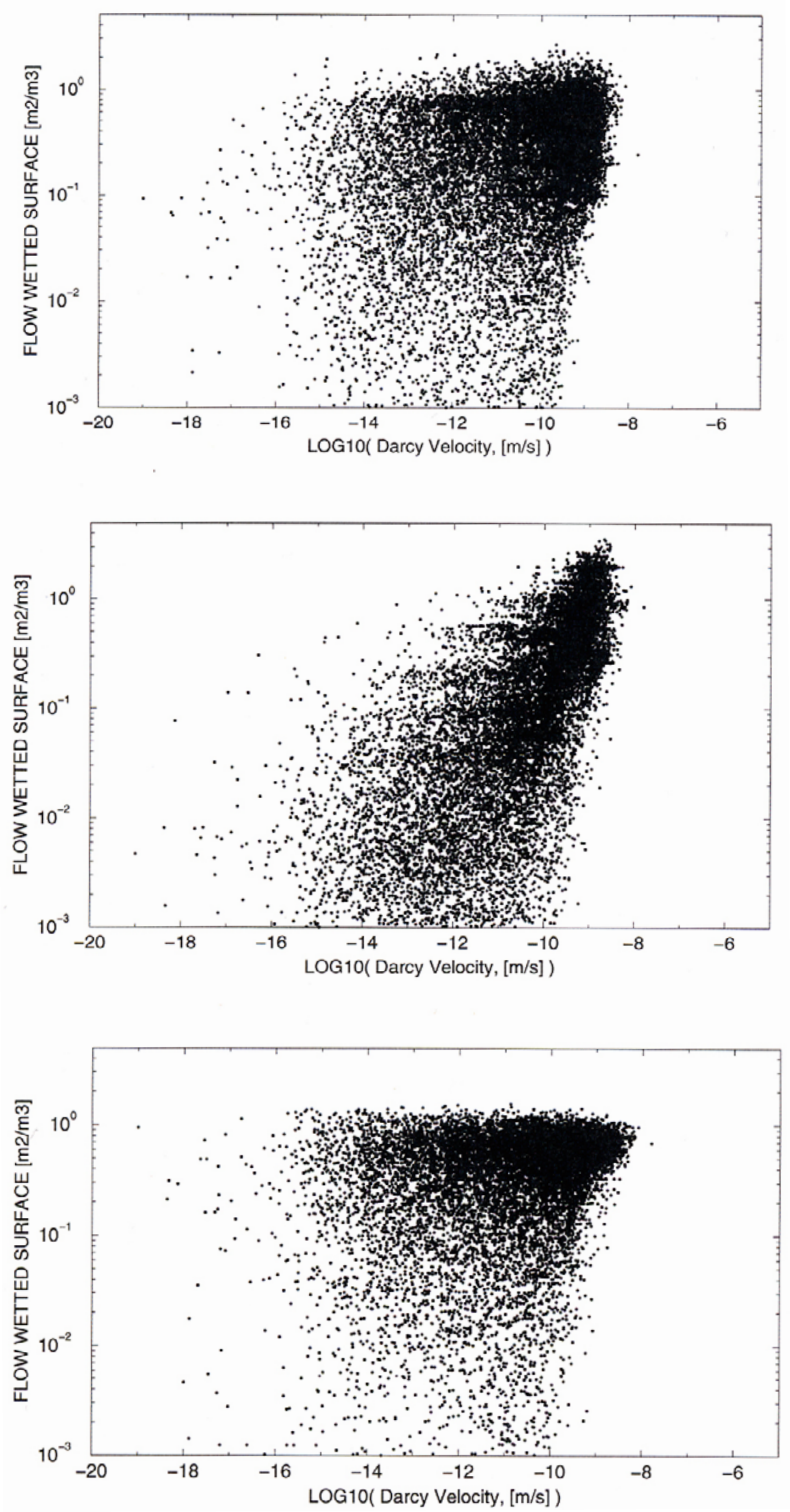

Figure E-3. *Correlation between flow wetted surface a_r, and Darcy velocity, q. Method one (top), two (middle) and three (bottom).*

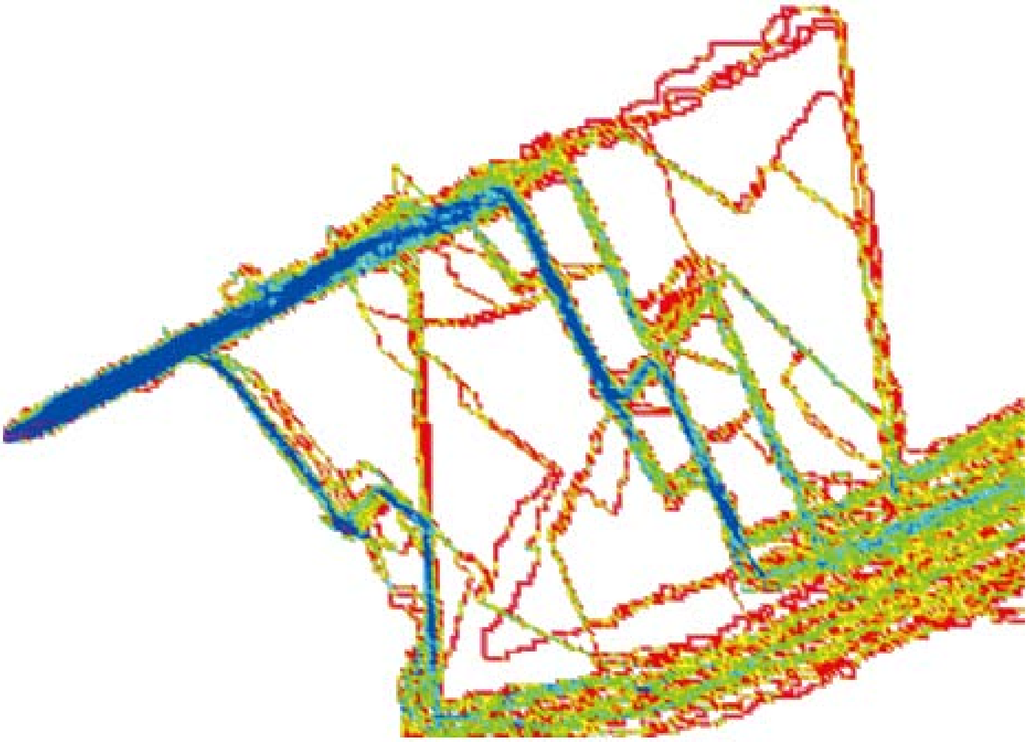

Figure E-4. *Flow channels formed by 100 particle tracks in a flow from west to east. Blue indicates high intensity of tracks, red low.*

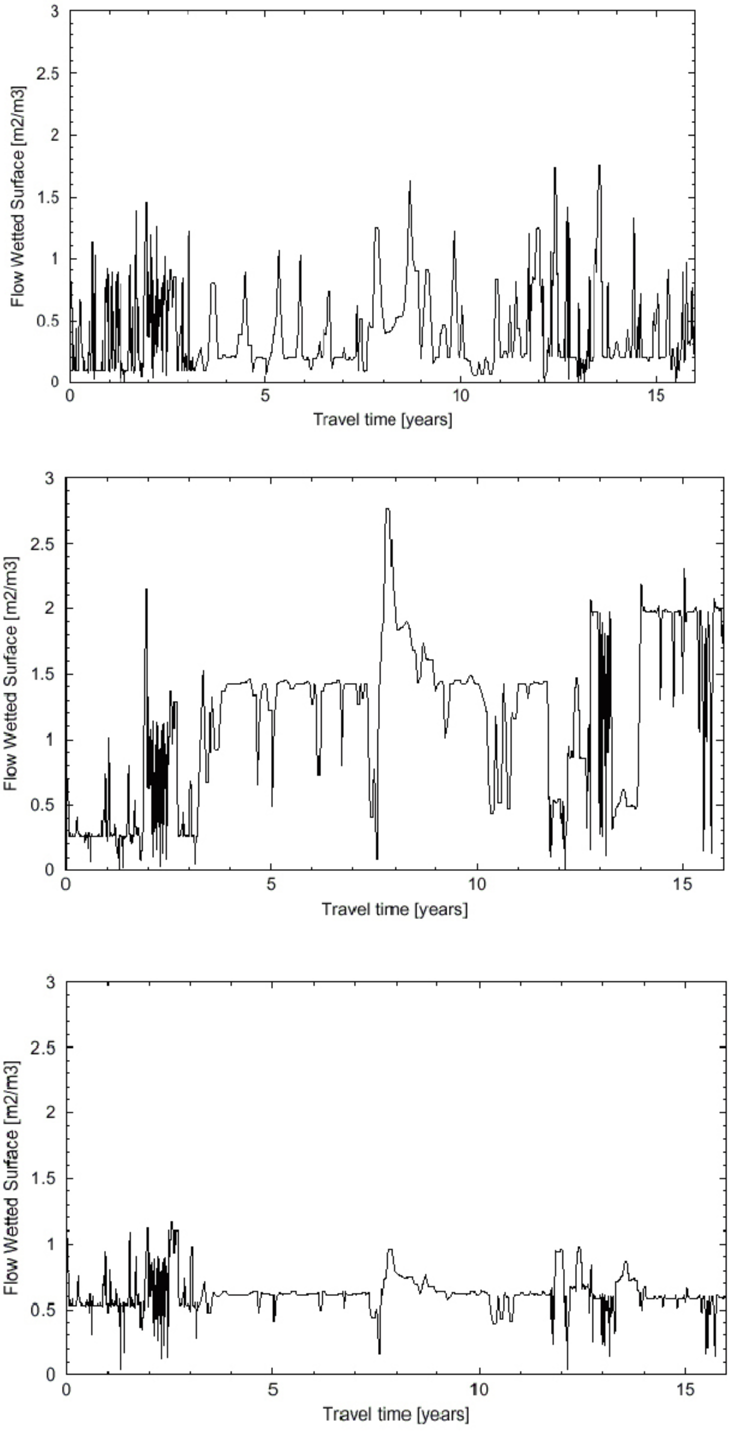

Figure E-5. *Variation of a_r along a single flow path. Method one (top), two (middle) and three (bottom).*

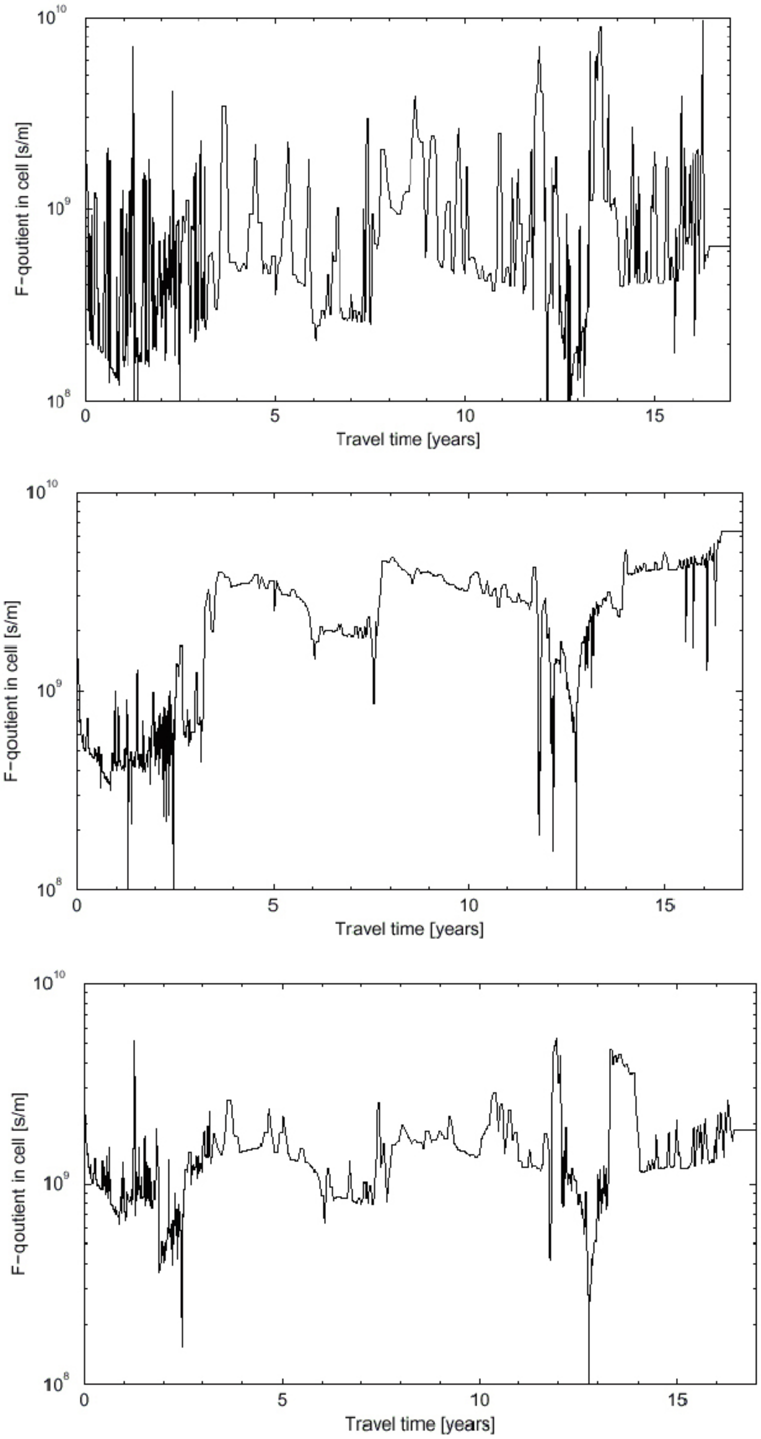

Figure E-6. *F-quotients along a flow path. Method one (top), two (middle) and three (bottom).*

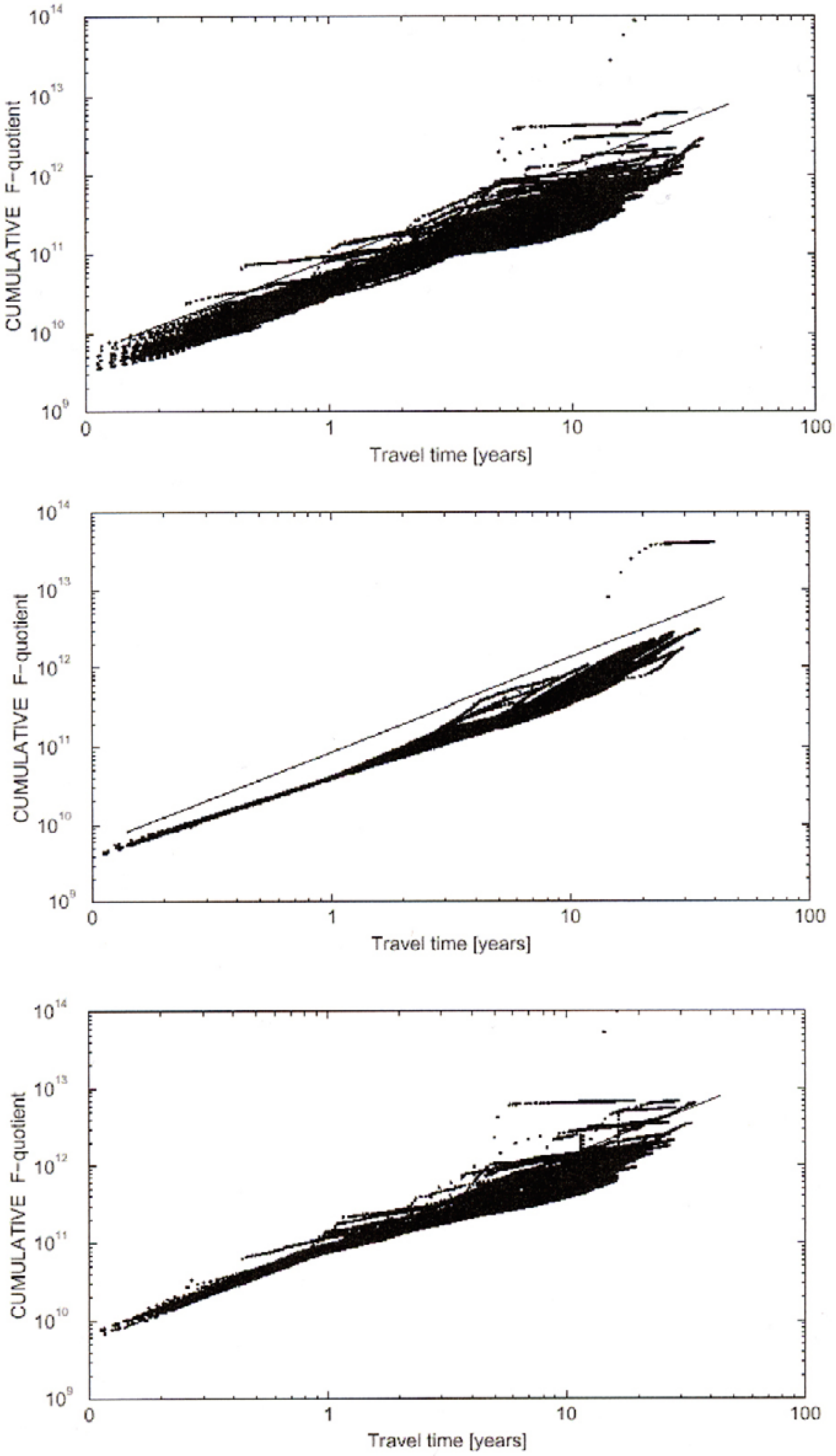

Figure E-7. *Integrated F-quotients along flow paths. Straight line gives the result from Outters and Shuttle (2000). Method one (top), two (middle) and three (bottom).*

E.4 Discussion and conclusions

The present analysis assumes that all fractures and fracture zones have a simple geometric shape, i.e. the bounding surfaces are two parallel planes. This is of course a gross simplification that needs to be taken into account when the results are evaluated. The following points should also be considered:

- The a_r values determined give *all* the surface area in a cell. It may well be the case that only a fraction of this area is in direct contact with the flowing water.
- On the other hand, a real fracture is not made up of two parallel planes, but may be highly irregular, which increases the possibly active surface (as compared to the assumptions made in this report).
- A steady flow field was used in the present analysis. In reality one may expect transient "pulses" on a variety of times scales; from tidal effects, yearly groundwater level variations to periods with an inland ice on the very long time scale. These transients may disperse a tracer within a fracture plane and also activate fractures that otherwise could not be reached by the tracer. A larger flow wetted surface would hence be the result.

The a_r-values derived should hence more be considered as index of a flow wetted surface, rather than an absolute estimate of the magnitude.

In Andersson et al. (1998) four topics are suggested, as having the potential to improve our understanding of the flow related migration parameters:

- develop the theoretical understanding of migration and matrix diffusion,
- study the effect of diffusion into stagnant or low flow zones in a single fracture,
- migration modelling directly in the flow codes,
- exploring for further evidence of matrix diffusion from tracer tests, static diffusion tests, geology and geochemistry.

This project has not been focused on these suggestions, but it may be the case that DarcyTools, with the features introduced in this report (FRAME and FWS-derivations), goes some way towards these goals. Presently PA-studies use global estimates of FWS in estimates of the F-quotients. It is possible to get some perspective on these estimates from the present study. In Figure E-8, the integrated F-quotients for 100 particles using two methods are compared. In one of the methods we use the global estimate of a_r, while the other method use the local cell values. If the two methods were giving equal results, the points should fall on the straight line in Figure E-8. This is not the case, the method using local cell values gives a significantly larger variation of F-quotients.

With the precautions mentioned above in mind, the following conclusions from the study are formulated:

- Three partly independent methods to estimate the flow wetted surface from the groundwater code DarcyTools have been evaluated. All three methods give global estimates of a_r that are in fair agreement and these are also in agreement with the expected value for the Äspö HRL (Andersson et al. 1998).
- Method one, which is based on the GEHYCO technique, is considered to be the best choice as it directly calculates a_r from the fracture network without any additional assumptions.

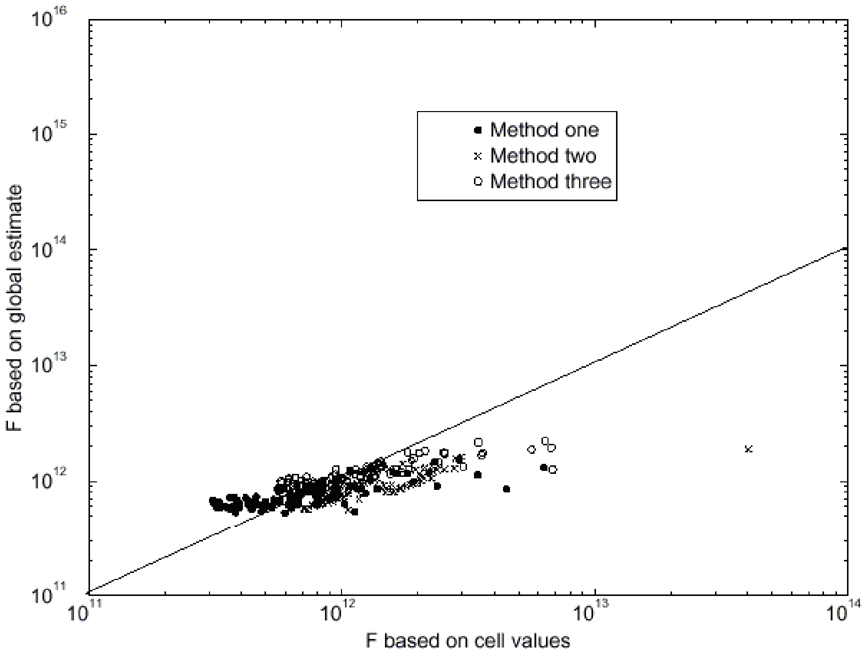

Figure E-8. *F-quotients determined with local and global FWS values.*

Appendix F

Empirical relations for the determination of fracture properties

F.1 Introduction

It is necessary to specify the properties of the conductive elements, even if some of the required information is uncertain or unknown.

The relations to be presented are not claimed to be the "best possible input data", but merely represent what is presently available (a more complete compilation is needed).

F.2 Transmissivity-fracture size

The following relation was found in a calibration study for the laboratory domain considered also in this report (see Report 2):

$$T = \begin{cases} 10^{-5}(l/100)^2 & [m^2/s] \text{ for } l \leq 100 \text{ metres} \\ 10^{-5} & [m^2/s] \text{ for } l > 100 \text{ metres} \end{cases} \qquad \text{(F-1)}$$

This relation is shown in Figure F-1 (labelled LABM (99)) together with data from field investigations (Äspö Major zones, Prototype Repository, TRUE Feature A, TRUE Block Scale) and some mean values from simulation models (DFN Aberg, DFN TRUE Block Scale). As already mentioned, the compilation is far from complete and we will restrain from any firm statements. However, relation (F-1) does not seem to contradict the information compiled.

F.3 Transmissivity-transport aperture

The transport aperture, e_T, will be used to calculate the kinematic porosity of a conductive element. In Figure F-2 one experimental curve (Rhén et al. 1997), one curve used in other models (Doe 1993. Unpublished manuscript referenced by Dershowitz et al. 1999) and the relation resulting from the cubic law are shown. The solid line is given by:

$$e_T = 2.0T^{0.6} \qquad \text{(F-2)}$$

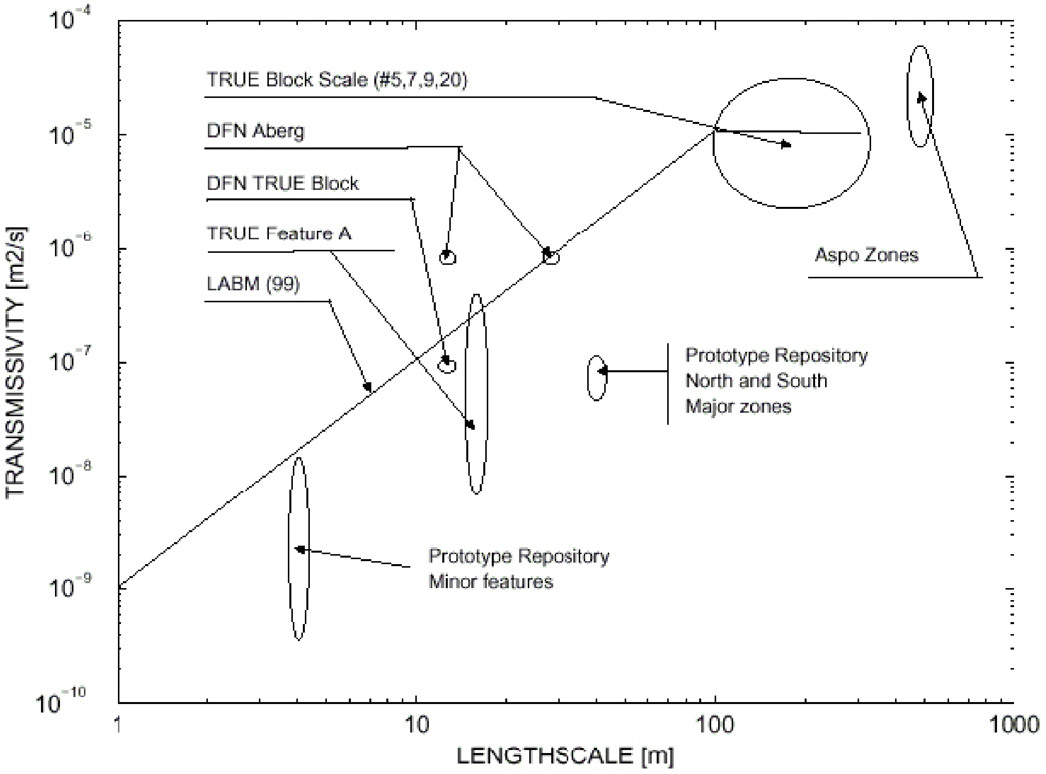

***Figure F-1.** Relation between fracture size and transmissivity.*

Compiled data:

- *TRUE BLOCK fractures* (#5, 7, 9, 20) *(Winberg 1998).*
- *TRUE Feature A (Winberg et al. 2000).*
- *Äspö. Major fracture zones NNW* (Rhén et al. 1997).*
- *Prototype Repository. South and North major zones and minor zones (Forsmark and Rhén, 1999).*
- *DFN, Aberg (Dershowitz et al. 1999).*
- *DFN, TRUE Block Scale (Winberg 2000).*

This relation is regarded as a good compromise, based on the following arguments:

- The curve by Rhén et al. (1997) is mainly based on fracture zones with relatively high transmissivity.
- The curve by Doe (1993) is mostly used for transmissivities in the range $10^{-7} \rightarrow 10^{-5}$ m^2/s.
- The cubic law applies to "single opening fractures" and is hence best suited for small transmissivities.

It should once again be pointed out that the only purpose of this compilation is to show that the relation used, Equation F-2, is in fair agreement with some easily compiled information.

Fracture size-thickness

It will be assumed that fractures are squares with dimension $L \times L$ m^2 and that the fracture thickness, b, is 1% of the fracture length scale, L. Field data from Äspö, (see Figure F-3), do not seem to contradict this relation. The definition of "fracture thickness" is given in Section 3.3.

Diffusion coefficients

Effective molecular diffusion in a conductive element should be proportional to the product of the kinematic porosity and the diffusivity value in the pore water (Neretnieks 1993). The proportionality constant is related to the properties of the pore space (constrictivity and tortuosity).

In DarcyTools, we will simply assume that the diffusion coefficient for a conductive element is equal to the product of the kinematic porosity and the diffusion value in pure water.

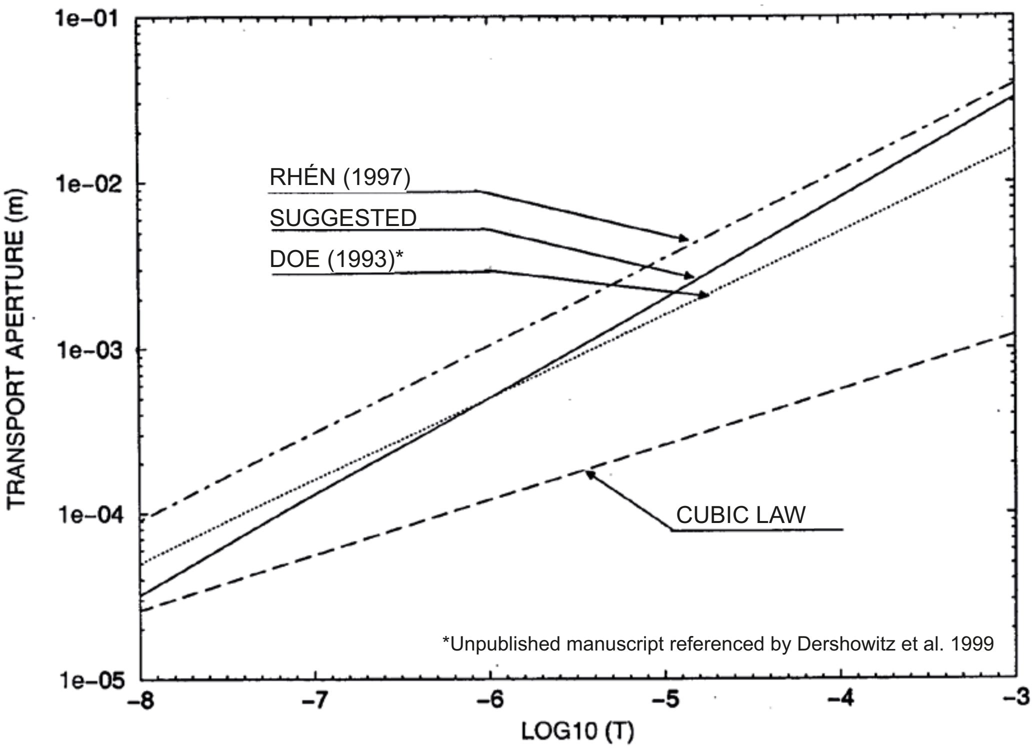

Figure F-2. *Relation between fracture transmissivity and transport aperture.*

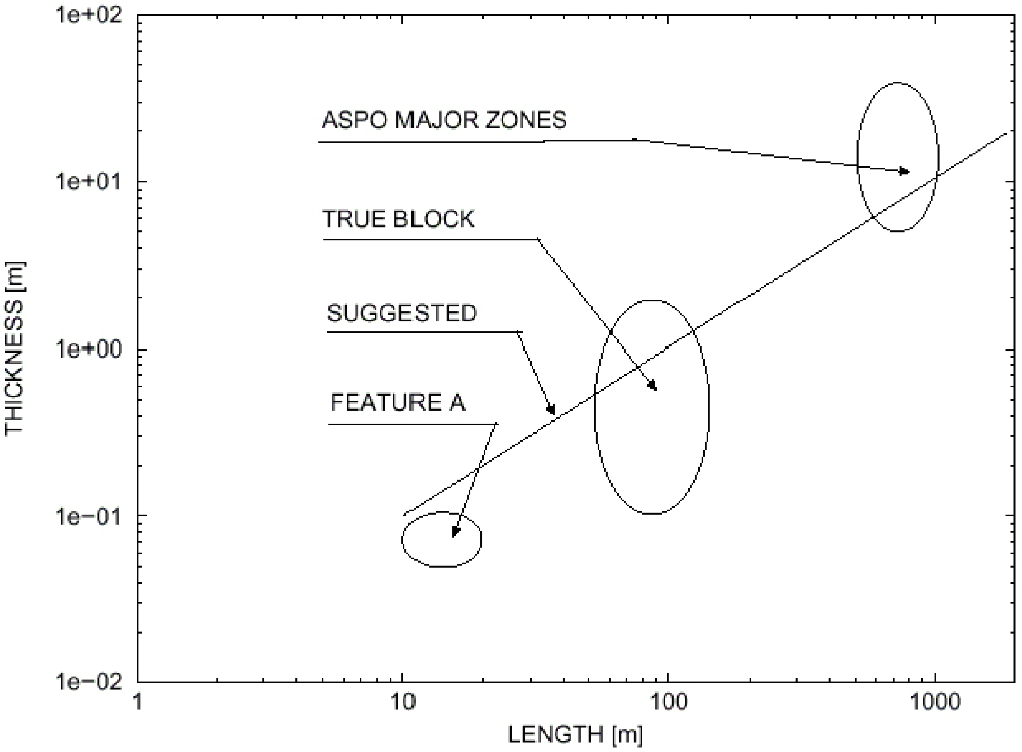

Figure F-3. *Relation between fracture thickness and length.*

Compiled data:

- *Äspö (zones NNW*) (Rhén et al. 1997).*
- *TRUE BLOCK (Winberg 1998).*
- *Feature A (Winberg et al. 2000).*

Appendix G

Some simple calculations illustrating the GEHYCO method

G.1 Some simple calculations illustrating the GEHYCO method

Calculations (which can be done without a computer) for a 2D case will be presented, with the objective to illustrate the basic idea of GEHYCO. The case to be discussed concerns a conductive element that runs at an angle of 45° to the coordinate directions and has a thickness, b_e, comparable to the grid size, Δ, see Figure G-1. The exact flux, Q_a, from cell centre (2, 2) to cell centre (3, 3) is given by:

$$Q_a = K_e b_e \frac{dh}{\sqrt{2}\Delta} \tag{G-1}$$

where K_e is the element conductivity and dh the head difference. In the grid representation there will be two flow paths between the points in question. The velocity cell conductivity, K_c, is calculated as the "element conductivity times the intersecting volume divided by the cell volume" according to the basic principle of the method, thus:

$$K_c = K_e \frac{\sqrt{2}\Delta b_e}{2\Delta^2} = K_e \frac{b_e\sqrt{2}}{2\Delta} \tag{G-2}$$

for both the velocity cell between (2, 2) and (3, 2) and the cell between (3, 2) and (3, 3). The head gradient from point (2, 2) to (3, 2) is thus $dh/2\Delta$. We can now formulate the flux, as represented in the grid, as:

$$Q_c = K_e \frac{b_e\sqrt{2}\Delta}{2\Delta}\frac{dh}{2\Delta} = \frac{K_e b_e}{2}\frac{dh}{\sqrt{2}\Delta} \tag{G-3}$$

As we have two flow paths between the points, it is found that the grid representation gives the same flux as the exact solution.

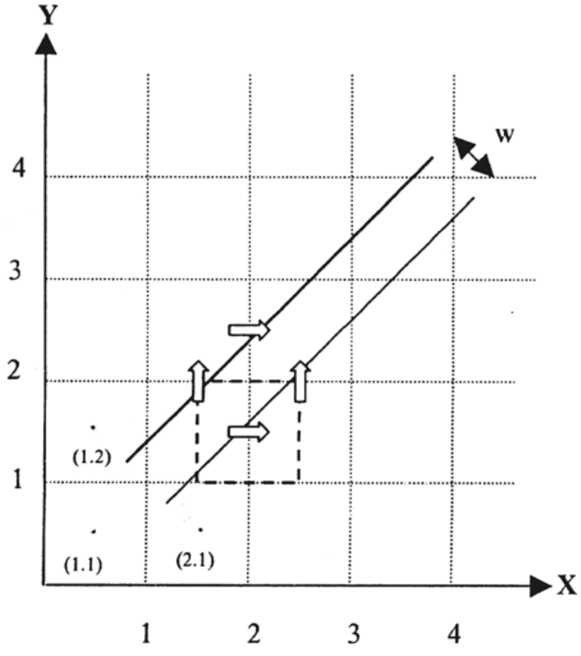

Figure G-1. Illustration of how flow and transport is simulated on the grid.

Next we consider the transport time between the two points in question. Analytically it is easily calculated as the distance divided by the pore velocity:

$$t = \frac{\sqrt{2}\Delta}{U_D / n_e} = \frac{\theta_e \Delta \sqrt{2}}{K_e \dfrac{dh}{\sqrt{2}\Delta}} = \frac{2\theta_e \Delta^2}{K_e dh} \tag{G-4}$$

where t is the transport time, U_D the Darcy velocity and θ_e the kinematic porosity. When estimating the transport time in the grid representation of the element, it is instructive to think of a particle that travels the distance. If we further accept that the residence time of the particle in a cell is equal to the free volume of the cell divided by the flow rate through the cell, the following calculations can be carried out. First one should note that the particle has to move through the grid in the "staggered arrangement", i.e. from (2,2) to (3,2), or (2,3), and then to (3,3). The two pathways have the same transport time and we only need to consider one of them. The two cells in question (2,2) and (3,2) have however different free volumes and through flows and we need to calculate the residence time for each and add the times.

Cell (2,2): $t_{2,2} = \dfrac{\theta_e V_i}{Q}$ (G-5)

Where V_i is the intersecting volume and Q is the flow rate through cell (2.2). After some algebra it is found that:

$$t_{2,2} = \frac{\sqrt{2}}{2} \frac{\theta_e \Delta}{K_e dh} \left(2\sqrt{2}\Delta - b_e \right) \tag{G-6}$$

Cell (3,2): By the same procedure it is found that:

$$t_{3,2} = \frac{\sqrt{2}}{2} \frac{\theta_e \Delta}{K_e dh} b_e \tag{G-7}$$

By adding these two residence times, it is found that the transport time in the grid representation is equal to the analytical solution (Equation G-4).

Diffusive transport can be regarded as a combination of the two cases, flow and transport, discussed. First one should note that the diffusive flux is analogue to the Darcy flux, if the head gradient is replaced by the concentration gradient and the conductivity by the diffusion coefficient. It is clear that diffusion coefficients thus need to be evaluated at cell walls. If the diffusive term is part of an advection/diffusion equation for a scalar, we should evaluate the balance equation for a scalar control volume, see Figure 3-3. It is thus the free volume of the scalar cell, discussed already, that is affected by the fluxes at the cell walls. Hence, solving an advection/diffusion equation for a scalar quantity, does not require any new elements in the grid representation.

The calculations presented intend to illustrate how the properties of the conductive elements are represented in the grid. It is of course reassuring that the method gives correct result for the simple case studied, but it is not a proof that the method is exact. In fact, see Svensson (1999a, 2001), it is well established that some fracture orientations, in relation to the grid, give an error in the simulated flow and transport times. This error has also been found to depend on the thickness of the element in relation to the grid size (b_e/Δ). Estimating this error is one of the main issues in the verification studies, see Report 2.

Appendix H

Parallel DarcyTools

H.1 Introduction

From Version 3.4, DarcyTools implements a domain decomposition technique for parallel runs on multi-core shared memory computers and distributed memory clusters. The technique consists in decomposing the domain into several blocks and allocating one process per block. For users ease, none of the existing CIF command has been modified and new capabilities have been gathered into a single new command named <blockgen>. This command is for partitioning the domain grid into blocks, for partitioning the initialization files according to the domain decomposition and for merging output files for post-processing.

blockgen

The <blockgen> command is considered only by the new BlockGeN program (BGN). The first argument <nblocks> sets the number of blocks for grid or file partitioning and for file merging. The <gridpart> argument then specifies whether BGN will generate block grids from the original domain or will consider that the block grids already exists and simply have to be read. The <binary> argument fixes the type of output file format. When set to true, output files are formatted. When set to false, output files are unformatted. The <tecplot> argument refers to a <tecplot> command name for outputting grids similarly to the <gridgen> command. The <load> argument is for grid partitioning only and fixes the percentage of the total domain cells that a block must contain. This argument is ignored when the <partfile> argument exists and sets the file name of a user defined partition. Finally the <partition> and <merge> arguments can be used to specify names of files to be partitioned or merged according to the grid partitioning.

```
<blockgen>
  <nblocks>   : number of blocks               [1=]
  <load>      : block id, load in percent      [0+]
  <partfile>  : user partition file name       [1-] (default='')
  <tecplot>   : tecplot name                   [1-] (default='')
  <binary>    : grid output files format       [1-] (default=T)
  <gridpart>  : grid partitioning              [1-] (default=T)
  <partition> : file to partition              [0+] (default='')
  <merge>     : file to merge (no #xxx suffix) [0+] (default='')
```

H.2 Grid partitioning

The BGN program reads the grid file defined by the <run> command (xyz by default) and partitions the grid into N (set by <nblocks>) blocks ready for N processes. N+1 new grid files are created and named by adding the '#xxx' suffix to the original grid file name (for instance xyz#0, xyz#1, xyz#2 for 2 blocks generated from the file xyz). The xyz#0 file contains a redundant grid made of the top boundary cells i.e. cells of the land and sea locations. The xyz#nnnn files contain the grid for blocks 1 to N.

Besides the new grid files, N block files are also created with names following the 'blk#nnnn' pattern. Those files contain the additional information necessary for connecting blocks. Users shouldn't care about their content.

When specifying a TECPLOT output file, the BGN program generates N Tecplot files with the '#nnnn' suffix (when the name of the tecplot file terminates with .plt, the suffix is inserted before .plt). Every Tecplot file outputs the same information (grid, locations and cellmk) but is restricted to its block only. To gather the global view users simply have to load files using the TECPLOT program.

Partitioning

By default, DarcyTools implements a Hilbert space-filling curves technique to take advantage of the Cartesian structure of the grid. Given a list of cells in the original domain, a space-filling curve is built that passes through each cell once. The map is constructed so that cells that are close in 3D space remain close when mapped. Thus the curve preserves locality.

A space-filling curve on a simple Cartesian mesh is shown in Figure 1. Once the curve is constructed, the decomposition domain is performed by dividing it into N subintervals, where N is the desired number of processor. The length of any subinterval can be specified by the <load> argument of the <blockgen> command, in term of percentage of the total length. When only some of the blocks have an associated load, the remaining amount of cells is equally distributed among free blocks.

For a better load balancing, one can use the <partfile> argument of the <blockgen> command to specify the name of a specific partition file. Partition files contain the block ID for each cell of the original grid according to the following format:

```
write(iunit,*) '#BG#V300'
write(iunit,*) nbcells
write(iunit,*) (iblock(i),i=1,nbcells)
```

When iblock(i) is smaller than 1, BGN automatically allocates the cell to additional blocks. In that way one can specify all blocks from 1 to NBLOCKS or can specify only some of them and let the program use the space filling technique for remaining cells.

Halo

The parallelization techniques employed in DarcyTools rely on a Single-Program Multiple-Data (SPMD) approach which first consists in partitioning the grid and then in executing the same piece of code redundantly on each block. This way, computing the interior solution of a given block, works similarly to any computation in a single grid domain. Only the boundary conditions have to differ and additional boundary conditions must be added to reflect the influence of the neighboring blocks flows. This is achieved by adding "halo" cells to the block grids.

Halo cells are additional cells coinciding one by one to interior cells of neighboring blocks. They are used to duplicate the solution periodically provided by neighboring blocks. During their FIF coding, users may always consider that cell values are correct while external face values of halo cells are undefined similarly to external face values of the entire domain.

Duplicating data between block (sub-domains) is achieved with an MPI library as illustrated on Figure H-3.

Halo cells values are strictly equal to neighboring block values. However users should be aware that Tecplot output files contain halo cells which, because of the printing order of superposed cells, may lead to misinterpretation when visualizing blocks.

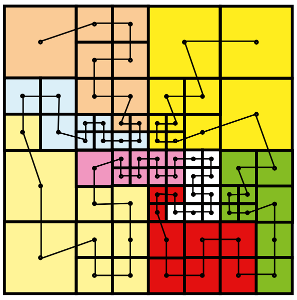

Figure H-1. *Illustration of Paneo-Hilbert space-filling curve partitioning.*

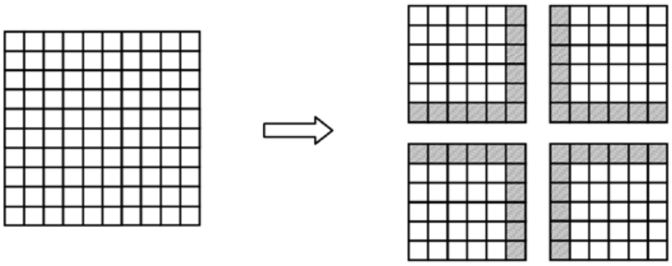

Figure H-2. *Example of domain decomposition with addition of halo cells.*

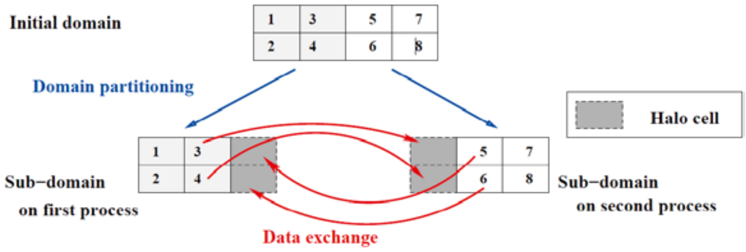

Figure H-3. *Sketch of halo structure and data fluxes between two blocks.*

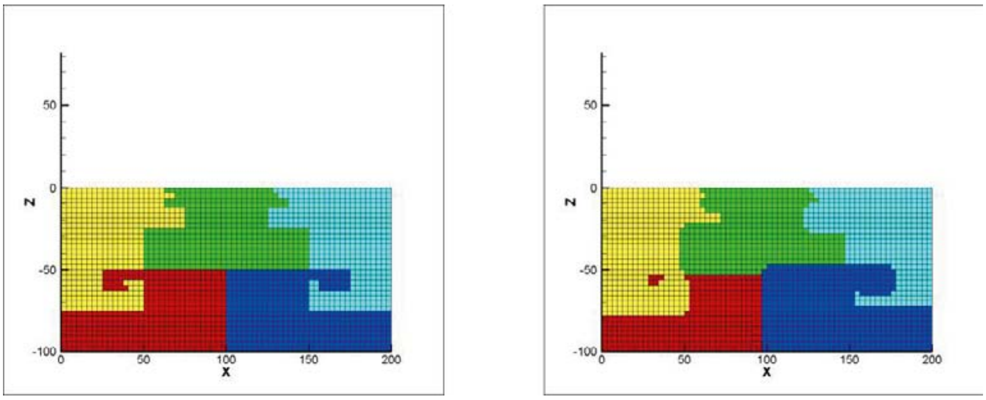

Figure H-4. *Five blocks without (left) and with (right) halo cells.*

H.3 Programming

As mentioned above, the advantage of the Single-Program Multiple-Data (SPMD) strategy is that the same piece of code is executed by each process. The convergence of the entire domain solution is reached by successive updates of halo cells.

For this purpose the process in charge of a given block adds extra Dirichelt boundary conditions to temporarily fix the halo values. Then it computes a new internal solution to fit these halo-values and, in a third step, transmits the newly computed internal cell values to the corresponding halo cells of the neighboring blocks. For a better efficiency these steps (5,6,7-Figure H-5) have been integrated directly into the MIGAL solver and halo-values are updated after each fine grid relaxation of the multi-grid procedure.

At the present stage of the development, this block-Jacobi approach induces a strong penalty in terms of rate of convergence for purely linear cases, and users are invited to increase the solver work per cycle by increasing MIGAL's parameters such as NBRELAX, IPRECO or IGMRES. However, DarcyTools usually involves several non-linear models such as Salinity, Ground Water Table or Tunnel sections, and hundreds of iterations are necessary to ensure convergence. In such cases the Block-Jacobi approach is usually acceptable.

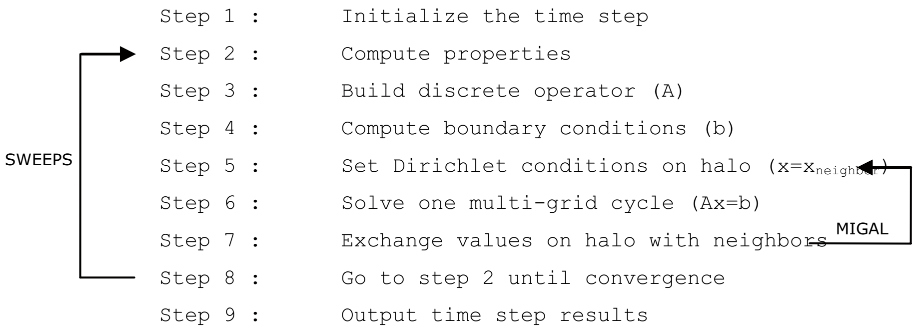

```
Step 1 :      Initialize the time step
Step 2 :      Compute properties
Step 3 :      Build discrete operator (A)
Step 4 :      Compute boundary conditions (b)
Step 5 :      Set Dirichlet conditions on halo (x=x_neighbor)
Step 6 :      Solve one multi-grid cycle (Ax=b)
Step 7 :      Exchange values on halo with neighbors
Step 8 :      Go to step 2 until convergence
Step 9 :      Output time step results
```

Figure H-5. *Time step algorithm for parallel version.*

FIF coding

A drawback of the SPMD strategy is that users must think parallel, keeping in mind that the sole data associated to the block are accessible from user functions. For instance, assuming that cells having the highest altitude in the grid are land or sea cells is not valid any more. The grid of the process is no longer the grid of the entire domain but only the grid of the block. For a successful FIF coding users should keep in mind, at least three important rules:

1- The same user function is executed for every block in parallel. For this reason users should pay attention not to write into the same file and should instead write in several distinct files.

2- Users should keep in mind that locations can be empty for a given block and should adapt their algorithm accordingly. Typically, land or sea locations cannot be simultaneously empty with the sequential version; it is often the case with the parallel version.

3- When computing, for example, a sum of a variable on the entire domain or on a given location, users must remember that their calculation is only local to the block that the process is in charge of. They should also avoid halo cells in their summation since halo-values will already be summed with the internal cells of the neighboring blocks. New facilities (M_BCI module) are provided for reducing local values over blocks.

Beside this, FIF coding can remain unchanged and users are not required to identify halo cells whose values can safely be computed in the same way than interior cell values.

H.4 Concluding remarks

Considering the current direction of computer hardware development, it is believed that parallelization of software is the main way forward to speed up simulations. Version 3.4 is the first parallel version and experiences are so far limited. The chosen SPMD approach does however look promising.